



<http://researchspace.auckland.ac.nz>

ResearchSpace@Auckland

Copyright Statement

The digital copy of this thesis is protected by the Copyright Act 1994 (New Zealand).

This thesis may be consulted by you, provided you comply with the provisions of the Act and the following conditions of use:

- Any use you make of these documents or images must be for research or private study purposes only, and you may not make them available to any other person.
- Authors control the copyright of their thesis. You will recognise the author's right to be identified as the author of this thesis, and due acknowledgement will be made to the author where appropriate.
- You will obtain the author's permission before publishing any material from their thesis.

To request permissions please use the Feedback form on our webpage.

<http://researchspace.auckland.ac.nz/feedback>

General copyright and disclaimer

In addition to the above conditions, authors give their consent for the digital copy of their work to be used subject to the conditions specified on the [Library Thesis Consent Form](#) and [Deposit Licence](#).

Note : Masters Theses

The digital copy of a masters thesis is as submitted for examination and contains no corrections. The print copy, usually available in the University Library, may contain corrections made by hand, which have been requested by the supervisor.

Polarisation Techniques for Surface Plasmon Resonance Sensors

David John Lehar Graham

A thesis submitted in fulfilment
of the requirements for the degree of
Doctor of Philosophy in Physics.

The University of Auckland, 2011.

Abstract

Surface plasmons are electromagnetic waves that propagate along the interface between a metal and a dielectric. Surface plasmons can be excited by attenuated total internal reflection of p-polarised light at a thin metal layer separating a prism from a lower refractive index dielectric. The coupling to the plasmon is very sensitive to the refractive index of the dielectric and this is the basis of surface plasmon resonance (SPR) sensors. SPR sensors, using a metal surface coated with a sensitising layer to which an analyte of interest binds, have found significant applications in biosensing. The amplitude and phase of p-polarised light both change rapidly at the resonance so polarisation techniques can therefore be used to detect very small variations in the refractive index. This thesis presents two SPR instruments using polarisation techniques.

A polarisation imaging SPR instrument is constructed. Linearly polarised light is reflected from an SPR surface, is incident on a polarisation analyser and the transmitted light detected with a camera. The input polarisation that gives minimum transmission through the optical system is measured for each pixel of a 128×48 pixel image. A theoretical analysis of the effect of various experimental conditions on the accuracy of refractive index measurements made with this instrument is presented. Measurements made with salt solutions are presented to demonstrate that refractive index changes can be detected over a 0.01 RIU range near $n = 1.33$. The noise in the refractive index is 2×10^{-6} , similar to that expected from the theoretical analysis. A gold surface patterned with a fluoropolymer is used to demonstrate that spatially varying refractive index changes can be imaged.

A novel technique for differential SPR measurements that detects the difference in refractive index between two areas of a SPR surface was developed. A theoretical analysis of this instrument shows that it should be able to detect changes in the difference of the refractive indices of the two areas. Measurements with salt solutions are presented to demonstrate that this instrument can detect refractive index differences while being insensitive to changes in the refractive index common to both areas of the SPR surface.

Acknowledgements

I would like to thank

My supervisors Lionel Watkins and Rainer Leonhardt.

Steve Warrington and the Mechanical Workshop for the construction of useful equipment.

Contents

1	Introduction	1
1.1	Surface plasmons and sensing	1
1.2	The imaging instrument	2
1.3	The differential instrument	3
1.4	Thesis outline	3
2	Surface plasmon resonance sensors	7
2.1	Surface Plasmons	7
2.2	Surface plasmon resonance	13
2.3	SPR Sensors	14
2.3.1	Measurement techniques	18
2.3.2	Imaging and multi channel SPR instruments	23
3	Imaging theory	27
3.1	Concept	27
3.2	Simulations	30
3.3	Noise	35
3.3.1	The signal to noise ratio	37
3.3.2	SNR for measurements with different ϕ	42
3.4	Effect of changing the gold layer thickness	46
3.5	Wavelength	50

4	Imaging system apparatus	53
4.1	Apparatus Details	54
4.1.1	Light source	54
4.1.2	Modulator	54
4.1.3	Prism and flow cell	57
4.1.4	Analyser	59
4.1.5	Camera	59
4.1.6	Imaging optics	60
4.2	Imaging Measurements	60
4.2.1	Data Acquisition	60
4.2.2	Calibration	62
5	Expected sensor performance	63
5.1	Camera noise and linearity	63
5.2	The SPR surface	68
5.2.1	Polarisation	71
5.3	Expected sensor performance	75
6	Imaging measurements	79
6.1	Refractive index measurements	81
6.1.1	Results for $\phi = 45^\circ$	82
6.1.2	Results for all analyser settings	86
6.2	Patterned Slides	90
6.2.1	Results for patterned sample 1	91
6.3	Discussion and future work	96
7	Differential SPR theory	99
7.1	Concept	99
7.2	Different SPR systems	107
7.3	Differences between the two SPR surfaces	109

7.4	Noise	114
8	Differential SPR apparatus	119
8.1	Apparatus details	120
8.1.1	Light source and polariser	120
8.1.2	Prism and flow cell	120
8.1.3	Angle of incidence control	122
8.1.4	Fresnel Rhomb	122
8.1.5	Analyser and detector	123
8.2	Electronics	123
8.2.1	Photodiode	123
8.2.2	Phase sensitive detector	124
8.2.3	Piezo driver and PI controller	125
8.3	Position sensitive detector	126
9	Differential SPR measurements	129
9.1	Response to small index changes	129
9.2	Sensor response when compensated	131
9.3	Results for a larger refractive index range	137
9.4	Temperature changes	138
9.5	Discussion and future work	141
10	Conclusion	143
A	Scattering matrix method	145
B	Optical properties of materials	151
	References	153

List of Figures

1.1	A polarisation difference image of a patterned gold surface . . .	2
1.2	A measurement made with the differential instrument	4
2.1	System for surface plasmons.	7
2.2	The z component of the electric field for a surface plasmon . .	11
2.3	Electric field for a surface plasmon	11
2.4	The Otto and Kretschmann configurations.	15
2.5	Reflectance vs angle of incidence for a SPR system	15
2.6	Reflectance for different refractive indices	17
2.7	SPR biosensor concept	17
2.8	Reflectance vs wavelength	20
2.9	Phase for different gold thickness	21
2.10	The differential surface plasmon ellipsometer.	22
2.11	Simple SPR imaging configuration.	24
2.12	Self referencing by shifting one resonance	26
3.1	SPR polarisation imaging system concept	28
3.2	Reflectance vs angle of incidence	31
3.3	Phase change on reflection vs angle of incidence	32
3.4	Polarisation ψ_m vs angle of incidence	32
3.5	Polarisation ψ_m vs refractive index	33
3.6	Sensitivity $d\psi_m/dn$ vs refractive index	34

3.7	Transmission vs input polarisation	34
3.8	Maximum transmission $A + B$ vs refractive index change.	36
3.9	Minimum transmission A vs refractive index change.	36
3.10	S/N_{shot} vs θ for varying A	40
3.11	S/N_{sat} vs θ for varying A	40
3.12	Signal noise ratio for the shot noise case	43
3.13	Signal noise ratio for n in the shot noise case	44
3.14	Signal noise ratio for the saturation case	45
3.15	Signal noise ratio for n in the saturation case	45
3.16	Reflectance vs angle of incidence for three gold thickness	47
3.17	Polarisation ψ_m for three gold thickness	47
3.18	Minimum transmission A vs refractive index change	48
3.19	SNR for three gold thicknesses in the shot noise limit	49
3.20	SNR for three gold thicknesses in the camera saturation limit	49
3.21	Reflectance for a non monochromatic light source	51
3.22	Transmission for a non monochromatic light source	51
3.23	Polarisation ψ_m for a non monochromatic light source	52
4.1	The experimental apparatus.	53
4.2	Cross section of the polarisation modulator.	55
4.3	The prism and flow cell.	58
4.4	Intensity vs resistor voltage and the fitted quadratic	62
5.1	Apparatus for measuring the noise and linearity of the camera.	64
5.2	The intensity as measured by the power meter	65
5.3	The intensity as measured by the camera	65
5.4	Intensity measured by the camera vs the power meter	66
5.5	Mean noise in the camera's intensity measurement	66
5.6	Apparatus for characterising the SPR slide	68
5.7	Intensity vs external angle of incidence	69

5.8	The reflectivity for p-polarised light for the SPR slide	69
5.9	Analyser setting for minimum transmission	72
5.10	Sensitivity vs internal angle of incidence	72
5.11	Maximum transmission $A + B$ vs angle of incidence.	74
5.12	Minimum transmission A vs angle of incidence.	74
5.13	SNR in the shot noise limit	76
5.14	SNR in the camera saturation limit	76
6.1	Refractive index of salt (NaCL) solutions vs concentration . .	80
6.2	Refractive index of higher concentration salt solutions	80
6.3	Current measuring resistor voltage for minimum transmission	83
6.4	Polarisation (ψ_m) for a channel from the centre of the image .	83
6.5	An image of the input polarisation for minimum transmission	84
6.6	An image of the difference in the polarisation result	84
6.7	Polarisation for a channel from the centre of the image, 30° . .	87
6.8	Polarisation for a channel from the centre of the image, 20° . .	87
6.9	Sensor response for three settings of the analyser	89
6.10	Intensity for a slide coated with drops of fluoropolymer	92
6.11	Polarisation, ψ_m , image of the partially coated slide	92
6.12	Polarisation, ψ_m , for channels from coated and uncoated areas	95
6.13	Image of the polarisation difference, $\Delta\psi_m$, for two salt solutions	95
6.14	Polarisation difference, $\Delta\psi_m$, image for the second slide	96
7.1	A two prism SPR system.	99
7.2	Reflectance vs angle of incidence for two refractive indices . .	100
7.3	Phase change vs angle of incidence for two refractive indices .	100
7.4	Transmission for the differential SPR instrument	103
7.5	Practical configuration for the differential SPR instrument . .	104
7.6	Transmission vs refractive index difference	104
7.7	Signal vs refractive index difference	106

7.8	Angle, ($\Delta\theta_m$), vs refractive index difference	106
7.9	Signal vs refractive index difference for three SPR systems . .	108
7.10	Angle of incidence difference for three SPR systems	108
7.11	Angle, $\Delta\theta_m$, with non identical SPR surfaces	110
7.12	Angle, $\Delta\theta_m$, with non identical SPR surfaces-compensated . .	110
7.13	Angle, $\Delta\theta_m$ vs the common index	113
7.14	Angle, $\Delta\theta_m$ vs the common index, gold index changed	113
7.15	Transmission vs angle of incidence difference	115
7.16	Signal vs angle of index difference	115
8.1	The apparatus for the differential SPR measurements	119
8.2	The arrangement of the prism and flow cells.	121
8.3	Fresnel rhomb quarter-wave plate.	123
8.4	Photodiode front-end amplifier.	124
8.5	Phase sensitive detector circuit.	124
8.6	Piezo driver and PI controller circuit.	125
8.7	Apparatus used to detect changes in the angle of the mirror. .	127
8.8	Position on the PSD vs angle of the reflected beam	127
9.1	Exchanging water and solution (3) in the flow cells	130
9.2	$\Delta\theta_m$ as the solutions were exchanged, bottom flow cell first . .	132
9.3	$\Delta\theta_m$ as the solutions were exchanged, top flow cell first	132
9.4	Angle $\Delta\theta_m$ for all 16 combinations of the solutions	133
9.5	Angle $\Delta\theta_m$ when both flow cells contain the same solution . .	134
9.6	Angle difference vs refractive index in the bottom flow cell . .	135
9.7	Angle difference vs refractive index difference	135
9.8	Angle $\Delta\theta_m + c$ for high index solutions	137
9.9	The effective single channel configuration	138
9.10	Angle result as the temperature is changed by 4.5°C	139
9.11	Single channel result as the temperature is changed by -4°C .	139

A.1 A thin film system	146
----------------------------------	-----

List of Tables

6.1	The six salt solutions used.	81
6.2	Sensitivity of ψ_m to refractive index changes.	88
6.3	Noise in the polarisation and refractive index.	89
6.4	Sensitivity and noise for the patterned slide.	93
9.1	Solutions used to characterise the differential instrument. . . .	129
9.2	Sensitivity for different solutions in the top flow cell.	136
9.3	The three higher index solutions used.	137
B.1	Optical constants of gold.	151
B.2	Optical constants of chromium.	152

1 Introduction

This thesis presents the design and experimental results for two surface plasmon resonance sensors, using polarisation techniques.

1.1 Surface plasmons and sensing

Surface plasmons are coupled electromagnetic and surface charge waves that propagate along the interface between a conductor and a dielectric. One method of exciting surface plasmons is attenuated total internal reflection in a prism coated with a thin metal film, with a dielectric on the other side of the film [1]. When p-polarised light is incident on the surface, the evanescent wave of the reflected light can couple to a surface plasmon on the metal–dielectric interface, reducing the reflected intensity. The coupling to the plasmon is very sensitive to the refractive index of the dielectric, with a change in the index causing a shift in the angle of incidence at which the resonance occurs. Measuring the reflectivity of the surface to monitor changes in the resonance angle allows small refractive index changes to be detected. The electric field of the plasmon is tightly confined to the interface so only refractive index changes occurring at the surface are detected and this can be useful for monitoring surface chemistry. Sensitivity to a specific analyte can be achieved by coating the metal film with a sensitising layer to which the analyte will bind. When the analyte binds to the surface, the refractive index change at the surface can be detected. This is the basis of surface plasmon resonance (SPR) sensors first demonstrated by Liedberg *et al.*[2].

A number of different techniques for making SPR sensors have been de-

veloped [3]. The main application has been in biosensing, with SPR sensors allowing the detection of molecules in solution and the binding reactions between molecules [4].

1.2 The imaging instrument

Imaging SPR measurements, made with a sensor surface spotted with different sensitising spots, can allow the detection of a large number of different interactions in parallel [5]. The simplest and most commonly used method for SPR imaging is to monitor the change in intensity of p-polarised light reflected from the surface with a camera. This technique has limited accuracy and there has been interest in more accurate SPR imaging systems. For the first part of this thesis, I developed a polarisation imaging SPR instrument. This instrument measures the input linear polarisation that, when reflected from an SPR prism surface, gives the minimum transmission

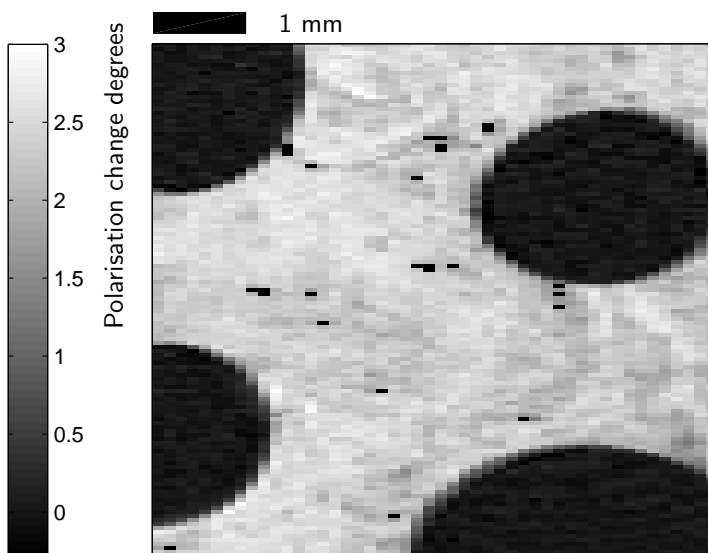


Figure 1.1: Difference in images of a Gold surface patterned with dots of polymer. Made with two salt solutions differing in refractive index by $\Delta n = 0.0006$.

through a polarisation analyser. A CMOS camera with focusing optics is used as the detector, allowing the input polarisation for minimum transmission to be found for each pixel of the polarisation image. Figure 1.1 shows a measurement of a spatially varying refractive index change made with this instrument. The gold surface used is partially coated with a polymer. When salt solutions with different refractive indices are flowed over the surface, the measured polarisation for the uncoated areas changes. The refractive index, and thus the polarisation, of the coated areas remains constant.

1.3 The differential instrument

For SPR sensors, a major limitation on the accuracy of the measurement is drifts due to changes in the bulk refractive index or temperature. Imaging instruments can be used to compare a sensitised area to an un-sensitised reference area. It is also possible to use simpler instruments that measure a sample and a reference channel [6, 7]. The second part of this thesis presents a novel differential SPR instrument that measures the refractive index difference between two areas of a surface. This instrument detects the difference in the angle of incidence at which the surface plasmon resonance occurs for the two areas. Figure 1.2 shows how the sensor responds to different salt solutions in two flow cells covering the two areas measured. Differences in the refractive index are detected while changes in the refractive index common to both areas are not.

1.4 Thesis outline

Chapter 2 gives a description of SPR sensors. The properties of surface plasmons on a metal–dielectric interface are derived from Maxwell’s equations. The concept and applications of SPR to sensing are described. The different techniques used to make SPR measurements are explained, with examples from the literature.

The concept of the polarisation imaging SPR instrument is described in chapter 3. The relationship between the measured input polarisation for minimum transmission, ψ_m , and the reflection coefficients of the SPR surface

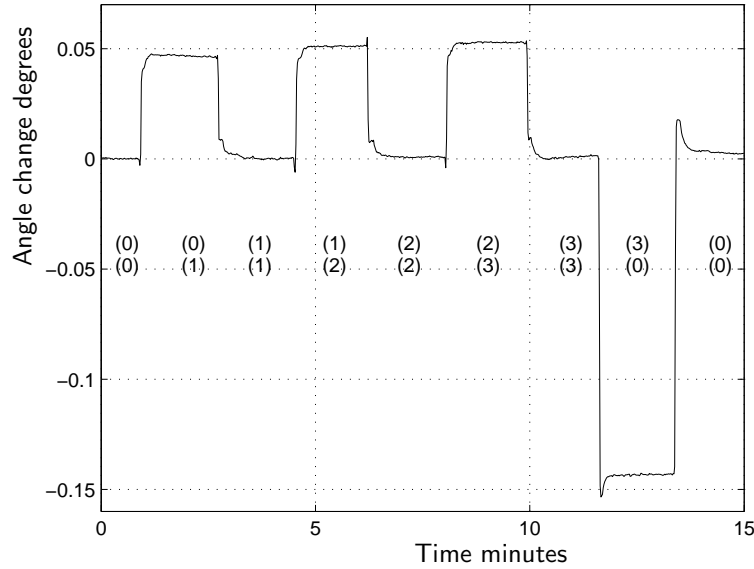


Figure 1.2: The response of the differential instrument to different combinations of salt solutions, numbered (0) to (3), in the $\begin{smallmatrix} \text{(top)} \\ \text{(bottom)} \end{smallmatrix}$ flow cells. When both flow cells contain the same solution the sensor output does not change, but when the solutions are different the output changes in proportion to the difference.

is derived. Using the scattering matrix method of thin film modelling, the reflection coefficients are calculated and the dependence of ψ_m on the refractive index found. A theoretical analysis of the signal to noise ratio is used to determine the effect of different experimental conditions on the accuracy with which the refractive index can be measured.

The experimental apparatus used for the polarisation imaging SPR instrument is described in chapter 4. The procedure for calculating the polarisation image and calibrating the instrument is explained.

In chapter 5, measurements of the performance of the camera and the properties of the SPR surfaces used are presented. Based on these measurements, and the theoretical signal to noise ratio analysis from chapter 3, the expected performance of the imaging system is estimated.

Polarisation imaging SPR measurements made with my instrument are presented in chapter 6. Measurements made with salt solutions with different

refractive indices are used to determine the sensitivity and linearity of the instrument. Measurements of an SPR surface patterned with a polymer layer are used to demonstrate the instrument's ability to detect spatially varying refractive index changes.

The concept of the differential SPR instrument is introduced in chapter 7. Theoretical modelling of the performance of the instrument is presented. A modification to the initial concept to allow two SPR surfaces with different properties to be used is investigated.

The experimental implementation of the differential SPR instrument is described in chapter 8.

Measurements made with the differential SPR instrument are presented in chapter 9. Salt solutions of known index are used to investigate the ability of the instrument to measure refractive index differences.

Chapter 10 summarises the work done for this thesis.

2 Surface plasmon resonance sensors

This chapter introduces surface plasmon resonance sensors. The properties of surface plasmons are derived from Maxwell's equations. The coupling of light to a surface plasmon by attenuated total internal reflection in a prism is described. The concept and applications of surface plasmon resonance sensors based on this effect is summarised. Examples of the different measurement techniques used for surface plasmon resonance sensors are described.

2.1 Surface Plasmons

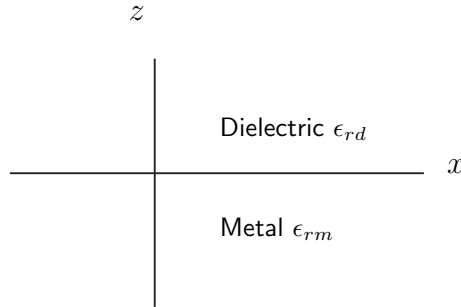


Figure 2.1: System for surface plasmons.

Surface plasmon polaritons¹ are coupled electromagnetic and surface charge waves that propagate along the interface between a conductor and a dielectric. Consider an interface with a metal relative permittivity ϵ_{rm} occupying

¹Referred to as surface plasmons throughout this thesis.

$z < 0$ and a dielectric ϵ_{rd} , with both media non magnetic $\mu_m = \mu_d = \mu_0$, as shown in figure 2.1. Maxwell's equations in the media are [8]

$$\nabla \cdot E = 0, \quad (2.1)$$

$$\nabla \times E = -\frac{\partial B}{\partial t}, \quad (2.2)$$

$$\nabla \cdot B = 0, \quad (2.3)$$

$$\nabla \times B = \mu_0 \epsilon_0 \epsilon_{rj} \frac{\partial E}{\partial t}, \quad (2.4)$$

where j is m , metal or d , dielectric.

To find the properties of the surface plasmon we look for a solution to Maxwell's equations in the form of a wave propagating along the interface in the positive x direction. It can be shown that solutions to Maxwell's equations for this system in the form of a wave propagating in the x direction are either transverse electric (TE, electric field in the $\pm y$ direction, s-polarised), or transverse magnetic (TM, magnetic field in the $\pm y$ direction, p-polarised) [9]. For the wave to be guided it must be evanescent in both materials. So the fields will decay exponentially away from the interface with decay constants α_m and α_d in the metal and dielectric. Only TM guided surface modes exist for this system [9] so the x and z components of the magnetic field and the y component of the electric field are zero. So the fields for a plasmon propagating in the positive x direction have the form [10]²

$$E_j = (E_{jx}, E_{jy}, E_{jz}) = (E_{0jx}, 0, E_{0jz}) \exp(-\alpha_j |z| + i(\beta x - \omega t)), \quad (2.5)$$

$$B_j = (B_{jx}, B_{jy}, B_{jz}) = (0, B_{0jy}, 0) \exp(-\alpha_j |z| + i(\beta x - \omega t)), \quad (2.6)$$

where j is m , metal or d , dielectric, ω angular frequency, t time, and β the propagation constant.

We can find α_j and β by substituting the equations for the fields into Maxwell's equations. Substituting the fields into equation 2.1 gives

$$\frac{\partial}{\partial x} E_{jx} + \frac{\partial}{\partial y} E_{jy} + \frac{\partial}{\partial z} E_{jz} = 0, \quad (2.7)$$

²My derivation follows reference [10], but uses SI units and B rather than Gaussian units and H .

$$i\beta E_{0jx} \exp(-\alpha_j|z| + i(\beta x - \omega t)) \mp_j \alpha_j E_{0jz} \exp(-\alpha_j|z| + i(\beta x - \omega t)) = 0, \quad (2.8)$$

where $\pm_j = +$ in the dielectric ($j = d$) and $-$ in the metal ($j = m$) (also $\mp_j = -\pm_j$). This can then be simplified to

$$i\beta E_{0jx} \mp_j \alpha_j E_{0jz} = 0. \quad (2.9)$$

While similarly substituting the fields into equation 2.2 and simplifying gives

$$\mp_j \alpha_j E_{0jx} - i\beta E_{0jz} = i\omega B_{0jy}. \quad (2.10)$$

As the magnetic field is independent of y and has no x or z component, $\nabla \cdot B = 0$, we get no additional condition from equation 2.3.

Substituting the fields into equation 2.4 and simplifying as above gives

$$\pm_j \hat{x} \alpha_j B_{0jy} + \hat{z} i \beta_j B_{0jy} = -i\omega \mu_0 \epsilon_0 \epsilon_{rj} (\hat{x} E_{0jx} + \hat{z} E_{0jz}), \quad (2.11)$$

where \hat{x} and \hat{z} are the x and z unit vectors. Separating the equation into its x and z components gives us two equations

$$\hat{x} \longrightarrow \pm_j \alpha_j B_{0jy} = -i\omega \mu_0 \epsilon_0 \epsilon_{rj} E_{0jx}, \quad (2.12)$$

$$\hat{z} \longrightarrow i \beta_j B_{0jy} = -i\omega \mu_0 \epsilon_0 \epsilon_{rj} E_{0jz}. \quad (2.13)$$

Equations 2.9, 2.10 and 2.13 can be solved for α_j . Start with equation 2.9 and substitute in E_{0jx} from equation 2.10 to get

$$\frac{i\beta}{\mp_j \alpha_j} (i\omega B_{0jy} + i\beta E_{0jz}) \mp_j \alpha_j E_{0jz} = 0, \quad (2.14)$$

$$\alpha_j^2 E_{0jz} = \beta (\omega B_{0jy} + \beta E_{0jz}). \quad (2.15)$$

Then using B_{0jy} from equation 2.13

$$\alpha_j^2 E_{0jz} = \beta \left(\frac{-\omega}{\beta} (\omega \mu_0 \epsilon_0 \epsilon_{rj} E_{0jz}) + \beta E_{0jz} \right), \quad (2.16)$$

$$\alpha_j^2 E_{0jz} = -\omega^2 \mu_0 \epsilon_0 \epsilon_{rj} E_{0jz} + \beta^2 E_{0jz}, \quad (2.17)$$

$$\alpha_j = \sqrt{\beta^2 - \mu_0 \epsilon_0 \epsilon_{rj} \omega^2}. \quad (2.18)$$

The components of fields parallel to the interface must match giving the conditions $E_{0dx} = E_{0mx}$ and $B_{0dy} = B_{0my}$. Starting then with the condition

$$B_{0dy} = B_{0my}, \quad (2.19)$$

and using equation 2.12 gives

$$\frac{-i\omega\mu_0\epsilon_0\epsilon_{rd}}{\alpha_d E_{0dx}} = \frac{i\omega\mu_0\epsilon_0\epsilon_{rm}}{\alpha_m E_{0mx}}. \quad (2.20)$$

Then using $E_{0dx} = E_{0mx}$ and cancelling we can find

$$\frac{\epsilon_{rd}}{\alpha_d} + \frac{\epsilon_{rm}}{\alpha_m} = 0, \quad (2.21)$$

the surface plasmon condition [10].

The propagation constant can be found from the surface plasmon condition by substituting in α_j from equation 2.18

$$\frac{\epsilon_{rd}}{\sqrt{\beta^2 - \mu_0\epsilon_0\epsilon_{rd}\omega^2}} + \frac{\epsilon_{rm}}{\sqrt{\beta^2 - \mu_0\epsilon_0\epsilon_{rm}\omega^2}} = 0, \quad (2.22)$$

$$\epsilon_{rd}^2(\beta^2 - \mu_0\epsilon_0\epsilon_{rm}\omega^2) = -\epsilon_{rm}^2(\beta^2 - \mu_0\epsilon_0\epsilon_{rd}\omega^2), \quad (2.23)$$

$$\beta^2(\epsilon_{rd}^2 + \epsilon_{rm}^2) = \mu_0\epsilon_0\epsilon_{rd}\epsilon_{rm}\omega^2(\epsilon_{rd} + \epsilon_{rm}). \quad (2.24)$$

Using $c = 1/\sqrt{\mu_0\epsilon_0}$ the propagation constant is then

$$\beta = \frac{\omega}{c} \sqrt{\frac{\epsilon_d\epsilon_m}{\epsilon_d + \epsilon_m}} = \frac{2\pi}{\lambda} \sqrt{\frac{n_d^2 N_m^2}{n_d^2 + N_m^2}}, \quad (2.25)$$

where λ is the vacuum wavelength for light with angular frequency ω and n_d and $N_m = n_m + ik_m$ are the refractive indices of the dielectric and metal.

The parameters E_{0jz} and E_{0jx} are related by equation 2.9

$$E_{0jx} = \frac{\pm_j \alpha_j E_{0jz}}{i\beta}, \quad (2.26)$$

and $E_{0mx} = E_{0dx}$.

Figures 2.2 and 2.3 show the electric field for a surface plasmon on a

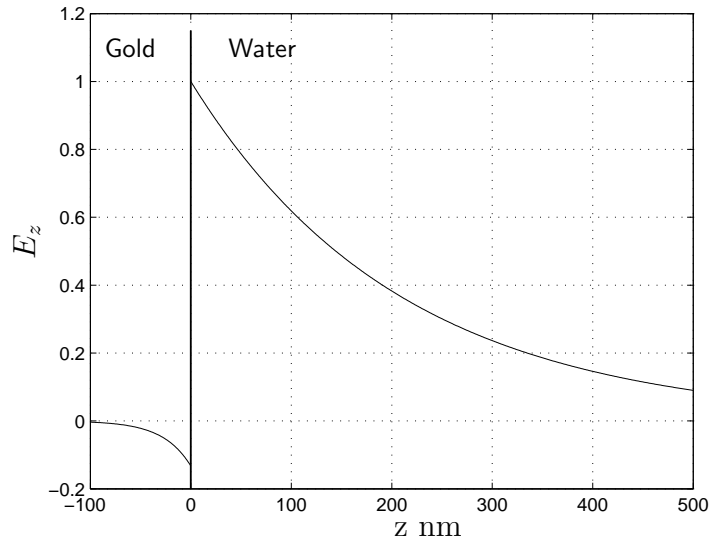


Figure 2.2: The component of the electric field perpendicular to the interface (E_z) for a surface plasmon on a gold water interface at $\lambda = 680$ nm. The field is normalised such that $E_{0dz} = 1$ and is shown at $t = 0$, $x = 0$.

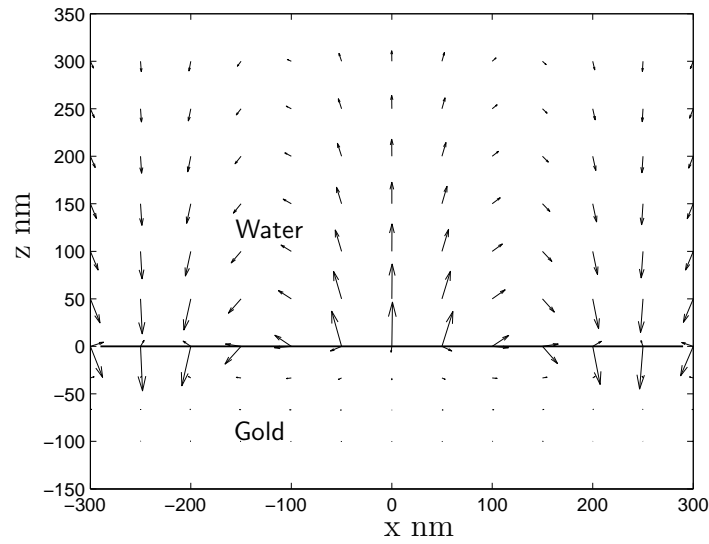


Figure 2.3: Electric field for a surface plasmon on a gold water interface at $\lambda = 680$ nm and $t=0$.

gold water interface with $\lambda = 680$ nm. Here and throughout this thesis, λ is the vacuum wavelength for light with angular frequency ω . Note that the plasmon is tightly confined to the interface with most of the field in the dielectric. The plasmon decays rapidly due to the loss in the metal with the propagation length ($1/e$ amplitude) being $11 \mu\text{m}$ for a gold water interface with $\lambda = 680$ nm.

The surface charge (σ) wave component of the plasmon can be found from the discontinuity of E_z

$$\sigma = \epsilon_0(E_{dz}(z=0) - E_{mz}(z=0)), \quad (2.27)$$

$$\sigma = \epsilon_0(E_{0dz} - E_{0mz}) \exp i(\beta x - \omega t). \quad (2.28)$$

So there is a surface charge wave with the same propagation constant and frequency as the electromagnetic wave, as expected.

For light to couple to the surface plasmon, the component of the wave vector $k = 2\pi n/\lambda$ of the incident light parallel to the surface must be equal to the real part of the propagation constant. This is the phase matching condition $k_x = \Re(\beta)$ [10], where $\Re(x)$ is the real part of x . If the real part of β is greater than k for light in the dielectric, light will not couple to the plasmon for any angle of incidence. This condition $k < \Re(\beta)$ is equivalent to the condition that the wavelength of the light in the dielectric is longer than the wavelength of the plasmon ($\lambda_p = 2\pi/\Re(\beta)$). The result is a non-radiative surface plasmon mode that does not couple directly to light. This occurs for some metals including gold, silver and aluminium in the visible and near infra-red frequency ranges. If the field of the plasmon coupled directly to light, the field in the dielectric would not be evanescent and the mode would not be guided.

While surface plasmons do not directly couple to light on a flat interface, they can be coupled to light by surface features and roughness [9]. Diffraction gratings can be used to couple surface plasmons where, for a particular angle of incidence, a diffracted order will couple to a plasmon and be absorbed [11]. Surface plasmons were first observed by Wood [12] as anomalous absorption in a diffraction grating.

The tight confinement of the plasmon to the surface has led to their investigation for sub-wavelength optics and wave-guides [13]. The unexpectedly

high transmission of thin metal films with arrays of sub-wavelength holes is attributed to surface plasmons [14].

In a thin metal film embedded in a dielectric, a plasmon on one side of the film will couple to a plasmon on the other side. This can form symmetric and anti-symmetric modes where the fields of the two plasmons add and subtract in the metal respectively. The anti-symmetric mode, the long range surface plasmon, is of interest for wave guides as the reduction in the field in the metal reduces the loss and increases the distance the plasmon will propagate [15]. The coupling across a metal film has also been used to enhance the transmission of light through a LED electrode [16].

2.2 Surface plasmon resonance

A surface plasmon can couple to the evanescent wave of p-polarised light that experiences attenuated total internal reflection in a prism. This can occur in the Otto [17] or Kretschmann [1] configurations as shown in figure 2.4. In the Otto configuration the dielectric is a thin layer between a metal surface and the prism. In the Kretschmann configuration a prism with a thin (~ 50 nm) metal layer on it is used. The evanescent wave penetrates into the metal and excites a plasmon on the opposite interface. The condition for the coupling is that the wave vector of the evanescent wave must equal the real part of the propagation constant of the surface plasmon, the same phase matching condition as above, and this can be achieved by adjusting the angle of incidence θ , [18]

$$k_x = \Re(\beta), \quad (2.29)$$

$$\frac{2\pi}{\lambda} n_p \sin \theta \approx \frac{2\pi}{\lambda} \Re \left(\sqrt{\frac{n_d^2 N_m^2}{n_d^2 + N_m^2}} \right), \quad (2.30)$$

where the refractive index of the prism n_p must be greater than that for the dielectric ($n_p > n_d$). There is no coupling of s-polarised light to the plasmon as this light is transverse electric (TE) while the plasmon is transverse magnetic (TM). This condition is approximate as the presence of the prism within the evanescent field of the plasmon will alter the propagation constant of the plasmon (β). Surface plasmons excited in this condition lose

energy to the coupling to light in the prism (leakage radiation) as well as absorption in the metal [9]. Destructive interference between the reflected light and the leakage radiation reduces the intensity of the reflected beam. For an optimum metal thickness and angle of incidence, where the loss due to leakage is equal to the loss due to absorption in the metal, the reflected intensity will be zero [9]. The Kretschmann configuration is usually used for sensing applications as the plasmon is excited on the external surface of the metal film and the dielectric is easily accessible. All the work for this thesis used prism coupling in the Kretschmann configuration.

Figure 2.5 shows the effect of the surface plasmon resonance for a typical Kretschmann configuration. Note that there is a steep dip in the reflectivity for p-polarised light (R_p) at the resonance with no corresponding change in R_s as the s-polarised light is not coupled to the plasmon. The kink at about 62° corresponds to the critical angle for total internal reflection if the metal film was not present. The data for this figure and other simulations shown are calculated from the Fresnel equations using the scattering matrix method [19] as described in appendix A.

The coupling to the plasmon depends on the refractive index of the metal layer and dielectric (see equation 2.30) as well as the thickness of the metal film. Measurements of the surface plasmon resonance can thus be used to characterise the thickness and optical properties of thin films [20, 21]. The intense electric field of the plasmon can be used to investigate non-linear optical effects such as second [22] and third [23] harmonic generation.

2.3 SPR Sensors

The propagation constant of the surface plasmon depends on the refractive index of the dielectric so if the index changes, the angle of incidence at which the resonance occurs changes (see equation 2.30). Figure 2.6 shows how the resonance angle shifts as the index changes for a typical sensor configuration. The change in index may be detected from the change in the position of the resonance minimum. As shown in the figure, the refractive index change may also be detected from the change in the reflected intensity for a constant angle of incidence. The phase of the p-polarised light also changes at the resonance

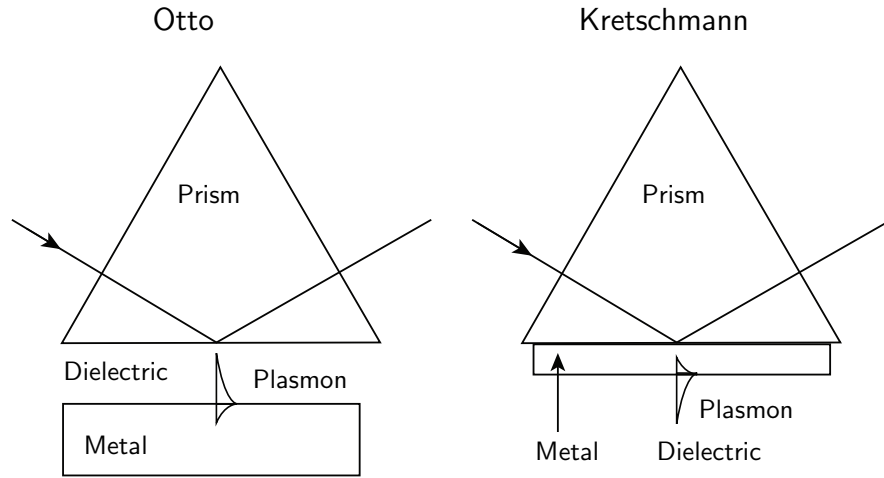


Figure 2.4: The Otto and Kretschmann configurations.

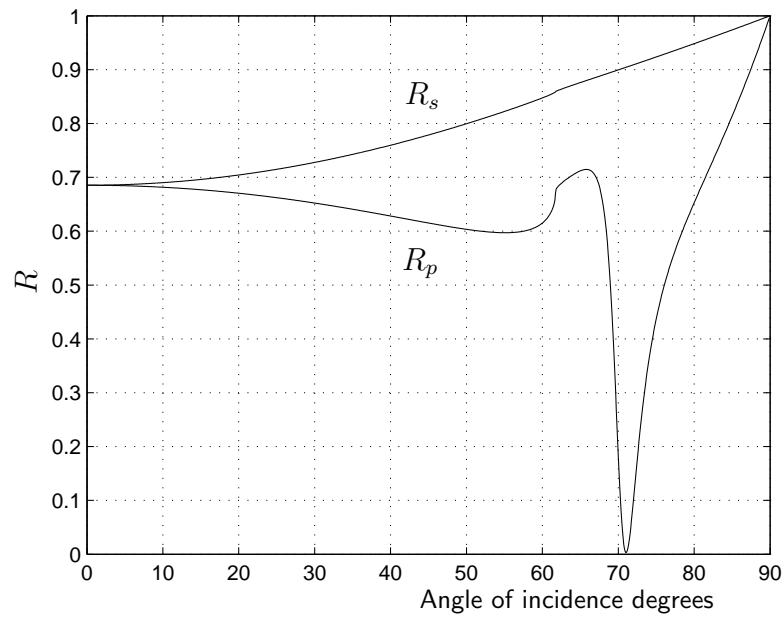


Figure 2.5: Reflectance for p-polarised (R_p) and s-polarised (R_s) light vs angle of incidence for a Kretschmann configuration SPR system. Glass prism $n = 1.51$ and a 48 nm gold film separated by 3 nm chromium, dielectric water $n = 1.33$. This system is similar to that used for my experimental work.

so phase and polarisation techniques may be used as will be described later in this chapter. As the electric field of the plasmon only extends a short distance into the dielectric (see figures 2.2 and 2.3) only changes at the metal surface affect the resonance. If the metal film is coated in a sensitising layer that some analyte of interest will bind to and then a solution containing that analyte is flowed over it, binding of the target analyte to the surface will change the refractive index near the surface and thus change the resonance angle. This is the principle of surface plasmon resonance sensors as shown in figure 2.7.

A variety of SPR sensors have been developed. The main application has been in biosensing, with SPR allowing the detection of molecules and the binding reactions between them [4]. Antibodies, proteins produced by immune systems that bind to a specific antigen, are commonly used as the basis of sensitising layers. As well as simply detecting the presence of an analyte in a solution, the rate at which the binding occurs provides information about the reactions between molecules. More complex measurements can also be made, for example to determine the relative binding of the analyte to two antibodies, one on the SPR surface and the other in a solution. Commercial instruments for SPR sensing have become available [24] in particular those produced by Biocore³. The reviews by Homola [3, 25] and Abdulhalim *et al.* [26] give overviews of the principle and use of SPR sensors. The second two reviews [25, 26] give references to large numbers (~ 100) of applications of SPR sensors mostly using commercial instruments, in particular Biocore. The following papers give examples of the range of applications of SPR sensors for detecting: bacteria [27] [28], DNA [29], viruses [30], arsenic [31], pesticides [32], explosives [33]. For the purposes of this thesis it is sufficient to know that the detection of small refractive index changes occurring at a surface has many useful applications.

SPR sensors usually use gold as the metal film. Gold gives a suitable resonance for red and near infra-red light and has good chemical properties. Silver as used in the first SPR sensors [2] gives a narrower resonance than gold, particularly for red light, but its lower chemical resistance, in particular the formation of a sulphide layer due to SO_2 in air, makes it less suitable in practice. The possibility of using a silver film with a protective layer of gold

³Biocore Systems www.biocore.com

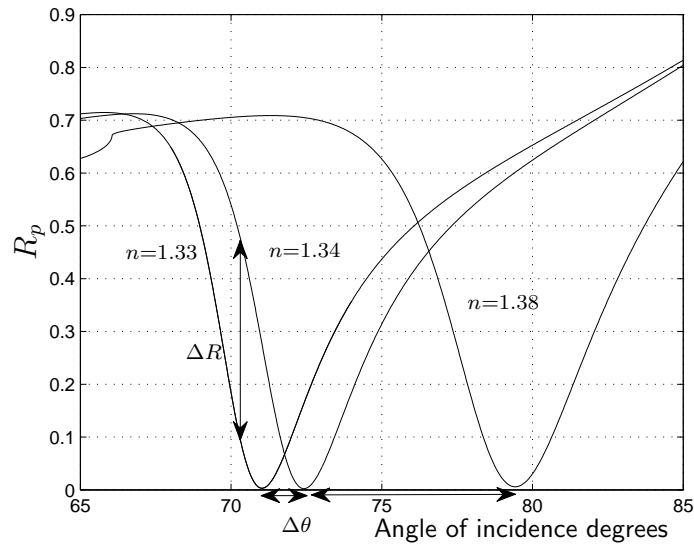


Figure 2.6: Reflectance for p-polarised light (R_p) for different dielectric refractive index values vs angle of incidence. Sample glass $n=1.51$ with 3 nm chromium and 48 nm gold, $\lambda = 680$ nm.

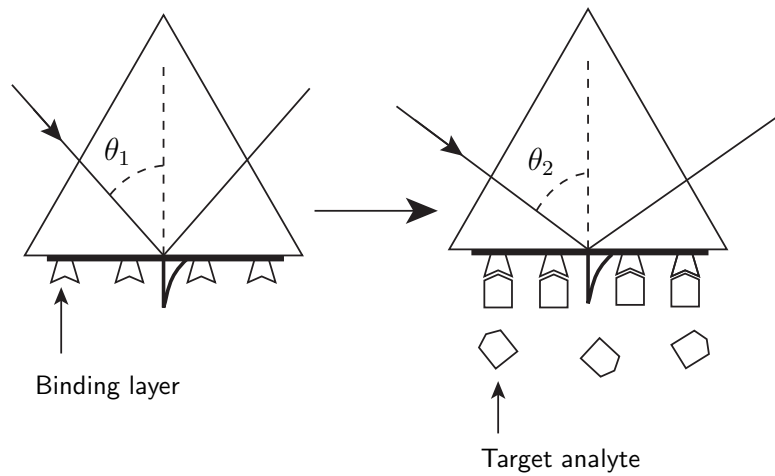


Figure 2.7: SPR biosensor concept. The binding of the target analyte to the sensitising layer changes the angle of incidence at which the coupling to the plasmon occurs from θ_1 to θ_2 .

for a SPR sensor has been investigated [34].

2.3.1 Measurement techniques

This section describes the different SPR measurement techniques that have been developed.

Intensity measurement

SPR sensors were first demonstrated by Liedberg *et al.* [2]. Their experiments used a quartz prism coated with silver films with sensitising layers. A beam of p-polarised light from a helium-neon laser was reflected from the sample at an angle of incidence slightly less than that for the reflectivity minimum where the reflectivity is changing rapidly and linearly with angle as shown in figure 2.6. The reflected intensity was monitored with a photodiode. Shifts in the resonance angle were detected from the change in the reflected intensity. Detection of a halothane gas was demonstrated using a thin film of silicone oil as the sensitising layer. They also demonstrated the use of the SPR sensor for biosensing using their apparatus to detect the binding of an antibody to an antigen [35].

The intensity measurement technique described above is simple but the difficulties in accurately measuring the reflectivity can limit the accuracy. To achieve an accuracy of 10^{-6} RIU (refractive index units)⁴ requires that the reflected intensity be measured with an accuracy of the order of 10^{-4} [3].

Angle measurement

As shown in figure 2.6, the obvious effect of a refractive index change is to shift the angle of incidence at which the surface plasmon resonance occurs. It is possible to scan the angle of incidence while recording the intensity and then calculate the angle for minimum intensity. Angle measurement can give SPR measurements with good linearity over a much larger refractive index range than intensity measurement (see figure 2.6). The imaging system of

⁴While refractive index is a dimensionless number, in the SPR literature it is usually given units of RIU.

VanWiggeren *et al.* [18] that will be described in the section on imaging instruments is a good example of this technique.

A simpler alternative to scanning the angle of incidence is to reflect a diverging beam from the sample and then detect it with a 1D photodiode array or CCD [36, 37]. As each pixel will receive light reflected at a different angle of incidence, this gives the same result without needing a scanning system. This configuration is used in the most common commercial SPR systems (Biocore and others) with accuracies of 10^{-6} RIU being typical. It has been shown that for realistic input power levels and detectors, the shot noise limit of the accuracy can be as low as 10^{-9} RIU [37]. An illustration of the advantage of this technique is a commercial system: the Spreeta2000 which has a LED and diode array built into a plastic prism and gives high accuracy SPR measurements [38] in a 3 cm package.

A SPR instrument where a piezo actuator is used to rapidly modulate the angle of incidence and the resulting differential signal detected has been demonstrated [39].

Wavelength measurement

The propagation constant depends on the dielectric constant of the metal as well as the dielectric (see equation 2.25). Gold is highly dispersive and so a small change in the wavelength changes the angle at which the resonance occurs significantly. As a result, a plot of reflectance vs wavelength for a given angle of incidence shows a similar minimum at resonance to a plot of reflectance vs angle of incidence for a given wavelength. This is shown in figure 2.8. SPR measurements can thus be made by illuminating the sample with a broadband light source, detecting the reflected light with a spectrometer and finding the wavelength for minimum reflectance [40]. A high accuracy wavelength scanned SPR sensor has been demonstrated by Caruso *et al.* [41] using an acousto-optic tunable filter to control the wavelength of light incident on the sample.

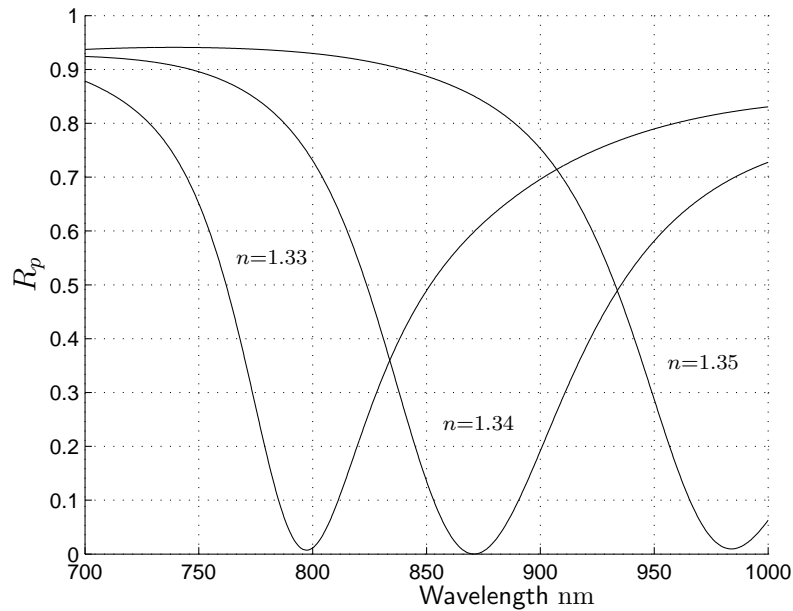


Figure 2.8: Reflectance vs wavelength for 45 nm gold on glass $n = 1.51$. Results for three different dielectrics $n = 1.33, 1.34$ and 1.35 are shown. The angle of incidence is 69° .

Phase techniques

At the surface plasmon resonance, the phase of the reflection coefficient for p-polarised light ($\arg r_p$) as well as its magnitude changes and interferometric SPR instruments that measure the phase have been demonstrated [42]. Typically the phase difference between the p and s polarised light is measured allowing a common path configuration. The shape of the phase change depends sensitively on the thickness of the film. Figure 2.9 shows the phase near the resonance for SPR systems with different thicknesses of gold. If the thickness of the metal is chosen appropriately the phase can change very rapidly as a function of angle of incidence or refractive index and this has been used for high accuracy SPR measurements [43]. However a steep phase change corresponds to a low reflected intensity so there may be no advantage to a steeper phase change if the measurement is limited by the shot noise [44]. Also if a very steep phase change is used, the measurement is limited to a very small refractive index range. Related to the phase is the Goos-Hänchen

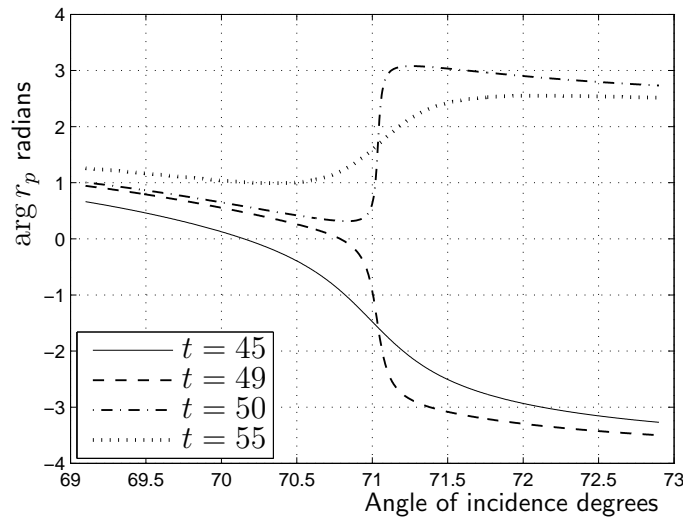


Figure 2.9: Phase for different gold thickness $t = 42, 49, 50$ and 55 nanometres. BK7 glass prism $n=1.51$, dielectric $n = 1.33$, 3 nm chromium layer and $\lambda = 680$ nm.

shift, the lateral displacement of a totally internally reflected beam, and an SPR instrument that measures this has been demonstrated [45].

Polarisation techniques

Both the amplitude and phase of the p-polarised light change rapidly at the resonance. So the polarisation of a non pure s or p polarisation state reflected from a SPR surface will change as the refractive index changes. Polarisation measurement techniques such as ellipsometry [19] can thus be used for SPR measurements [6, 46, 47].

Polarisation control can be used with intensity, angle or wavelength techniques to control the contrast or change the intensity minimum at the resonance to a maximum [48, 49].

The differential surface plasmon ellipsometer is a high accuracy SPR instrument demonstrated by Hooper *et al.* [50]. This system is shown in figure 2.10. In this instrument, linearly polarised light is incident on a metal coated surface in the Kretschmann configuration and the azimuth of the po-

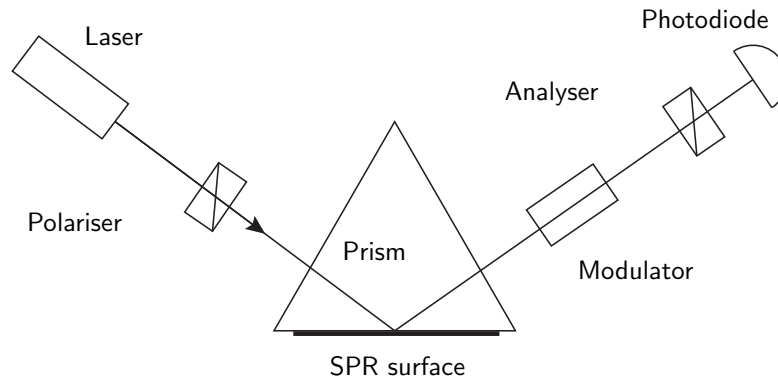


Figure 2.10: The differential surface plasmon ellipsometer.

larisation ellipse of the reflected light is measured. At the surface plasmon resonance with an appropriate input polarisation, the azimuth of the ellipse, which corresponds to the setting of a polariser's transmission axis that would give maximum intensity, is very sensitive to the refractive index. To measure the azimuth with high accuracy the azimuth of the light reflected off the sample is modulated sinusoidally by a Faraday rotator. If the light is then incident on a polariser and a photodetector, the AC component of the photocurrent at the modulation frequency is proportional to the differential of the intensity as a function of the azimuthal angle. This differential signal can be detected with high accuracy by a phase sensitive detector and changes in the azimuth can be detected by directly monitoring the detector output. Better accuracy and insensitivity to fluctuations in the laser intensity can be achieved by using the phase sensitive detector's output as a feedback signal to apply an offset to the modulator that makes the differential signal zero. The value of the offset is then measured. High accuracy refractive index measurements have been demonstrated with this instrument with sensitivities (2 standard deviation) of 2×10^{-7} RIU for a silver coated prism with gas samples [50] and better than 5×10^{-7} for gold surfaces for aqueous samples [51].

Wave guide and fibre optic sensors

Most SPR sensors use the Kretschmann configuration as above but other systems where there is an evanescent wave from total internal reflection can be used. Very compact SPR sensors can be constructed using optical fibres [52, 53]. Integrated optic waveguides can also be used for compact sensors [54]. A waveguide with a palladium film [55] has been used as a hydrogen sensor and since absorption of hydrogen by the palladium changes its refractive index, no sensitising layer is needed.

Diffraction grating sensors

Surface plasmons can also be excited by a diffracted mode of light reflected from a diffraction grating [11]. SPR sensors that measure the angle [56] or wavelength [57] at which the diffracted light couples to a plasmon have been demonstrated. Diffraction grating sensors have the advantage for practical applications that a replaceable sensor surface can be used without requiring it to be index matched to a prism.

2.3.2 Imaging and multi channel SPR instruments

Imaging or multi-channel SPR measurements can also be made [5], combined with a sensor surface spotted with different sensitising spots this can allow the detection of a large number ($100 \sim 1000s$) of different interactions in parallel [58, 59, 29]. This also allows the use of reference areas that are not sensitised to allow for correction of drifts due to changes in the bulk refractive index or temperature. The simplest and most commonly used method for making SPR imaging measurements is to reflect a beam of p-polarised light from the sample and monitor changes in its intensity with a camera as shown in figure 2.11. Resolutions of $\sim 10^{-5}$ RIU [60] are typically achieved with this technique, making it significantly less sensitive than single channel angle or wavelength scanned systems.

There is thus interest in developing more accurate imaging SPR systems. An imaging SPR system using polarisation control to increase the contrast and pairs of multilayer sensing spots has demonstrated a resolution

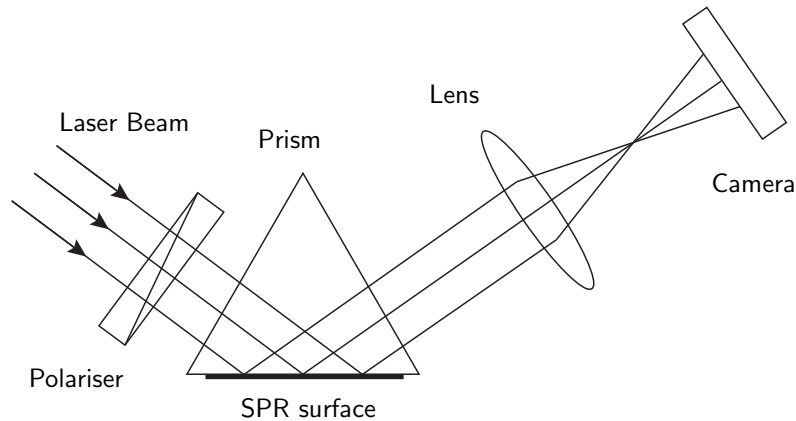


Figure 2.11: Simple SPR imaging configuration.

of 2×10^{-6} RIU for 64 independent channels [61, 62]. Imaging interferometers have been used to detect the phase change for the p-polarised light at the resonance [63, 64]. Angle scanned SPR imaging systems can give high accuracy measurements over a large refractive index range. The Ibis is a commercial SPR imaging instrument using a mechanical angle scanning mirror [65]. VanWiggeren *et al.* [18] demonstrated an instrument using an acousto-optic deflector to modulate the angle of incidence and a high speed camera as the detector. This instrument achieved a resolution of 2.6×10^{-8} RIU for 110 channels with a 1 second measurement time and 0.06 RIU range, the best performance of any SPR imaging instrument demonstrated. A multi channel instrument based on an array of diffraction gratings has also been demonstrated [56].

Recently a SPR biosensing measurement made with an imaging version of the differential surface plasmon ellipsometer described in section 2.3.1. has been presented [66]. This sensor uses a custom fabricated CMOS chip with a 64×64 pixel photodiode array and 64 phase sensitive detectors which can read any row of the pixel array. A measurement equivalent to the single channel instruments described can be made for a row of pixels using the phase sensitive detectors. The sensor can then be electronically scanned by selecting different rows to build up a 64×64 pixel image. The range and noise performance of this sensor are not specified.

If a 1D array of sensing spots is adequate, a variant of the angle measure-

ment technique using a non collimated beam and a 1D CCD array described in section 2.3.1 can be used [67]. Light from each sensing spot is imaged onto a line of pixels on a 2D CCD. A similar system has been demonstrated using a position dependent band pass filter where the observed wavelength rather than the angle of incidence varies along each line of pixels [68].

Self referenced Instruments

Simpler systems with only 2 channels have been developed. These may be useful to measure a single binding reaction with a reference to correct for bulk index or temperature changes. The obvious way of doing this is to use one of the single channel techniques described above using two beams and two detectors [6, 69, 70].

A two channel measurement can also be made with a single detector by shifting the resonance of one channel so that the two resonances can be distinguished. One way of doing this, as shown in figure 2.12, is to coat part of the sensor surface with a thin, high refractive index layer [7]. This will shift the angle or wavelength at which the resonance occurs for that area or channel. So an angle or wavelength scan will show two intensity minima. As long as the high index layer is much thinner than the penetration depth of the surface plasmon, the resonance will still change in response to refractive index changes. Refractive index changes at the coated and uncoated areas can thus be measured separately. A similar technique also shown in figure 2.12 uses a single beam reflected from two areas of a SPR sensor surface at different angles of incidence. Again this results in two intensity minima [71].

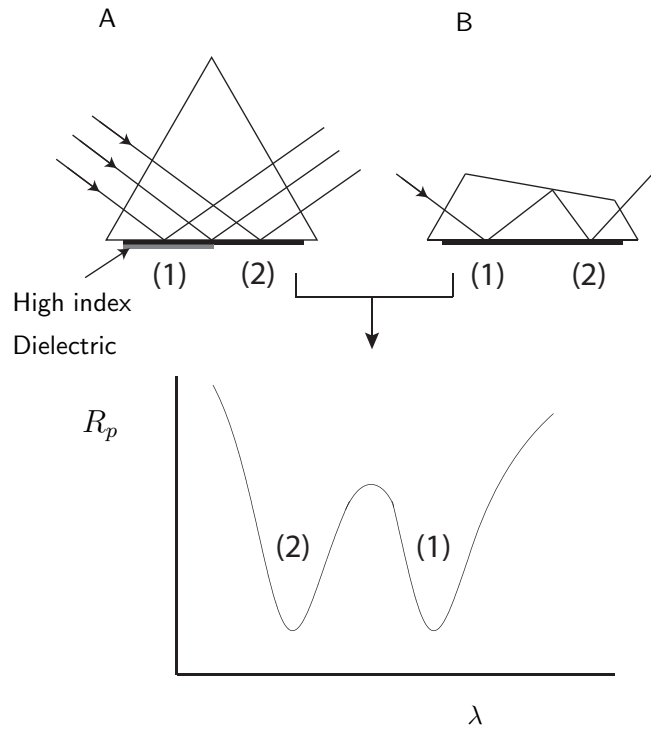


Figure 2.12: Self referencing by shifting one resonance. The shift in the resonance can be accomplished either by coating one channel with a thin high index layer (A) or by having the angle of incidence different for the two channels (B).

3 Imaging theory

This chapter describes the concept of the polarisation imaging SPR system and presents a theoretical analysis of its performance.

3.1 Concept

To make high sensitivity imaging SPR measurements, the technique chosen was to measure changes in polarisation due to the resonance. As described in chapter 2.3.1, it has been demonstrated by Hooper *et al.* that single channel SPR measurements can be made by measuring changes in the azimuth of the polarisation ellipse of light reflected from a SPR surface. As Hooper's instrument achieves high sensitivity and the theoretical modelling as presented later in this chapter suggested that good results could be obtained using a camera, a similar technique was selected for my instrument.

Figure 3.1 shows the concept of the polarisation imaging instrument. Light polarised at an azimuthal angle ψ from p-polarised is reflected from a Kretschmann configuration SPR prism. The light is then incident on a polarisation analyser with its transmission axis at an angle ϕ from p-polarised and the transmitted light is imaged onto a camera. The input polarisation azimuthal angle where the transmitted intensity is a minimum, ψ_m , is then found.

The transmission of the optical system can be found. The light starts linearly polarised at an azimuthal angle ψ from p-polarised so the electric field amplitude is

$$E = A(E_p, E_s) = A(\cos \psi, \sin \psi) \quad (3.1)$$

where E_p and E_s are the p-polarised and s-polarised components of E , and

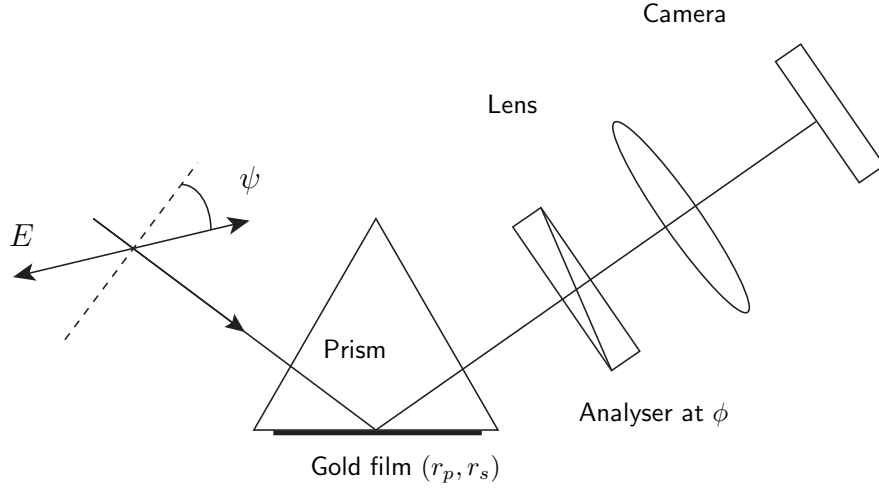


Figure 3.1: SPR polarisation imaging system concept

A is an arbitrary amplitude assumed to be 1 from now on.

The polarisation change when light is reflected from the SPR surface can be described by the complex reflection coefficients for p-polarised and s-polarised light, r_p and r_s , where the reflected electric field is equal to the incident field multiplied by the reflection coefficient. The complex reflection coefficients can be written in terms of their amplitude and phase as

$$r_p = |r_p|e^{i\delta_p}, \quad r_s = |r_s|e^{i\delta_s}, \quad \Delta = \delta_p - \delta_s, \quad (3.2)$$

where Δ is the difference in phase between r_p and r_s .

After reflection from the SPR surface the electric field is

$$E = (r_p \cos \psi, r_s \sin \psi) \quad (3.3)$$

The light is then incident on the analyser with its transmission axis at ϕ . The transmitted electric field is then

$$t = r_p \cos \phi \cos \psi + r_s \sin \phi \sin \psi. \quad (3.4)$$

The transmission (T) of the system, that is the intensity at the camera

divided by the intensity of the input light, is thus

$$T = |t|^2 = (r_p^* \cos \phi \cos \psi + r_s^* \sin \phi \sin \psi)(r_p \cos \phi \cos \psi + r_s \sin \phi \sin \psi), \quad (3.5)$$

$$\begin{aligned} T &= |r_p|^2 \cos^2 \phi \cos^2 \psi + |r_s|^2 \sin^2 \phi \sin^2 \psi \\ &\quad + |r_p||r_s|e^{-i\delta_p}e^{i\delta_s} \cos \phi \cos \psi \sin \phi \sin \psi \\ &\quad + |r_s||r_p|e^{-i\delta_s}e^{i\delta_p} \sin \phi \sin \psi \cos \phi \cos \psi, \\ T &= |r_p|^2 \cos^2 \phi \cos^2 \psi + |r_s|^2 \sin^2 \phi \sin^2 \psi \\ &\quad + |r_p||r_s|e^{-i\Delta} \cos \phi \cos \psi \sin \phi \sin \psi \\ &\quad + |r_s||r_p|e^{i\Delta} \cos \phi \cos \psi \sin \phi \sin \psi. \end{aligned}$$

Using $\cos \Delta = \frac{1}{2}(e^{i\Delta} + e^{-i\Delta})$ and $\sin(2\phi) = 2 \sin(\phi) \cos(\phi)$, this can be written as

$$T = |r_p|^2 \cos^2 \phi \cos^2 \psi + |r_s|^2 \sin^2 \phi \sin^2 \psi + \frac{1}{2}|r_s||r_p| \cos \Delta \sin(2\phi) \sin(2\psi). \quad (3.6)$$

The input polarisation for minimum or maximum transmission, ψ_m , can be found by finding the points where the derivative of $T(\psi)$ is 0.

$$0 = \frac{\partial T}{\partial \psi}(\psi_m), \quad (3.7)$$

$$\begin{aligned} 0 &= -2|r_p|^2 \cos^2 \phi \sin \psi_m \cos \psi_m + 2|r_s|^2 \sin^2 \phi \sin \psi_m \cos \psi_m \\ &\quad + |r_s||r_p| \cos \Delta \sin(2\phi) \cos(2\psi_m), \end{aligned}$$

$$0 = \sin 2\psi_m (|r_s|^2 \sin^2 \phi - |r_p|^2 \cos^2 \phi) + |r_s||r_p| \cos \Delta \sin(2\phi) \cos(2\psi_m). \quad (3.8)$$

Solving for ψ_m

$$\sin 2\psi_m (|r_s|^2 \sin^2 \phi - |r_p|^2 \cos^2 \phi) = -|r_s||r_p| \cos \Delta \sin(2\phi) \cos(2\psi_m), \quad (3.9)$$

$$\frac{\sin(2\psi_m)}{\cos(2\psi_m)} = -\frac{|r_s||r_p| \cos \Delta \sin(2\phi)}{(|r_s|^2 \sin^2 \phi - |r_p|^2 \cos^2 \phi)}, \quad (3.10)$$

$$\tan(2\psi_m) = -\frac{2|r_p||r_s| \cos \Delta \sin \phi \cos \phi}{|r_s|^2 \sin^2 \phi - |r_p|^2 \cos^2 \phi}. \quad (3.11)$$

As $\tan(2\theta) = \tan(2(\theta + n \times 90^\circ))$ (n any integer) there are minima and maxima 90° apart as expected. When calculating ψ_m , the maxima and minima can be distinguished by checking the intensity and the minimum closest to 0 used.

Instead, we could start with light with a fixed polarisation azimuthal angle ϕ then reflected off the SPR surface and incident on a rotatable analyser set with its transmission axis at ψ . This results in the same formula for the transmission, equation 3.5. As the transmission is the same the minima occur at the same ψ_m and the two measurements are equivalent. This second technique is that of measuring changes in the azimuth of the polarisation ellipse as by Hooper *et al.*. The minimum transmission occurs when the transmission axis of the analyser is aligned with the minor axis of the ellipse.

The input polarisation azimuthal angle for minimum transmission ψ_m depends on the reflection coefficients. As both the phase and amplitude of r_p change rapidly at the surface plasmon resonance, measuring ψ_m allows changes in the resonance due to refractive index changes at the surface to be detected. The rest of this chapter will present an analysis of how ψ_m changes due to refractive index changes and the effect of various experimental conditions on the expected accuracy of refractive index measurements made with this technique.

3.2 Simulations

To model the performance of the imaging system it is necessary to calculate the reflection coefficients of the SPR surface r_p and r_s . This can be done using the Fresnel equations and the scattering matrix method [19] as described in appendix A.

Thin film modelling using the scattering matrix method was done for a SPR system similar to that used for my experimental work. This system was a Kretschmann configuration with a 45 nm gold layer on glass ($n = 1.51$) with a 3 nm chromium layer and water as the sensed medium. The chromium layer was included as in my experimental work a ~ 3 nm chromium layer was used to improve the adhesion of the gold when vacuum depositing it on the glass substrate. The wavelength used was 680 nm, similar to that used in my experimental work.

The refractive index of the gold ($N = 0.161 + 3.64i$) is taken from fitting to data from the Handbook of Optical Constants of Solids [72] as described in appendix B. It is noted that the optical constants of thin, vacuum-deposited gold films depend greatly on the deposition conditions. Also these simulations ignore the effect of surface roughness and the fact that chromium can diffuse into gold [73]. These simulations are therefore meant to give estimates of the performance of the SPR system and to illustrate the effect of different conditions rather than to give precise results.

Figures 3.2 and 3.3 show the reflectance $|r_p|^2$, $|r_s|^2$ and phase change $\arg r_p$ and $\arg r_s$ for p-polarised and s-polarised light as a function of the angle of incidence. The surface plasmon resonance is clearly visible as the steep dip in the reflectance for p-polarised light with no corresponding change for s-polarised light. The minimum reflectance is $\sim 2\%$ as the gold film is slightly too thin for complete coupling to the plasmon. This minimum reflectivity is representative of that for my experimental work and the effect of changing the thickness will be discussed later in this chapter. The steep phase change at the resonance is also clearly shown.

The input polarisation azimuthal angle for minimum transmission ψ_m

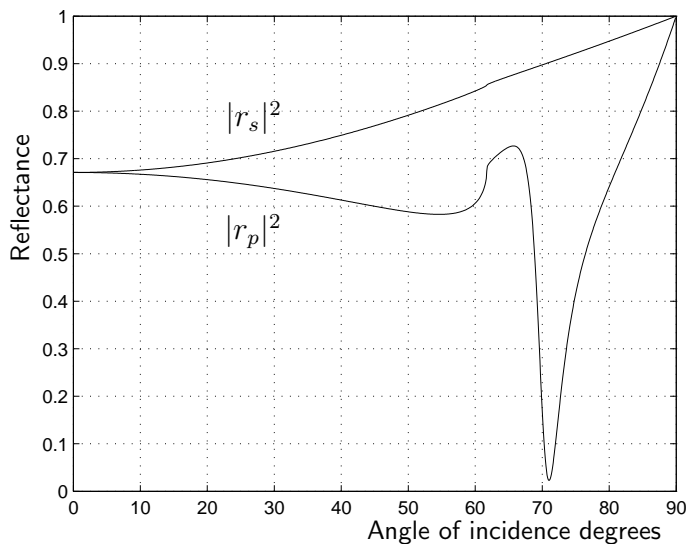


Figure 3.2: Reflectance vs angle of incidence

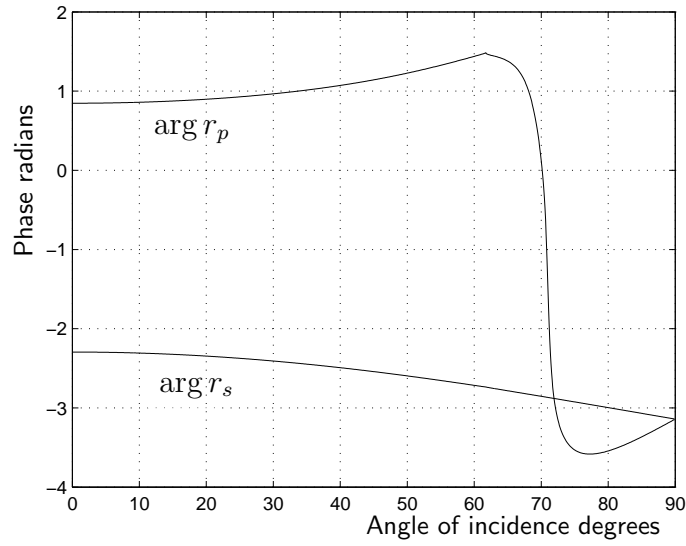


Figure 3.3: Phase change on reflection vs angle of incidence

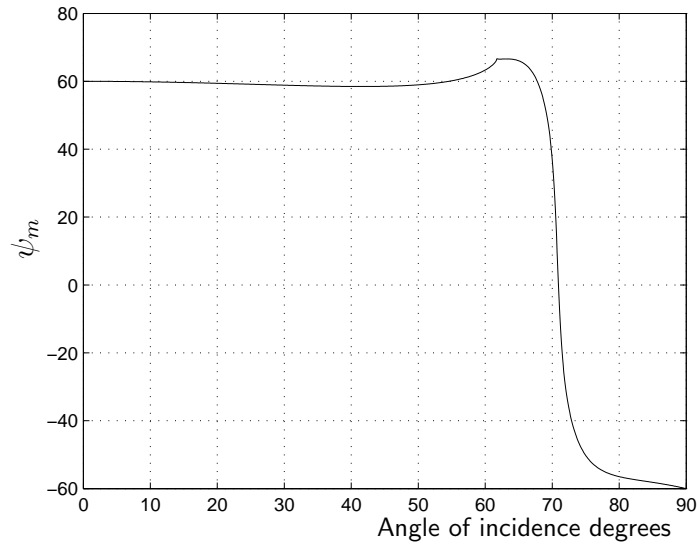


Figure 3.4: Input polarisation for minimum transmission ψ_m vs angle of incidence ($\phi = 30^\circ$).

when using this SPR system in the instrument presented at the start of this chapter can be calculated from equation 3.11. Figure 3.4 shows how ψ_m changes as a function of angle of incidence with the output polariser set at $\phi = 30^\circ$. Note that ψ_m changes steeply at the resonance.

A change in the refractive index of the sensed medium will shift the resonance and thus change ψ_m . Figure 3.5 shows how ψ_m changes as the refractive index changes from that of water for different settings of the output polariser ϕ . I assume the index is close to water $n = 1.33$ as the main application of SPR instruments is for sensing of aqueous solutions. The 0.01 refractive index range shown is reasonable for a SPR instrument. The angle of incidence is 71.5° .

As shown in figure 3.5 the sensitivity, that is the change in ψ_m per unit refractive index change, depends on the setting of the output polariser. This is shown more clearly in figure 3.6 where the sensitivity $d\psi_m/dn$ in degrees per RIU is shown as a function of the refractive index. As the output polariser approaches p-polarised, $\phi = 0^\circ$, the maximum sensitivity increases. However

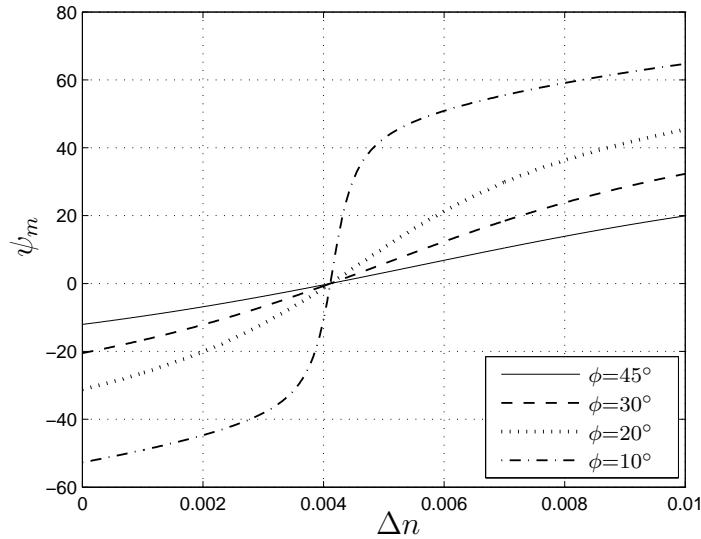


Figure 3.5: Input polarisation for minimum transmission ψ_m vs refractive index change ($n = 1.33 + \Delta n$), for different settings of the output polariser, ϕ .

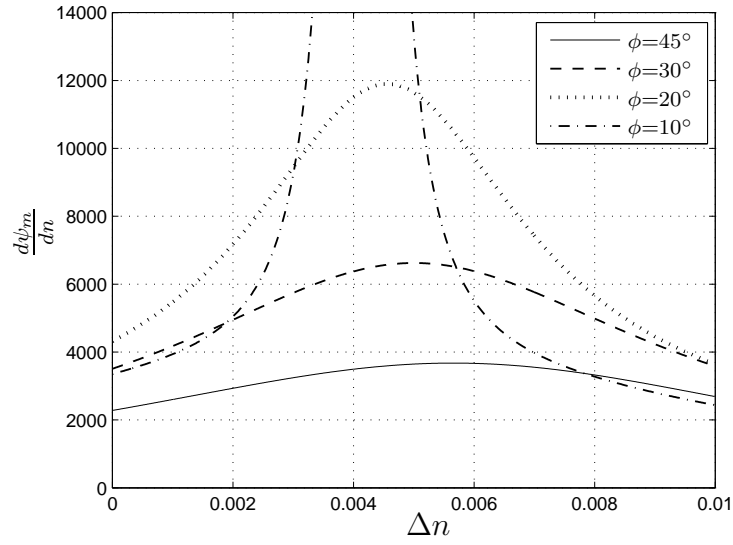


Figure 3.6: Sensitivity $d\psi_m/dn$ degrees per RIU vs refractive index change. The peak for $\phi = 10^\circ$ continues to 10^5 .

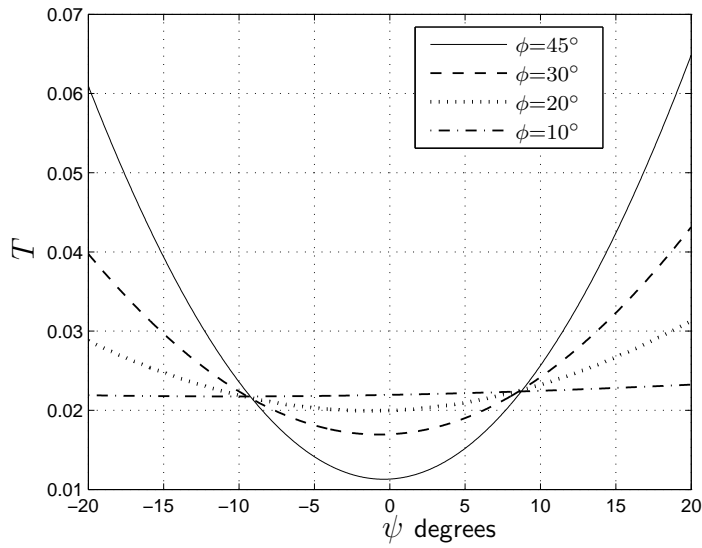


Figure 3.7: Transmission T vs input polarisation ψ at $n = 1.334$ and 71.5° angle of incidence.

the high sensitivity occurs only over a small refractive index range and the change in ψ_m with n becomes less linear.

While very high sensitivity can be obtained for suitable settings of the output polariser, they will not necessarily result in high accuracy when measuring refractive index changes. This is because ψ_m is not detected directly but rather the transmitted intensity is measured. To measure ψ_m , the input polarisation ψ can be scanned and the point of minimum transmission found. Figure 3.7 shows the transmission for a $\pm 20^\circ$ scan calculated from equation 3.6. The refractive index is $n = 1.334$, or approximately the sensitivity peak. As ϕ moves closer to zero the change in the transmission with change in ψ becomes smaller. This means that ψ_m will be more difficult to measure accurately in the presence of optical noise.

3.3 Noise

In this section I look at the effect of changing the output polariser setting ϕ in more detail by investigating the signal to noise ratio.

If elliptically polarised light is incident on an analyser, the transmission as the analyser is rotated will have the form of a sinusoid plus an offset. This can be shown by starting with elliptically polarised light with its azimuthal axis aligned with the x axis. This state can be formed by adding the electric fields of a circularly polarised component ($E = C(1\hat{x} + i\hat{y})$) and a linearly polarised component ($E = D\hat{x}$) to give

$$E = (D + C)\hat{x} + iC\hat{y} \quad (3.12)$$

where D and C are constants that determine the intensity and ellipticity. The electric field transmitted through a polariser with its transmission axis at an angle ν to the y axis will be

$$t = (D + C) \sin \nu + iC \cos \nu. \quad (3.13)$$

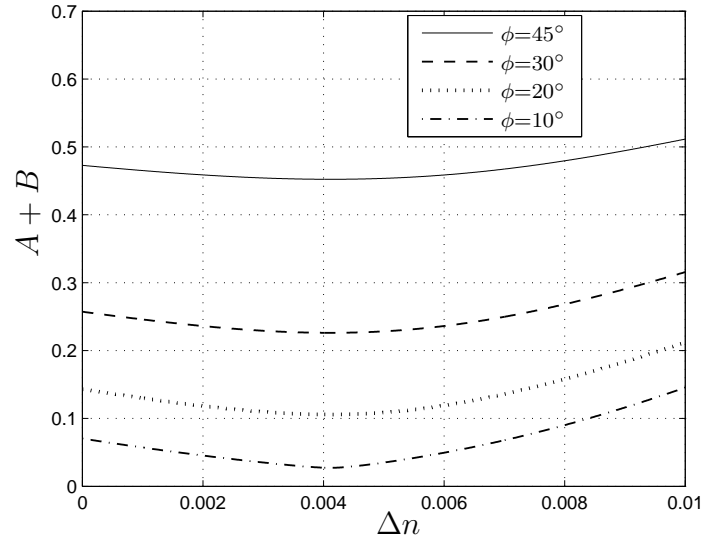


Figure 3.8: Maximum transmission $A + B$ vs refractive index change.

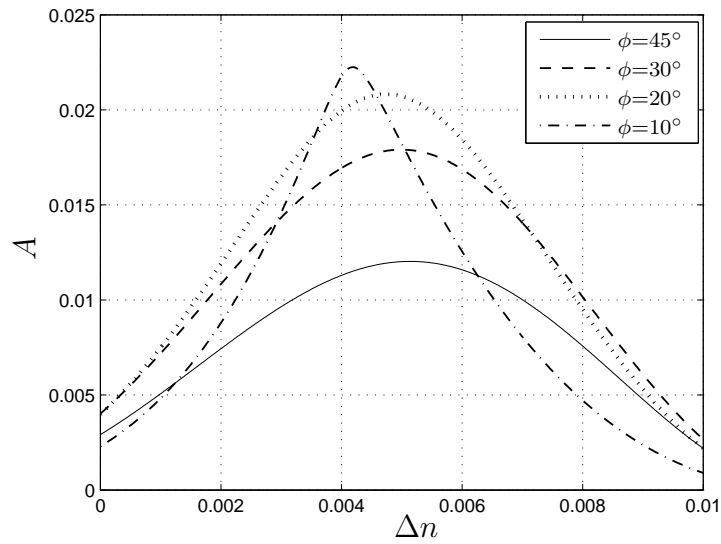


Figure 3.9: Minimum transmission A vs refractive index change.

So the transmitted intensity ($T = |t|^2$) is

$$T = (D + C)^2 \sin^2 \nu + C^2 \cos^2 \nu, \quad (3.14)$$

$$= ((D + C)^2 - C^2) \sin^2 \nu + C^2 (\sin^2 \nu + \cos^2 \nu), \quad (3.15)$$

$$= C^2 + ((D + C)^2 - C^2) \sin^2 \nu. \quad (3.16)$$

The equation for the transmission as a function of ψ (equation 3.4) is the same as if the input polarisation was fixed at ϕ and the analyser is now at ψ , as described in section 3.1. So the transmission as a function of ψ will be a sinusoid plus a constant offset. If we define $\theta = \psi - \psi_m$ then the transmission will be

$$T = A + B \sin^2 \theta, \quad (3.17)$$

where A is the minimum transmission ($\psi = \psi_m$, $\theta = 0^\circ$) and $A + B$ is the maximum transmission ($\psi = \psi_m + 90^\circ$, $\theta = 90^\circ$). Figures 3.8 and 3.9 show the maximum and minimum transmission vs refractive index for the same SPR system used in the previous section with different output polariser settings ϕ . The main effect of moving ϕ closer to 0° to achieve higher sensitivity is to reduce the maximum transmission.

3.3.1 The signal to noise ratio

As it is the transmission that is measured, the accuracy with which ψ_m can be determined will depend on the rate of change in the transmission with change in ψ and the noise of the transmission measurement.

The change in the transmission as a function of $\theta = \psi - \psi_m$, that is, the signal will be

$$S = \frac{\partial T}{\partial \theta} = B \sin(2\theta). \quad (3.18)$$

The signal to noise ratio of transmission measurements to find θ will thus be equal to S divided by the noise of the transmission measurement.

Note that this is the optical signal to noise ratio (optical signal / optical noise).

To measure the transmission, the transmitted intensity is measured. The accuracy of the intensity measurement may be limited by the photon statis-

tics of the light incident on the detector, that is the shot noise. The detection of photons is a Poisson process so the noise (1 standard deviation) in an intensity measurement is the square root of the number of photons detected. Defining I_E as the number of photons emitted in the measurement time and I_D as the number of photons arriving at the detector so that

$$T = \frac{I_D}{I_E}. \quad (3.19)$$

Note I_D, I_E are intensities measured as number of photons in the measurement time.

The noise in the transmission for a single shot noise limited measurement is then

$$N_{shot} = \frac{\sqrt{I_D}}{I_E}, \quad (3.20)$$

$$= \frac{\sqrt{I_E T}}{I_E}, \quad (3.21)$$

$$= \frac{\sqrt{T}}{\sqrt{I_E}}, \quad (3.22)$$

$$= \frac{\sqrt{A + B \sin^2 \theta}}{\sqrt{I_E}}. \quad (3.23)$$

It is assumed that I_E is already known or noiseless. As we are finding the minimum transmission only the relative transmission as ψ changes is needed.

So in the shot noise limit the signal to noise ratio is

$$\frac{S}{N_{shot}} = \frac{B \sin(2\theta) \sqrt{I_E}}{\sqrt{A + B \sin^2 \theta}}. \quad (3.24)$$

For this imaging instrument a CMOS camera will be used as the detector. The amount of light that can be detected per exposure is limited by the full well capacity of the pixels. The frame rate, that is the number of exposures per second, is also limited by the sensor electronics. The total amount of light that can be detected is quite limited with common CMOS cameras as the full well capacity is of the order of 100 000 photo-electrons per pixel. If the input power or the exposure length must be reduced to prevent the camera from saturating the noise in the intensity measurement will be the

same as if there was a noise source proportional to the intensity. The noise of the camera's output will be constant and equal to the shot noise of light incident on the camera during the exposure plus any intrinsic noise of the sensor. If the amount of light transmitted is now doubled the exposure must be halved or the beam attenuated by half. So the signal to noise ratio of the intensity measurement will be the same and the noise will have doubled. Let C_{SNR} be the signal to noise ratio of intensity measurements made by the camera. Then given that

$$T = \frac{I_D}{I_E}, \quad (3.25)$$

as before.

The noise in the transmission for a single saturation limited measurement of the transmitted intensity is

$$N_{sat} = \frac{I_D/C_{SNR}}{I_E}, \quad (3.26)$$

$$= \frac{I_E T}{I_E C_{SNR}}, \quad (3.27)$$

$$= \frac{T}{C_{SNR}}, \quad (3.28)$$

$$= \frac{\sqrt{A + B \sin^2 \theta}}{C_{SNR}}. \quad (3.29)$$

So when limited by the saturation of the camera, the signal to noise ratio for θ will be

$$\frac{S}{N_{sat}} = \frac{B \sin(2\theta) C_{SNR}}{A + B \sin^2 \theta}. \quad (3.30)$$

I assume that the accuracy with which the input polarisation for minimum transmission ψ_m can be determined is proportional to the signal to noise ratio at the value of θ for maximum SNR. We can find ψ_m by a quadratic least mean squares fit to some intensity measurements near ψ_m to find the point of minimum transmission. The transmission has a sinusoidal form and so should be well approximated by a parabola near a minimum. Intensity measurements at points where the intensity is changing rapidly as a function of angle have more effect on the fitted ψ_m than points where the intensity is changing less rapidly. So result for ψ_m from the fit will be dominated by the higher intensity points of the scan where the parabola is steeper. How

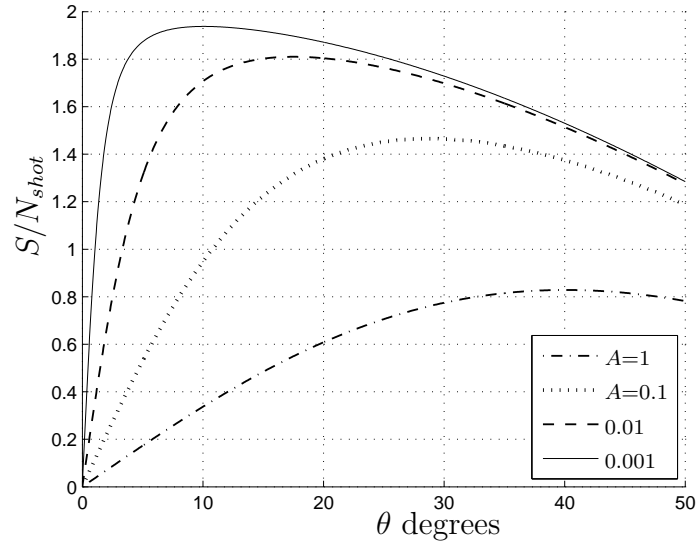


Figure 3.10: S/N_{shot} vs θ for $B = 1$, $I_E = 1$ and varying A . The maximum S/N_{shot} is quite similar to its value at $\theta = 22.5^\circ$

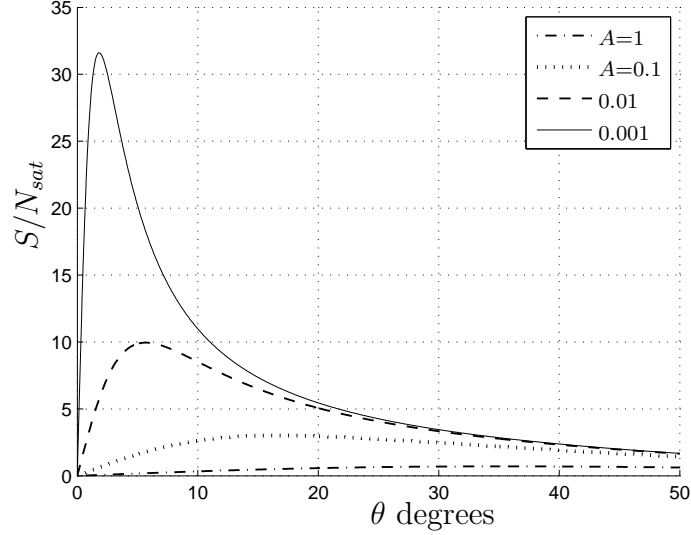


Figure 3.11: S/N_{sat} vs θ for $B = 1$, $C_{SNR} = 1$ and varying A . Note the much greater dependence on A compared to S/N_{shot} and that there is no θ for which S/N_{sat} is always close to the maximum for a given A .

good these points are in terms of intensity change per degree (signal) and noise gives us an idea of how accurate the fit will be. The range of θ values over which intensity measurements are made can be chosen such that the highest intensities recorded occur near the maximum signal to noise ratio. We can then compare the expected accuracy of the fits for different ϕ and see whether the change in fit accuracy cancels out the change in sensitivity $d\psi_m/dn$. This analysis could be done by modelling fitting a parabola to data of varying noise over a varying range, but I think that is unnecessarily complicated for an estimate.

For the shot noise limit case the maximum S/N_{shot} for varying θ , $S/N_{shot}|_{max}$ can be approximated by its value at $\theta = 22.5^\circ$ or $\pi/8$ radians as shown in figure 3.10 where S/N_{shot} is plotted for varying A . This approximation is used to simplify all further analysis

$$\frac{S}{N_{shot}}|_{max} \approx \frac{S}{N_{shot}}(\theta = 22.5), \quad (3.31)$$

where $S/N|_{max}$ indicates the maximum value of the S/N for all θ . The value of $\theta = 22.5^\circ$ was chosen as half of 45° and between the points of maximum SNR for the different A . For the saturation case the maximum S/N_{sat} is not well approximated by its value at a particular θ as shown in figure 3.11. Also S/N_{sat} is much more sensitive to A , the constant offset, than in the shot noise limited case. This is because A is the minimum transmission so as A increases, the intensity at the camera for a given input intensity increases. A value can be found for max S/N_{sat} using the approximation $\sin \theta \approx \theta$ to simplify finding the θ value at which the max S/N_{sat} occurs. This is equivalent to approximating $I(\theta)$ by a parabola near the minimum. Using this approximation

$$\frac{S}{N_{sat}} \approx \frac{2B\theta}{A + B\theta^2} C_{SNR}. \quad (3.32)$$

The θ value where S/N_{sat} is a maximum can be found by finding the point where the gradient of S/N_{sat} is 0

$$\frac{\partial \frac{S}{N_{sat}}}{\partial \theta} \approx \frac{2B(A + B\theta^2) - 4B^2\theta^2}{(A + B\theta^2)^2} C_{SNR}, \quad (3.33)$$

$$0 = 2B(A + B\theta_M^2) - 4B^2\theta_M^2, \quad (3.34)$$

$$\theta_M = \sqrt{\frac{A}{B}}, \quad (3.35)$$

where θ_M is the position at which the maximum S/N_{sat} occurs. At the point of maximum SNR θ_M , the transmission will be $2A$ (twice the minimum transmission). The maximum S/N_{sat} is then

$$\frac{S}{N_{sat}}|_{max} \approx \frac{2B\sqrt{\frac{A}{B}}}{A + B\frac{A}{B}}C_{SNR} = \sqrt{\frac{B}{A}}C_{SNR}, \quad (3.36)$$

This approximate result can be shown numerically to be accurate to 10 % when $A < B/5$. This condition ($A < B/5$) is true for all my results except for $\phi = 10^\circ$ near the sensitivity peak where $A > B$ and the result for the SNR will be too large.

3.3.2 SNR for measurements with different ϕ

The signal to noise ratio of measurements of ψ_m can now be calculated for the SPR system presented in section 3.2 from the calculated maximum and minimum transmission that are shown in figures 3.8 and 3.9. The SNR depends on the input intensity I_E and the camera's SNR C_{SNR} for the shot noise and camera saturation cases, respectively. These depend on the details of the measurement which will be described in the next two chapters. It will be shown in chapter 5.3 that for a typical single intensity measurement with my apparatus (a 0.001 second exposure and averaging a 5×5 group of pixels) these parameters are approximately $\sqrt{I_E} = 1.3 \times 10^4$ and $C_{SNR} = 500$. For the purpose of finding the optimum output polariser setting for refractive index measurements these can be treated as arbitrary constants. The formulas for the signal to noise ratios are for θ in radians so the results are multiplied by $180/\pi$ to give values for degrees. As the aim of measuring ψ_m is to detect changes in the refractive index n , the SNR for refractive index as detected by measuring ψ_m are found. These signal to noise ratios $S/N_{shot}(n)|_{max}$ and $S/N_{sat}(n)|_{max}$ are calculated from the SNR for ψ_m and the sensitivity $d\psi_m/dn$ in degrees of change in ψ_m per RIU as calculated in

section 3.2.

$$\frac{S}{N_{shot}}(n)|_{max} = \frac{d\psi_m}{dn} \times \frac{S}{N_{shot}}|_{max} \quad , \quad \frac{S}{N_{sat}}(n)|_{max} = \frac{d\psi_m}{dn} \times \frac{S}{N_{sat}}|_{max}. \quad (3.37)$$

Results for the shot noise limited case are presented first. Figure 3.12 shows signal to noise ratio for measuring ψ_m , $S/N_{shot}|_{max}$ for the different settings of the output polariser ϕ . As expected, it decreases as ϕ approaches 0° . The SNR for measuring n in the shot noise limit $S/N_{shot}(n)|_{max}$ is shown in figure 3.13. The best $S/N_{shot}(n)|_{max}$ is obtained for $\phi = 30^\circ$ but results for $\phi = 20^\circ$ and $\phi = 45^\circ$ are quite similar. The SNR obtained for $\phi = 10^\circ$ is very low as although the sensitivity is very high, the poor SNR for measuring ψ_m more than compensates for it. The SNR changes over the refractive index range and is highest in the middle of the range.

The SNR was also calculated for the camera saturation case. Figure 3.14 shows $S/N_{sat}|_{max}$ for the different settings of the output polariser ϕ . The $S/N_{sat}(n)|_{max}$ for the case is shown in figure 3.15. The results for $\phi = 20^\circ, \phi = 30^\circ, \phi = 45^\circ$ are very similar. So I expect that the accuracy of refractive index measurements will be similar over this range. The result

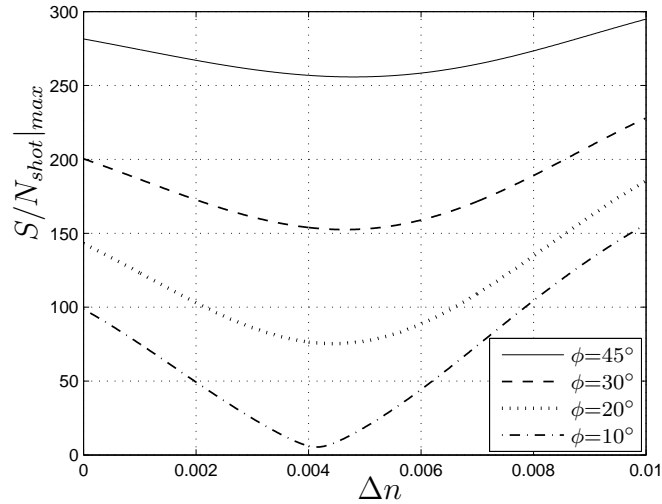


Figure 3.12: Signal noise ratio for the shot noise case $S/N_{shot}|_{max}$ vs refractive index change.

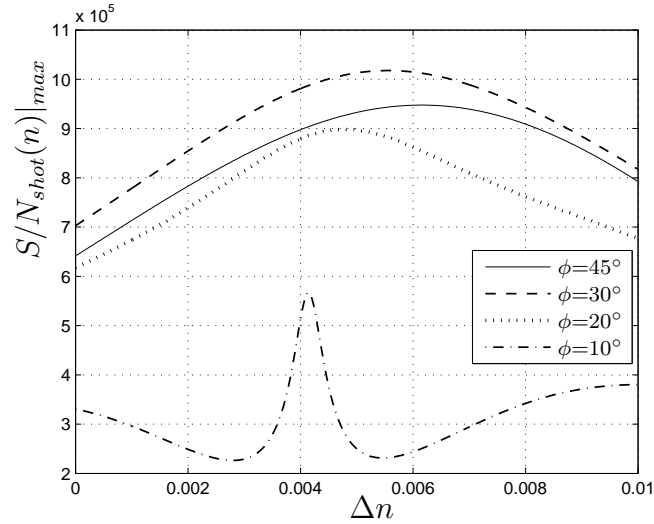


Figure 3.13: Signal noise ratio for the shot noise case when measuring n , $S/N_{shot}(n)|_{max}$ vs refractive index change.

for $\phi = 10^\circ$ is much lower except for a spike that is due to the limit of the approximations used when $A > B/5$. The peak $S/N_{sat}(n)|_{max}$ for $\phi = 10^\circ$ shown is 4.4×10^5 but at this point $A = 0.022$ and $B = 0.0051$ so the result for the SNR using the $\sin \theta = \theta$ approximation is not accurate. By plotting S/N_{sat} vs θ an accurate result for the peak $S/N_{sat}(n)|_{max}$ was found and it was 1.9×10^5 or similar to that for the other settings of the output polariser.

The conclusion for this section is that the output polariser setting may be varied from $\phi = 45^\circ$ to $\phi = 20^\circ$, with little change in the accuracy of refractive index measurements when limited by the shot noise and almost no change when limited by the camera saturation. The output polariser setting may thus be chosen based on other experimental conditions, closer to 45° to increase the linearity (ψ_m vs n) or closer to 20° to increase the sensitivity $d\psi_m/dn$ if the accuracy of the modulator is a limitation for example. The results for $S/N_{sat}(n)|_{max}$ are lower than those for $S/N_{shot}(n)|_{max}$ implying that for these values of I_E and C_{SNR} the measurement is limited by the camera saturation. The typical result for $S/N_{sat}(n)|_{max}$ from the plot is 2×10^5 or the noise in the refractive index measurement for a single 0.001 second intensity measurement would be $1/(2 \times 10^5) = 5 \times 10^{-6}$. These calculations will be repeated in chapter 5 using the measured properties of

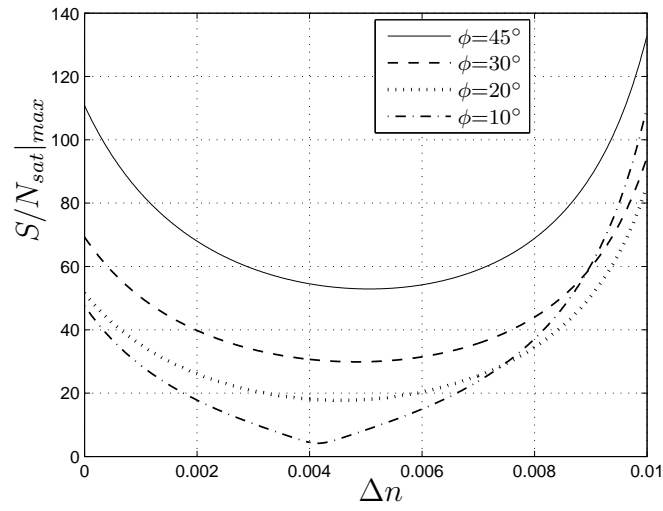


Figure 3.14: Signal noise ratio for the saturation case $S/N_{sat}|_{max}$ vs refractive index change.

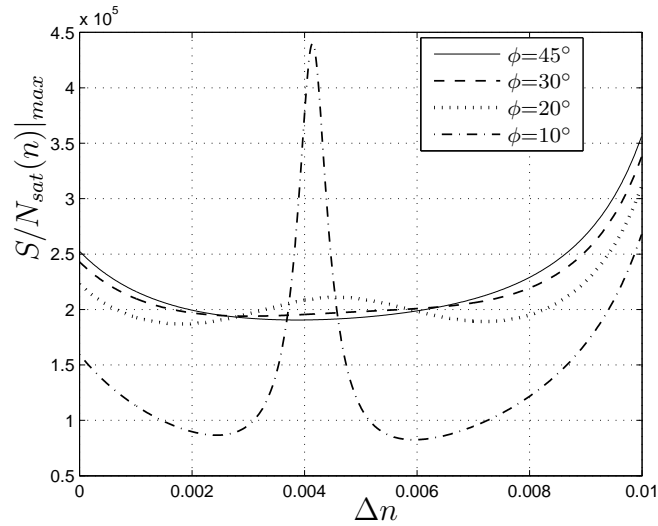


Figure 3.15: Signal noise ratio for the saturation case when measuring n , $S/N_{sat}(n)|_{max}$ vs refractive index change. The peak for $\phi = 10^\circ$ is due to the limitation of the approximation used the maximum should be 1.9×10^5 as explained in the text.

one of the SPR surfaces used and an estimate made of the expected accuracy of the imaging system.

3.4 Effect of changing the gold layer thickness

The thickness of the gold layer (t) has a significant effect on the surface plasmon resonance. Figure 3.16 shows the resonance for three gold thicknesses: 45 nm as for the results presented earlier, 50 nm which is close to the thickness that gives the deepest resonance (smallest minimum reflectivity) and 54.5 nm which is chosen to give a similar minimum reflectivity to 45 nm. The other properties of the SPR surface remain constant. Note the very low minimum reflectivity for 50 nm; the minimum value is $|r_p|^2 = 7.3 \times 10^{-5}$.

The input polarisation for minimum transmission ψ_m was calculated for these three gold thicknesses and is shown in figure 3.17. For all the results in this section an output polariser setting of $\phi = 30^\circ$ was used. The results for the three thicknesses have a very similar form. The sensitivity in degrees of change in ψ_m per RIU is thus very similar for different t . This suggests that the sensor should work for a range of gold thicknesses.

While there are only small changes in ψ_m due to different gold thicknesses, the minimum transmission A changes significantly, as shown in figure 3.18. The result for 45 nm is the same as presented earlier (figure 3.9). The result for 54.5 nm is the same as that for 45 nm in the middle of the refractive index range where $\psi_m = 0$, as the minimum reflectivity of the resonance is the same. As the index changes, however, the minimum transmission A increases rather than decreases. This was found from simulations of other thicknesses to be a general result. For gold films thicker than that to give the deepest resonance, A increases away from the resonance while for thin films it decreases to zero before increasing. The minimum transmission for 50 nm is very low in the middle of the refractive index range.

As described earlier when investigating the effect of changing ϕ , the minimum transmission A affects the signal to noise ratio when measuring ψ_m . So the thickness of the gold film may affect the accuracy of the refractive index measurements. The signal to noise ratios when measuring n for the

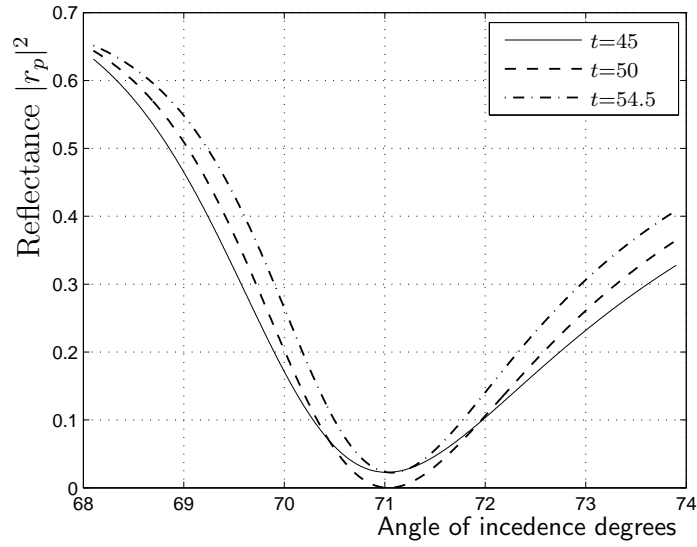


Figure 3.16: Reflectance $|r_p|^2$ for p-polarised light vs angle of incidence for 3 different gold thickness.

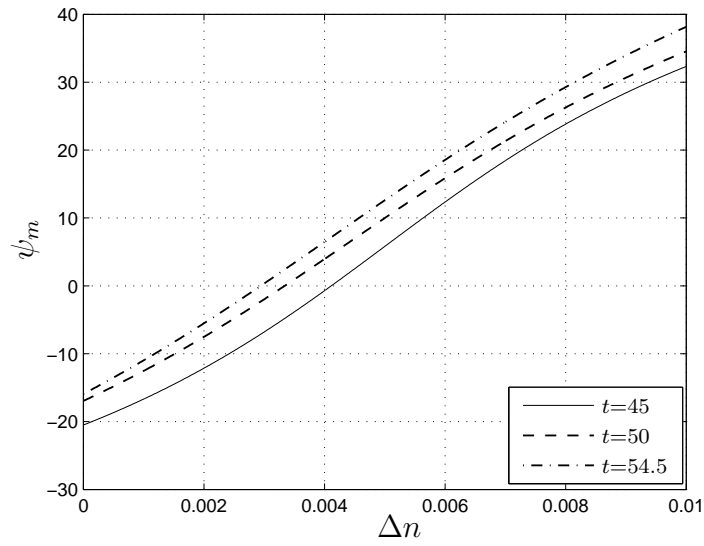


Figure 3.17: Input polarisation for minimum transmission ψ_m vs refractive index change. Results for three gold thickness are shown with $\phi = 30^\circ$.

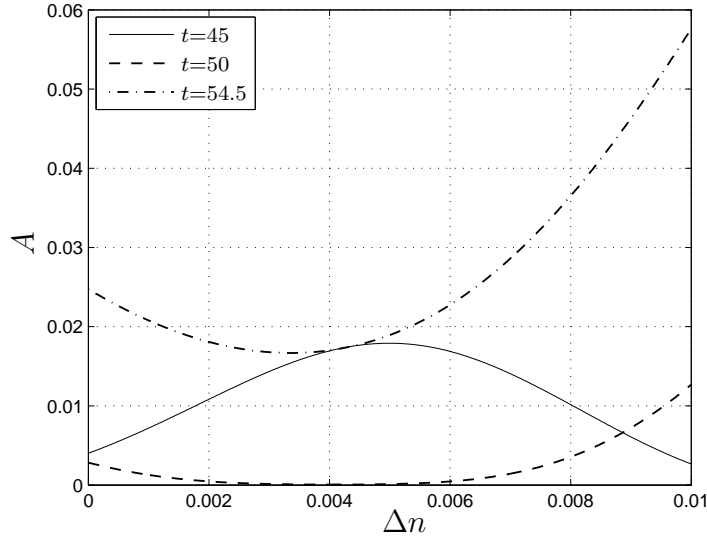


Figure 3.18: Minimum transmission A vs refractive index change. $\phi = 30^\circ$

shot noise case $S/N_{shot}(n)|_{max}$ and camera saturation case $S/N_{sat}(n)|_{max}$ case were calculated for the three gold thicknesses. These are plotted in figures 3.19 and 3.20. In the shot noise limit, there are only small differences in SNR so the thickness of the gold film will have a small effect on the accuracy with which refractive index changes can be measured. When limited by the camera's saturation the result is different; $S/N_{sat}(n)|_{max}$ is much higher for $t = 50$ nm where the very deep resonance causes A to be small. Obtaining high accuracy for low minimum reflectivity samples will require a high input power as there must be enough light to reach the camera saturation limit at the point of max SNR, which is at the point $T = 2A$. Note that $S/N_{sat}(n)|_{max}$ becomes larger than the result for the shot noise limit for the value of the input power used I_E . This also shows that the input power will have to be increased as shot noise is a fundamental limit on the accuracy.

The conclusions of this section are that small changes in the gold layer thickness around the value that gives the best coupling to the plasmon have little effect on the accuracy of refractive index measurements when limited by the shot noise. When limited by the camera saturation, optimising the gold layer thickness to reduce the minimum transmission appears to make much higher accuracy measurements possible. However, this requires a high

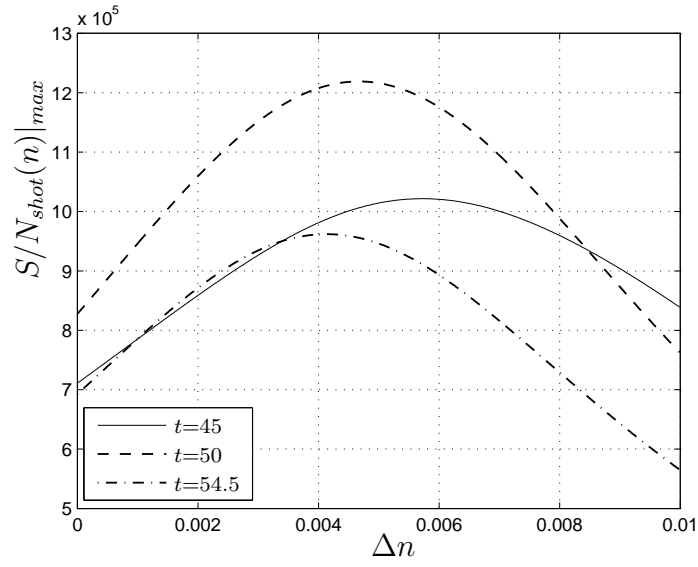


Figure 3.19: Signal to noise ratio for the shot noise limit $S/N_{shot}(n)|_{max}$ vs refractive index change.

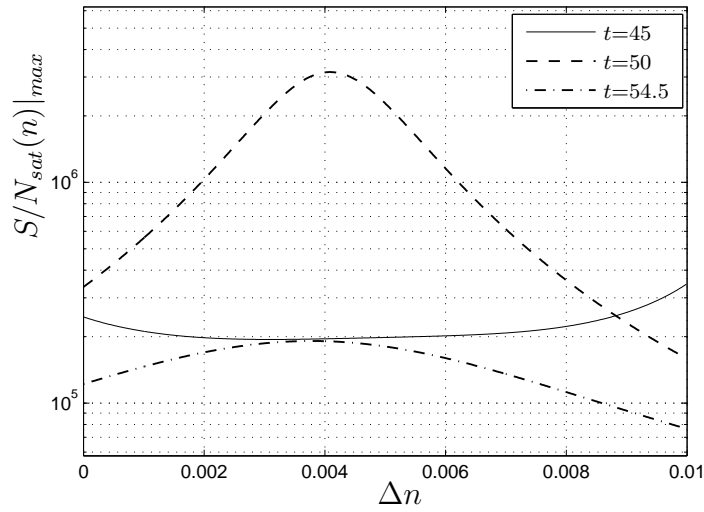


Figure 3.20: Signal to noise ratio for the camera saturation limit $S/N_{sat}(n)|_{max}$ vs refractive index change.

input power, and for a gold surface with roughness and other non-ideal characteristics the very low minimum reflectivity that high accuracy depends on may not be achieved. The use of a non-monochromatic source also increases the minimum transmission as described in the next section.

3.5 Wavelength

As will be described in the next chapter, a super luminescent diode was used as the light source rather than a laser to remove spurious interference fringes. This had an approximately 8 nm FWHM (full width half maximum) bandwidth and this may give different results than for a monochromatic source as has been assumed in all previous calculations. The reflectivity for an SPR surface on BK7 ($n = 1.51$) glass with 3 nm of chromium and 45 nm of gold as for the previous simulations was calculated for a light source with an 8 nm FWHM Gaussian bandwidth and a 680 nm centre wavelength. This was done by calculating the reflectivity for different wavelengths over a 660–700 nm range in 1 nm steps. The refractive index of gold at each wavelength was found from spline fits to data from the Handbook of Optical Constants [72] (see appendix B). The dispersion of the other materials was neglected. The results for different wavelengths were then averaged, weighted by a 8 nm FWHM Gaussian centred on 680 nm. The result, as well as that for a monochromatic source at 680 nm as previously calculated, is shown in figure 3.21. The result for the non-monochromatic source is similar except that the minimum reflectivity at the resonance is increased.

As described in the discussion of the gold layer thickness, increasing the minimum reflectivity at the resonance increases the minimum transmission when measuring ψ_m . The transmission for the range of wavelengths was calculated and the weighted average found in the same way as for the reflectivity. The transmission for a $\pm 20^\circ$ input polarisation ψ scan is shown in figure 3.22 with the result for a monochromatic source. The output polariser setting is $\phi = 30^\circ$ the angle of incidence is 71.5° and the refractive index is 1.334 or $\Delta n = 0.004$. As expected, the minimum transmission for the non-monochromatic source is larger and so the signal to noise ratio for measuring ψ_m in the camera saturation limit will be smaller. Also the input polarisation for minimum transmission ψ_m is different despite the centre wavelength

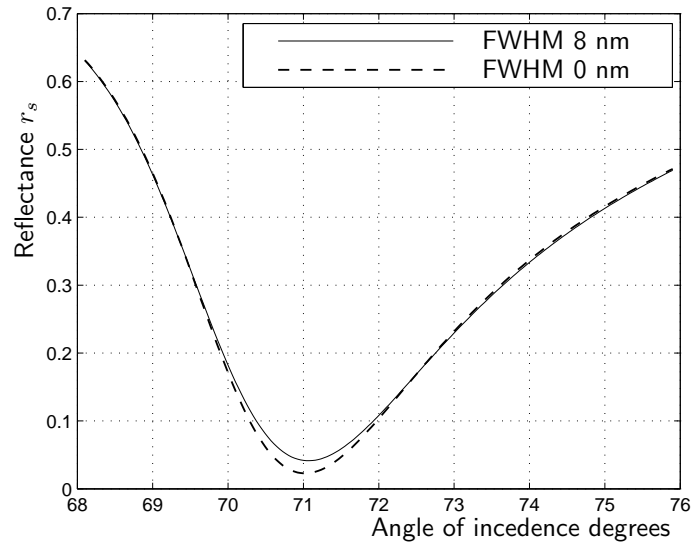


Figure 3.21: Reflectance vs angle of incidence for a monochromatic source and for one with a 8 nm FWHM Gaussian bandwidth

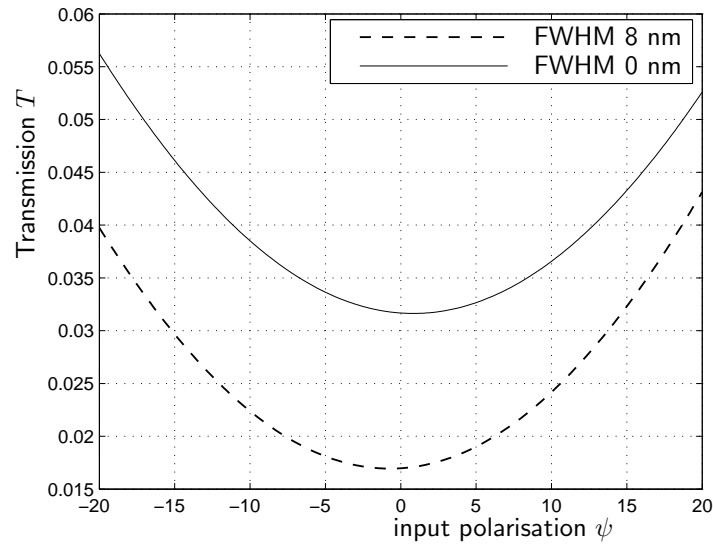


Figure 3.22: Transmission vs input polarisation for a monochromatic and non monochromatic (8 nm FWHM) light source. $\phi = 30^\circ$, $\Delta n = 0.004$, angle of incidence 71.5° .

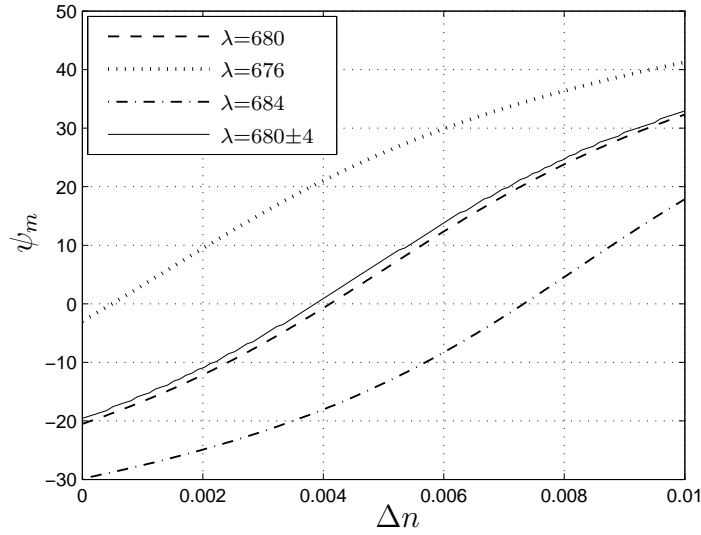


Figure 3.23: ψ_m vs refractive index change for three different wavelengths (676, 680 and 684 nm) and a non monochromatic source 680 nm centre wavelength 8 nm FWHM. $\phi = 30^\circ$ $n = 1.33 + \Delta n$ angle of incidence 71.5° .

being the same as for the monochromatic light source.

The change in ψ_m due to using a non-monochromatic source was calculated. To calculate ψ_m for the non-monochromatic source, the transmission was calculated for a range of ψ as for the previous figure and the minimum found. This calculation was repeated for each refractive index. The result for ψ_m vs the refractive index is shown in figure 3.23 with the results for monochromatic sources at 676, 680 and 684 nm also shown. The difference between the result for the non-monochromatic source and that for its centre wavelength is small. There is a large difference for different wavelengths so drift in the wavelength of the source used would cause significant errors.

From these results, it appears that a non-monochromatic source can be used for SPR measurements made by measuring ψ_m with the only major difference being a decrease of the signal to noise ratio for the camera saturation case due to the increase in the minimum transmission.

4 Imaging system apparatus

Overview

This chapter describes the experimental apparatus used for my polarisation imaging SPR system. The apparatus used is assembled on an optical table. Figure 4.1 shows the equipment used and the arrangement on the optical table. A beam from a super luminescent diode (SLD) is passed through a polariser and a Faraday effect polarisation modulator to control the azimuthal angle (ψ) of the light incident on the prism. After being expanded and collimated the beam is reflected from a Kretschmann configuration SPR surface; a prism with a gold coated microscope slide index matched to it. A flow cell clamped to the microscope slide allows solutions with different refractive indices to be flowed over the SPR surface. The reflected light is analysed by a polarisation analyser and focused onto a CMOS camera. The

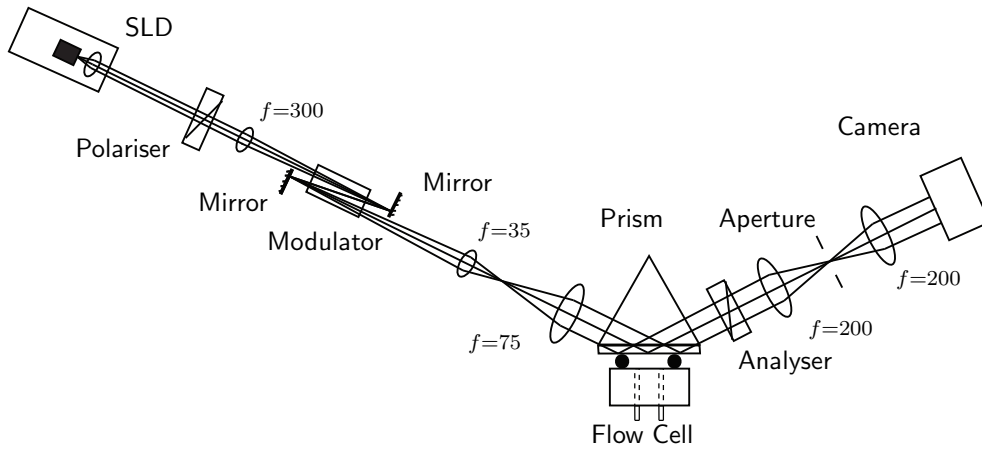


Figure 4.1: The experimental apparatus.

modulator is scanned and the input polarisation for minimum transmitted intensity (ψ_m) is found for each channel of the image.

4.1 Apparatus Details

4.1.1 Light source

The light source used was a super luminescent diode (SLD), the QSDM680-9 from Q Photonics, centre wavelength 677 nm, spectral width 7.5 nm FWHM. Originally a helium neon laser was used as the light source but gave poor performance due to spurious interference fringes. Interference fringes caused by reflections from a glass plate on the front of the camera produced a 20% modulation of the detected intensity but were quite stable. Interference fringes produced by reflections due to imperfect index matching at the prism slide interface were much less visible but caused fringes in the polarisation image and drifted significantly with time. The SLD was used as its much shorter coherence length removed these fringes. The diode was mounted in a temperature controlled laser diode mount with an aspheric collimation lens. The diode was driven by a constant current supply with a typical current of ~ 190 mA giving an output power of ~ 4 mW.

4.1.2 Modulator

A Glan-Thompson polariser is used to fix the polarisation state before the modulator. This polariser is mounted in a Newport SR50 rotation stage with a resolution 0.001° and absolute accuracy of 0.03° . The stage is controlled via a PC through a Newport ESP300 motion controller/driver.

The output of the SLD is polarised and it was mounted with its output approximately p-polarised. The polariser is usually set with its transmission axis near p-polarised so most of the light was transmitted.

The polarisation of the beam is controlled using a Faraday effect modulator. The Faraday effect is the rotation of the polarisation of light in a magneto-optic medium, in the presence of a magnetic field [74]. The rota-

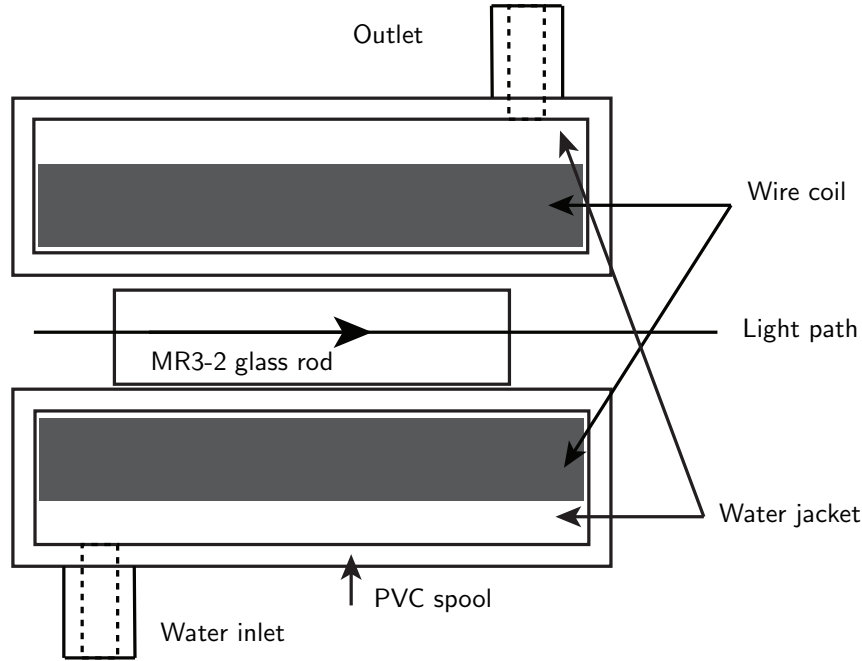


Figure 4.2: Cross section of the polarisation modulator.

tion is given by the equation

$$\theta_F = \mathcal{V}Bd, \quad (4.1)$$

where θ_F is the rotation of the polarisation, B is the magnetic field in the direction of the propagation of the light, d is the distance the light travels in the medium and \mathcal{V} is the Verdet constant of the medium. For my modulator, the active material is a 30 mm long, 5 mm diameter rod of MR3-2 terbium doped borosilicate glass from Xi'an Aofa Optoelectronics Technology Inc, Xi'an China. This glass is paramagnetic with a Verdet constant $\mathcal{V} = -96$ rad T⁻¹m⁻¹ at 633 nm and $\mathcal{V} = -31$ rad T⁻¹m⁻¹ at 1064 nm, both at 20°C.

The rod was placed within a ~ 700 turn coil of 0.45 mm insulated copper wire, wound around a PVC plastic spool made by the Physics Department mechanical workshop. The magnetic field in the rod will be proportional to the current in the coil. Approximating the coil by a long solenoid, the field in the rod is

$$B = \frac{\mu_0 NI}{h} \quad (4.2)$$

where μ_0 is the permeability of free space, N is the number of turns in the coil, I is the current in the coil and h is the length of the coil. As the length of the coil is 40 mm, significantly greater than the length of the rod, the effect of the fringing field will be small.

The coil was driven by a voltage ramp generated by a data acquisition card in the PC used to control the system, and connected to the coil through an amplifier. The data acquisition card used was a Measurement Computing PC1001 with a 12 bit digital-to-analogue converter. The amplifier was a simple inverting op-amp circuit [75] constructed using a National LM12 high power op-amp. This was powered by a ± 30 V supply and was capable of outputting up to ± 27 V at ± 6 A. The resistance of the coil was $4\ \Omega$, so running it at maximum power 24 V and 6 amps would dissipate 144 W. Using a linear scan from +6 amps to -6 A and a 50% duty cycle (scanning half the time, idle the other half), the maximum scan range and duty cycle for my measurements, gives an average power of 24 W. It is thus clear that the heat dissipated in the coil is substantial and cooling was needed. The coil was cooled with a water jacket around the spool to maintain an acceptable temperature. A cross section of the modulator showing the glass rod, coil and cooling jacket is shown in figure 4.2. Water flowing through the jacket was found to maintain a stable temperature at the rod of $\sim 15^\circ\text{C}$ above ambient for ~ 24 W average power.

To increase the available rotation, two small mirrors were used to reflect the beam so that it passed through the rod three times. With 3 passes through the modulator, the maximum ± 6 amp scan resulted in a $\pm 45^\circ$ polarisation scan. A 300 mm focal length lens is used to focus the beam to a waist near the modulator. The small diameter of the beam near the modulator made it easier to separate the 3 beam paths.

A $\sim 0.25\ \Omega$ resistor made by paralleling 6 high power resistors was placed in series with the coil. The voltage across this resistor was monitored by one of the 12 bit analogue-to-digital inputs of the data acquisition card. The resistor voltage will be proportional to the current in the coil and thus the polarisation rotation of the beam through the modulator. The temperature of the glass rod will be different for different measurements due to variations in room temperature and the use of different scan ranges, resulting in a different average power in the coil. As the Verdet constant is expected to have

a $1/T$ temperature dependence for this paramagnetic material [74, 76], the relationship between the resistor voltage and the polarisation change will be temperature dependent. A calibration measurement of the relationship between the resistor voltage and the polarisation rotation was thus made at the end of each set of imaging measurements. This was done by comparing the effect of the modulator to the effect of rotating the input polariser and will be described in section 4.2.2. The precise Verdet constant, length of propagation in the glass rod, details of the coil and the exact value of the current measuring resistor do not need to be known as they are thus calibrated for.

After the modulator, the beam was expanded and collimated using two lenses with focal lengths of 35 and 70 mm. The total power incident on the prism was ~ 2.5 mW and the power in the area of the beam imaged onto the camera was 0.6 mW.

4.1.3 Prism and flow cell

The expanded beam was coupled, via a prism, to a Kretschmann arrangement consisting of a microscope slide coated on one side with a thin gold film in contact with a temperature controlled flow cell. Figure 4.3 shows the arrangement of the SPR system and the flow cell.

A high index (SF2 glass $n = 1.64$) prism was used to reduce the external angle of incidence at which the SPR resonance occurred. This made the alignment easier and reduced the stretching of the image due to the oblique angle the slide is viewed at. The gold films were deposited on microscope slides ($n = 1.50$). The slides were cleaned with *aqua regia*, rinsed with distilled water and then wiped with lens tissue and methanol. Following this, they were coated with a 3 nm adhesion layer of chromium and ~ 40 nm of gold by thermal evaporation in a vacuum coater. Index matching oil (Cargile $n = 1.51$) between the prism and the slide was used to reduce unwanted reflections from this interface.

The prism and slide were clamped to an aluminium block. A 20 mm diameter O-ring in a groove cut into the block was used to create a watertight space between the slide and block. Depending on how tightly the prism was clamped, this space was 0.5 to 1 mm thick or approximately 0.15 to 0.3 ml in volume. Two holes drilled through the block with plastic pipe fittings on

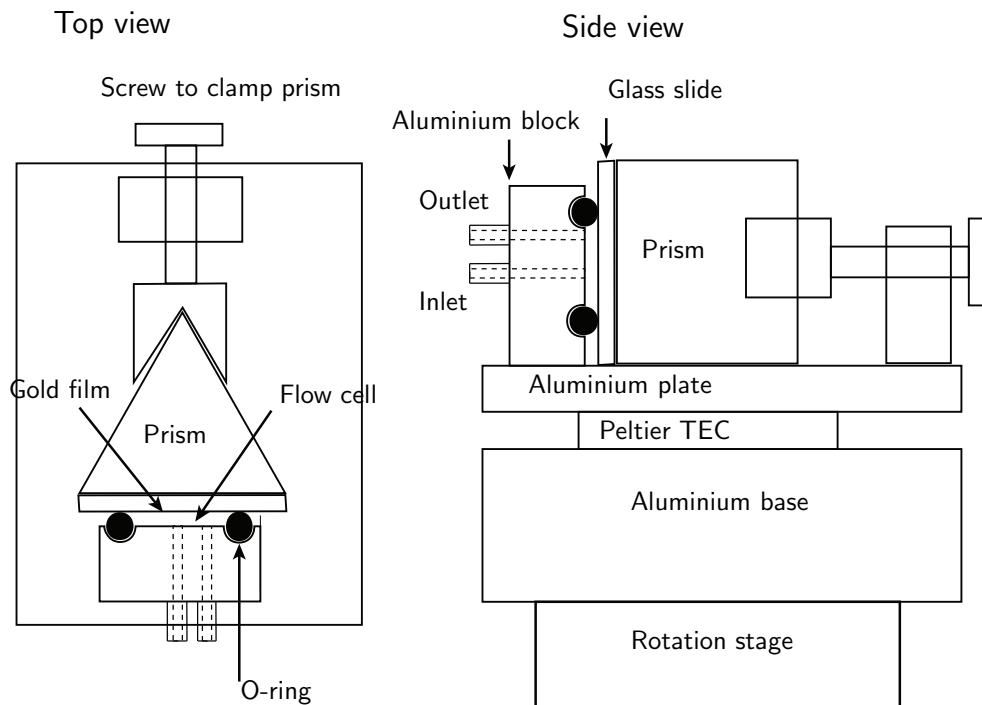


Figure 4.3: The prism and flow cell.

the outside formed the inlet and outlet. The flow cell inlet was connected through two 4–1 selector valves to up to seven plastic 60 ml syringes that could contain salt solutions or pure water with different refractive indices. The syringe to valve and flow cell connections were made with Tygon R-3603 Laboratory Tubing 1.6 mm ID. A tube from the outlet of the flow cell led to a waste bucket. When changing the solution in the flow cell, at least 5 ml of the new solution was flowed through the cell to ensure the previous solution was completely replaced.

The flow cell and prism clamp were mounted on an aluminium plate. This plate was attached to a aluminium base with nylon bolts. A Peltier thermoelectric cooler (TEC) between the base and plate driven by a PID controller allowed the temperature of the flow cell to be controlled. A thermistor bolted to the plate provided feedback for the temperature controller. The aluminium base was mounted on top of a SR50 rotation stage, as used for the input polariser, to allow the angle of incidence to be accurately controlled. The aluminium flow cell and mount were made by the Physics Department

mechanical workshop.

4.1.4 Analyser

A rectangular aperture between the prism and the analyser blocks light reflected at the prism-slide interface. The polarisation analyser is a 25 mm polarising cube beam splitter. This was clamped on top of a prism table mounted such that it could be rotated to set the analyser angle (ϕ). For measurements with different values of ϕ , the analyser was adjusted by setting the polariser to $\phi + 90^\circ$, moving the analyser on the optical table so that it was directly before the polariser and manually rotating the analyser until the light transmitted through the polariser was extinguished.

4.1.5 Camera

The camera was a Silicon Video 642M monochrome CMOS camera. This camera uses a Micron MT9V403 sensor with 640×480 resolution at 8 or 10 bits per pixel and up to 204 frames per second (fps) for the full frame. The PCI capture card included with this camera was mounted in the PC used to control the SPR imaging system. The full well capacity (pixel saturation level) was 110 000 photoelectrons. The camera pixel size is $10 \times 10 \mu\text{m}$ and the active area of the sensor is $6.4 \times 4.8 \text{ mm}$.

It was found that when this camera was run at high frame rates in the 10 bit mode, some frames were not recorded and appeared in the output as arrays of zeros. This is believed to be due to limitations of the PCI bus. The 8 bit mode sends one byte per pixel and the 10 bit mode two, so the data transfer rate is twice as high. At 200 fps and 2 bytes per pixel the data rate is 117 MBs^{-1} , very close to the 133 MBs^{-1} limit of the PCI bus used. The 8 bit mode was therefore used for my measurements. This did not significantly increase the noise as the intensity was generally such that the shot noise was larger than the quantisation noise.

For the results presented, the camera was run at 640×240 resolution. This doubled the maximum available frame rate. Also the aspect ratio of the area of the sensor used compensated for the stretching of the image due to the slide being viewed at an oblique angle. This resulted in an approximately

square area of the slide being imaged.

Measurements of the camera's noise and linearity were made and will be presented in the next chapter.

4.1.6 Imaging optics

Two 200 mm focal length doublet lenses were positioned to give a focused image and collimated beam on the camera with a magnification $M = 1$. A circular aperture at the beam waist sets the resolution (R) and depth of field (dof) of the optics. For the imaging results with patterned surfaces presented later in this thesis, a 3.5 mm diameter aperture was used giving $R = 47\mu\text{m}$ and $\text{dof} = 8.9\text{mm}$. This large depth of field was needed as a tilted surface was being imaged. Polarisation measurements were made by averaging 5×5 pixel square areas that were approximately the same size as the resolution of the imaging optics. The filtering of high spatial frequency components due to the aperture seemed to reduce the (temporal) drifts in the polarisation measurements. The propagation length of the surface plasmons (1/e intensity decay) for gold at 680 nm is $\sim 5 \mu\text{m}$ (see section 2.1) so this does not affect the resolution of the system.

4.2 Imaging Measurements

4.2.1 Data Acquisition

A Matlab program running on the PC containing the camera control and data acquisition cards is used to control the experiment.

The camera is set to a 1 ms exposure and to be triggered by a square wave source connected to its control card's external trigger input. For all the imaging results that will be presented, the camera was run at 280 fps. The square wave source is also connected to the trigger input of the data acquisition card to allow the voltage across the current measuring resistor to be sampled at the time of the exposure.

To generate each polarisation image, the polarisation modulator is scanned while images are recorded. A quadratic fit to the recorded intensity values is

used to find the input polarisation that gave the minimum intensity for each channel of 5×5 pixels.

The Matlab program first calls a Matlab mex function implemented in C++ . This function first sets the modulator to the start of the polarisation scan by setting the DAC output of the data acquisition card connected to the modulator input. The start of the modulator scan is selected by an input to the function to give a polarisation rotation of up to $\pm 40^\circ$ selectable in $\pm 5^\circ$ increments. The camera then starts recording a sequence of 280 images to a memory buffer. As each image is recorded, the DAC output to the amplifier is incremented to scan the polarisation. The amount by which the DAC output is incremented is proportional to the starting value such that over the 280 image sequence the polarisation is scanned from positive to negative. A 10 Hz RC low pass filter between the DAC output and the amplifier smooths the transitions resulting in an almost linear scan centred on 0. Also, for each image the ADC input of the data acquisition card records a sequence of 100 measurements of the current measuring resistor voltage over a 1 ms interval coinciding with the camera exposure. After the image sequence is complete, 5×5 groups of pixels are summed to give a sequence of $280 \times 128 \times 48$ channel intensity images. The 100 voltage measurements for each image are also summed to find the average voltage during that exposure. The sequence of images and average voltages is returned.

Only the intensity results where the average for that 5×5 channel was between 5 and 150 out of the maximum of 255 were used as the camera is non-linear near zero and full scale. The non-linearity of the camera will be measured and explained in more detail in the next chapter. For each of the 128×48 channels, the resistor voltage for minimum intensity is then found by a quadratic least mean squares fit to the intensity vs voltage. Figure 4.4 shows the results of a typical scan for a 5×5 pixel channel. The choice of 5×5 pixel channels was because averaging larger areas did not significantly improve the accuracy, while using a larger number of smaller channels reduced the accuracy and resulted in an unacceptable increase in the time taken to calculate the polarisation image.

The acquisition time is 1.1 s and it takes approximately another second to perform the fitting, yielding a total measurement time of ~ 2 s. It is expected that with better programming, the fitting time could be significantly reduced

and that it could be done in parallel with the acquisition.

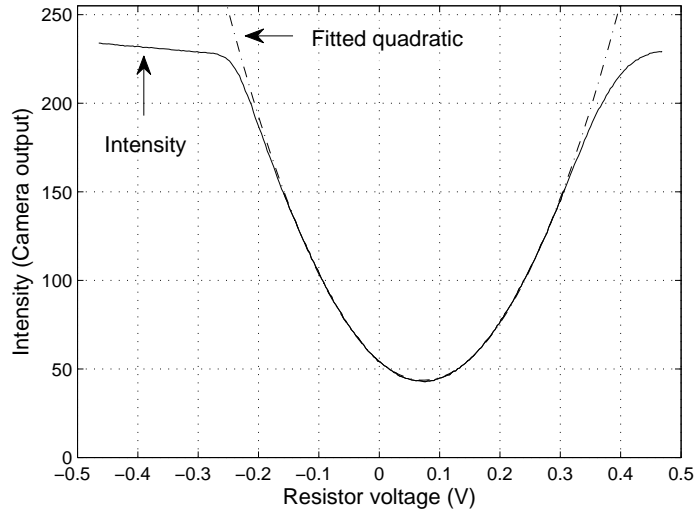


Figure 4.4: Intensity vs resistor voltage for a typical scan and the fitted quadratic. The input polarisation was scanned $\pm 20^\circ$, centred on -10° with the output polariser set at 45° . The intensity is the mean value for a 5×5 group of pixels. The camera can be seen to saturate at high intensities.

4.2.2 Calibration

To convert the fitted resistor voltage value into the azimuthal angle of the light leaving the modulator, a calibration measurement must be made. For a given, arbitrary sample, minimum intensity occurs when the light leaving the modulator has azimuthal angle ψ_m . If the input polariser is then moved, the modulator current must be adjusted in order to maintain the same polarisation state at the output of the modulator and hence minimum intensity. So the resistor voltage change corresponding to a 1° polarisation rotation change can be found by rotating the polariser 1° . This calibration was done at the end of each set of imaging measurements and examples will be given with the imaging results presented in chapter 6.

5 Expected sensor performance

The accuracy with which refractive index changes can be detected by the SPR imaging instrument described in the previous two chapters will depend on the properties of the gold SPR surface and the performance of the camera. The noise and linearity of intensity measurements made with the camera were measured by comparing them to those made with a photodiode and the results are presented in section 5.1. The reflectivity and polarisation change on reflection of a gold coated microscope slide, from the same batch used in the SPR imaging results presented in the next chapter, were measured and are presented in section 5.2. In section 5.3, the results of the previous two sections are used to calculate the signal to noise ratio in the same way as for the theoretical results presented in chapter 3.3. The signal to noise ratio is then used to estimate the accuracy of refractive index measurements using the imaging system.

5.1 Camera noise and linearity

To measure the noise and linearity of the camera a controllable intensity light source was needed. This is shown in figure 5.1. The beam from the super luminescent diode (SLD) was directed through a polariser, the Glan-Thompson in its SR50 rotation stage, and then through a fixed polarisation analyser, the polarising beam splitter. Rotating the polariser would change the intensity while the polarisation of the output beam remained constant. The beam was then focused with a lens through a 1 mm aperture to spatially filter it, and allowed to expand. The camera was placed in the beam at a

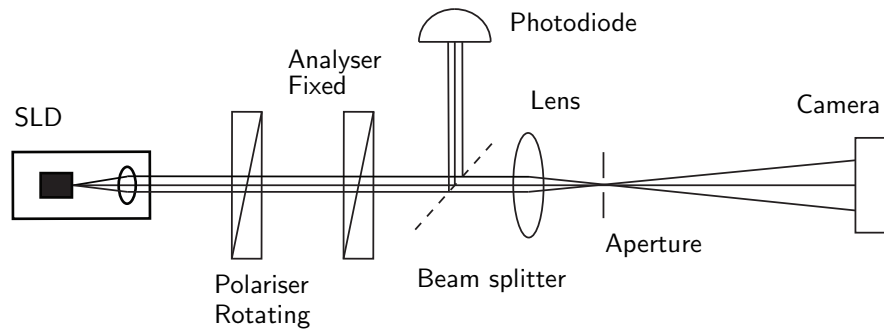


Figure 5.1: Apparatus for measuring the noise and linearity of the camera.

point where the beam was much larger than the active area of the sensor so that the illumination was approximately uniform. An uncoated, cleaned microscope slide was used as a beam splitter and placed in the beam between the analyser and the lens. The beam reflected by the slide could be monitored by the photodiode of a Newport 1815-C power meter via the data acquisition card (DAQ). The manufacturer specifies the linearity of the power meter's 818-SL photodiode as $\pm 0.5\%$.

To measure the camera's performance, the polariser was scanned while the intensity was recorded with both the camera and power meter. For each position of the polariser, data were acquired using the same Matlab mex function code as for the polarisation imaging instrument. A sequence of 275 images was recorded over a 1 second interval with 1 ms exposure times. For these measurements only a 40×20 channel area was recorded where each channel is a 5×5 pixel area. The data acquisition card samples 99 times during each exposure and the average is recorded.

The intensity change as the polariser is scanned as recorded by the power meter is shown in figure 5.2. The analyser was not set to any particular angle so the position of the minimum is not significant. Near the null, the intensity is well fitted by a parabola as expected. Figure 5.3 shows the intensity measured with the camera. For each setting of the polariser, the average intensity for 275 exposures I , of one 5×5 pixel channel is shown. At high intensity the camera saturates. At low intensity, zero is recorded

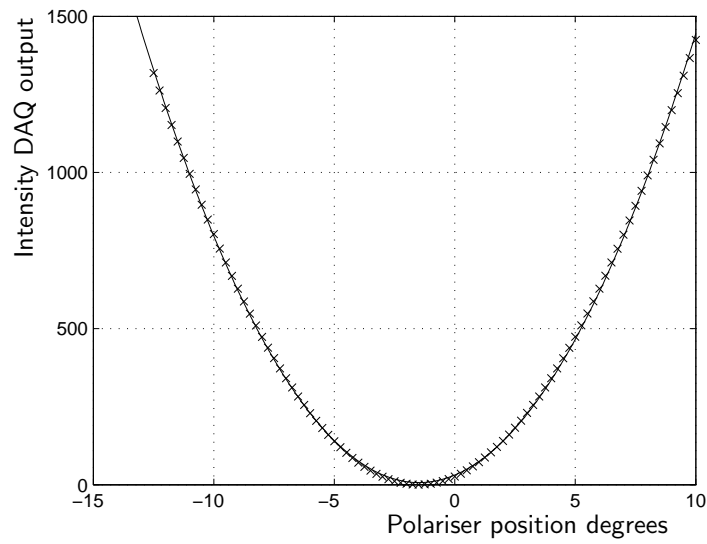


Figure 5.2: The intensity as measured by the power meter as the polariser is scanned. A parabola is fitted to the data.

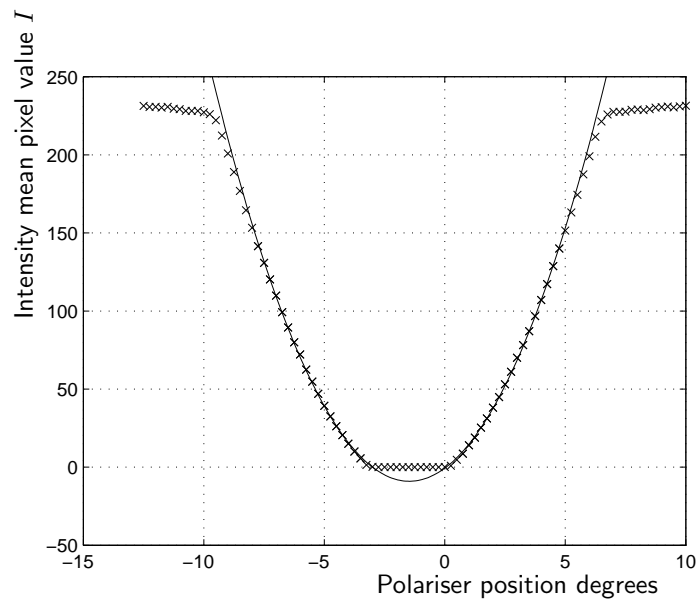


Figure 5.3: The intensity as measured by the camera (mean pixel value I) for the same polariser scan as the previous figure. A parabola is fitted to the data where the intensity is between 5 and 150.

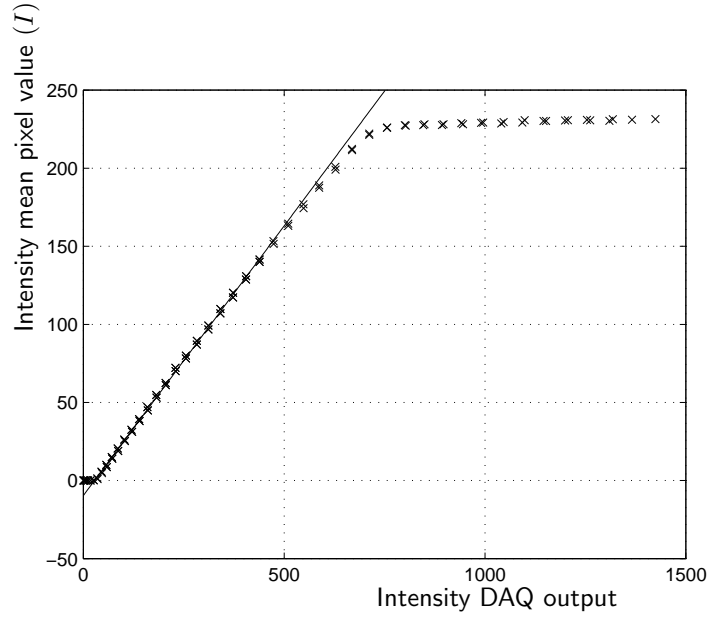


Figure 5.4: Intensity as measured by the camera (mean pixel value(I)) vs intensity measured by the power meter. A straight line fitted to data with $5 < I < 150$ is used to show the linear region.

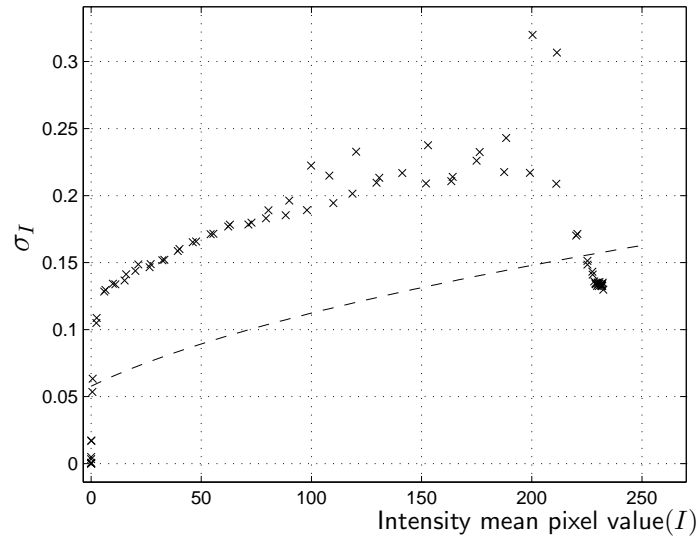


Figure 5.5: Mean noise in the camera's intensity measurement for the 5 x 5 pixel channels σ_I vs mean intensity (I). The dashed line shows the calculated result for an ideal camera with only shot noise and quantisation noise.

for all intensities below a threshold value. This is probably the result of the camera's dark current correction (black level) being too large. To show the non-linearity of the camera clearly, the intensity as measured by the camera is plotted against that from the power meter in figure 5.4. From the figure, it is clear that the camera's response is linear over the $5 < I < 150$ range used for finding ψ_m , for SPR imaging measurements as described in the previous chapter. The camera appears to be linear down to $I \sim 1$ and only slowly departs from linearity above $I = 150$. The $5 < I < 150$ range was used for the imaging measurements, as if the image is not uniform, some of the pixels in a 5×5 pixel channel may be outside the linear range even if the mean is not.

The noise of the intensity measurements was measured as the standard deviations of the 275 image sequences. The noise in the measurements from the photodiode showed no variation as the intensity changed and was 0.46 ± 0.04 DAQ output. The noise for the measurements from the camera was also calculated. The mean of the noise for all 800 channels is plotted against the mean intensity (mean I) in figure 5.5. The noise of the camera increases as the intensity increases and decreases as the camera saturates. The noise is significantly higher than the noise for an ideal camera with only shot noise and quantisation noise, showing the contribution of the camera's electronic noise. The shot noise is calculated assuming that the camera's full well capacity of 110,000 photoelectrons corresponds to its maximum intensity output $I = 255$. The quantisation noise is $1/\sqrt{12}$ of the least significant bit [77]. The noise is between 0.2 and 0.25 in the $100 < I < 150$ range that will dominate the fitted ψ_m , so the camera signal to noise ratio when calculating the system accuracy is approximately $C_{SNR} = 500$. Note that as a 5×5 pixel area is being averaged, the noise for a single pixel is approximately 1 or equal to the least significant bit. The noise from the photodiode sets an upper limit on the SLD intensity noise. As the noise is 0.46 ± 0.04 (DAQ output) independent of the intensity, so for the maximum measured intensity of 1400 (DAQ output), the intensity noise is no more than 1 part in 3000 and is thus insignificant for the camera measurements.

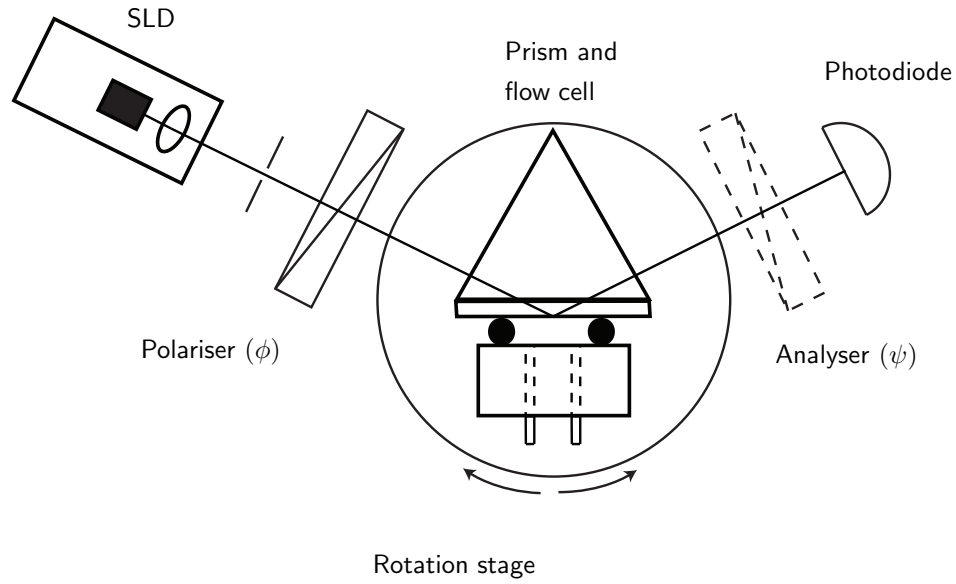


Figure 5.6: Apparatus for characterising the SPR slide. The analyser is removed for the reflectance measurements.

5.2 The SPR surface

The reflectivity for p-polarised light for a gold coated slide from the same batch as will be used for the imaging results was measured to observe the surface plasmon resonance. The slide was index matched to the prism and clamped to the flow cell as described in chapter 4.1.3. The flow cell was filled with distilled water. The beam from the SLD was passed through the Glan-Thompson polariser and then incident on the prism. The polariser was set to transmit p-polarised light. An iris limited the beam diameter to 2 mm. The beam reflected by the gold surface was detected by a Newport 1815-C power meter with its output connected to the data acquisition card. The beams reflected at the prism–slide interface were blocked so that they were not detected. The SPR prism was rotated to scan the angle of incidence using the SR50 rotation stage it was mounted on (as shown in figure 4.3) under

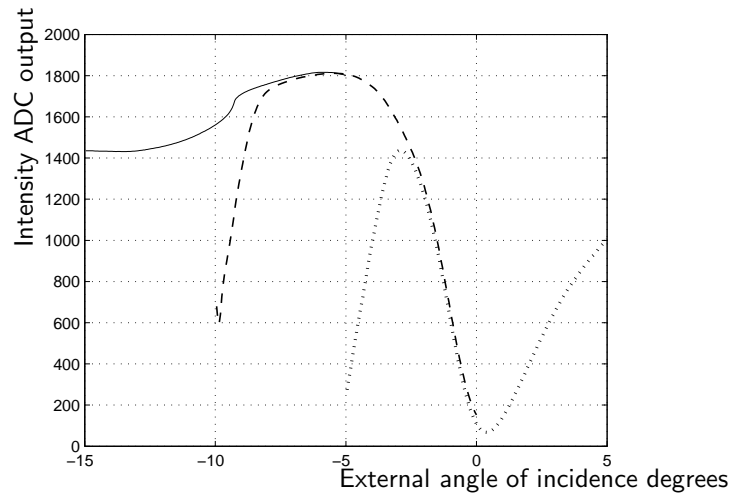


Figure 5.7: Intensity (result from the data acquisition cards ADC) vs external angle of incidence for 3 detector positions. The intensity decrease as the beam moves off the detector can be seen for two of the scans.

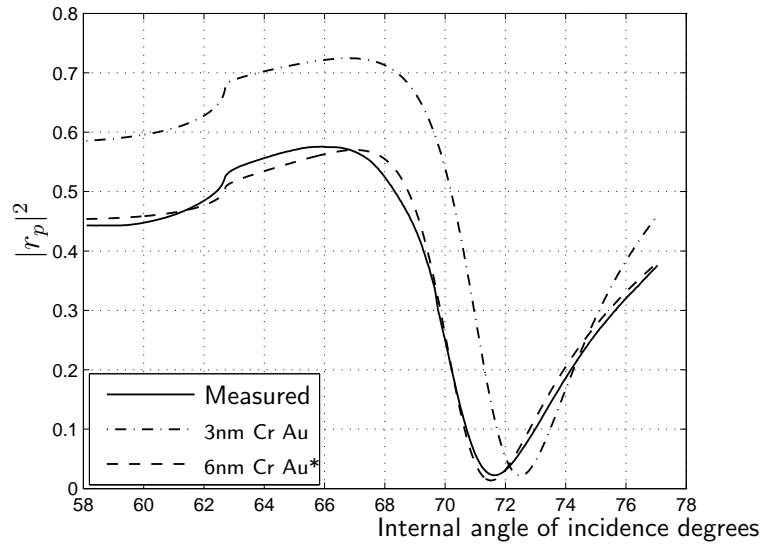


Figure 5.8: Reflectivity $|r_p|^2$ vs the angle of incidence. As well as the measured data two theoretical curves are shown one with 3 nm Cr and 45 nm Au as used for the theoretical calculations of chapter 3 and the other with 6 nm of Cr and the refractive index of gold $0.24 + 3.85i$ to better fit the experimental data.

the control of a Matlab program. The reflected intensity was recorded at 0.05° intervals. As the prism was rotated, the reflected beam moved across the detector so three scans with different positions of the power meter's photodiode were made to cover the desired angle of incidence range. The results for the three scans are shown in figure 5.7. The detected intensity is plotted against the external angle of incidence, that is the angle of incidence of the beam on the prism face. This is as opposed to the internal angle of incidence, the angle of incidence of the beam on the gold coated surface.

The internal angle of incidence was calculated by applying Snell's law to the air-prism and prism-slide interfaces. The intensity of the light incident on the prism was measured so that the reflectivity of the SPR surface could be calculated. The transmission of the air-prism and prism-slide interfaces was calculated using the Fresnel equations as described in section A. The refractive index of the index matching oil between the prism and slide is very close to that of the slide so this interface was treated as a direct transition from the prism to the slide. The measured reflectivity was corrected using the calculated transmissions to find the reflectivity for the gold SPR surface only. The result is shown in figure 5.8, plotted against the internal angle of incidence.

The surface plasmon resonance is observed as a steep dip in the reflectivity for p-polarised light. It was found that the measured resonance is significantly different than that expected from thin film modelling. Firstly, it had been found previously that the smallest minimum reflectivities were obtained for gold thicknesses of ~ 42 nm as measured by the film thickness monitor in the vacuum coater rather than 50 nm as expected from theoretical calculations. For the preparation of the batch of gold slides used, the gold was therefore evaporated to a thickness of 42 nm as measured by the thickness monitor. The minimum reflectance obtained is approximately 2 % which from modelling similar to that presented in chapter 3.5, is close to the minimum achievable for the source bandwidth. The resonance obtained is significantly wider than that predicted from thin film modelling and the maximum reflectivity is lower. This can be seen in figure 5.8 where the measured data can be compared to the theoretical curve for 3 nm Cr and 45 nm Au ($N = .161 + 3.64i$)[72]. A better fit to the experimental data can be obtained by increasing the thickness of the chromium layer to 6 nm to

reduce the maximum reflectivity and altering the refractive index of gold to $0.24 + 3.85i$. This is shown in the figure as the line labelled 6nm Cr Au*. It seems unlikely that the thickness of the chromium is twice the value given by the thickness monitor and other factors (index of Cr; roughness; contamination) are probably contributing. This new index value is mostly the result of increasing the imaginary part of the relative permittivity ($\sqrt{\epsilon_r} = N$) or the loss of the metal which makes the resonance dip wider. The original value of the relative permittivity was $\epsilon_r = -13.2 + 1.17i$ and the new value is $\epsilon_r = -14.7 + 1.87i$. The refractive index of vacuum deposited gold films is known to depend on the deposition conditions [72] so this index may be plausible as there is significant variation in the values given in the literature. Both the values for the imaginary part of the relative permittivity are within the range of values presented by Aspnes *et al.* [78] who reviewed the results for the properties of gold films prepared under different conditions. Also surface roughness is not modelled but this may increase the absorption of the plasmon which would widen the resonance dip in a similar way to changing the loss of the metal. The real part of the permittivity is also changed to move the angle of incidence at which the resonance occurs to match the experimental results more closely. More detailed modelling of the surface could be done but as this would need to model the effects of roughness, source bandwidth, uncertainty in the thickness and index of the chromium and gold it would be very complex and would need very accurate experimental data to be meaningful. Also, as will be shown in the imaging results presented in the next chapter, there is considerable variation across the surface of the gold slides and even more from one slide to another. The wider surface plasmon resonance dip is expected to reduce the sensitivity of the imaging instrument as r_p will change less rapidly with angle or refractive index.

5.2.1 Polarisation

The polarisation change of linearly polarised light reflected from the SPR slide was measured. The same apparatus as for the previous measurements was used except that the Glan-Thompson polariser in its rotation stage was moved to between the prism and detector to be used as an analyser and the polarising cube beam-splinter was used as the input polariser.

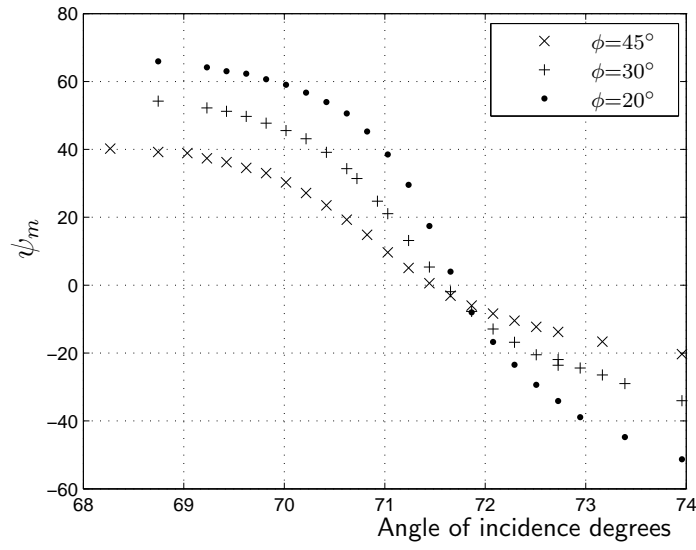


Figure 5.9: Analyser setting for minimum transmission (ψ_m) vs the internal angle of incidence. Three input polarisations are shown $\phi = 45^\circ$, 30° and 20° .

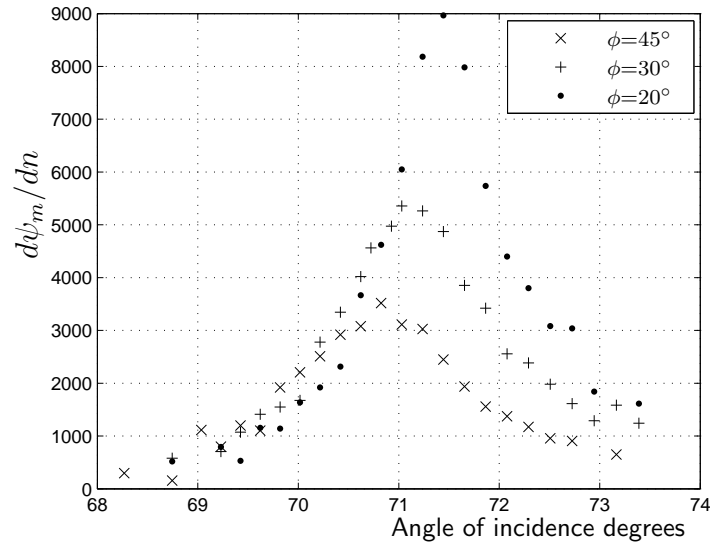


Figure 5.10: Sensitivity change in ψ_m per unit change refractive index vs angle of incidence.

As described in chapter 3.1, measuring the analyser setting for minimum transmission (ψ_m) for a fixed linear input polarisation (ϕ) reflected from a SPR sample is equivalent to finding the input linear polarisation for minimum intensity (ψ_m) with a fixed analyser at ϕ . A fixed input polarisation was used here as it was simpler experimentally, for these variable angle of incidence measurements.

For each polarisation measurement the analyser is scanned over a 200° range, with the transmitted intensity being recorded at 2° intervals. A sinusoid was then fitted to the intensity vs analyser azimuthal angle to find the setting for minimum intensity. The angle of incidence would then be changed and the analyser measurement repeated.

Figure 5.9 shows the result for the analyser setting for minimum transmission (ψ_m) vs the internal angle of incidence. Results are shown for three different input polarisations 45° , 30° and 20° from p-polarised.

The main effect of a change in the refractive index of the sensed medium is to shift the angle of incidence at which the resonance occurs, with increasing angle of incidence having a similar effect to decreasing refractive index. The 0.01 RIU change used for the simulations in chapter 3 is found to be equivalent to a 1.4° angle of incidence change. These results can thus be used to estimate the sensitivity for SPR measurements made with this sample. The sensitivity was calculated by using the difference between consecutive ψ_m measurements to estimate the gradient of the plots in figure 5.9 then multiplied by $1.4/0.01$. This is shown as change in analyser angle for minimum transmission per RIU $d\psi_m/dn$ plotted against the angle of incidence in figure 5.10.

Note that for the range of 70.6° to 72° angle of incidence, equivalent to a refractive index change of 0.01 RIU, the polarisation change is steep and approximately linear. As for the theoretical calculations in chapter 3.2, we see that as ϕ is moved closer to p-polarised, the sensitivity increases. The the maximum sensitivities are significantly less than those for the theoretical results (see figure 3.6). This is probably due to the reflectivity dip for this sample being wider than that for the system used for the theoretical calculations.

The sinusoidal fit to the intensity vs analyser angle data could also be

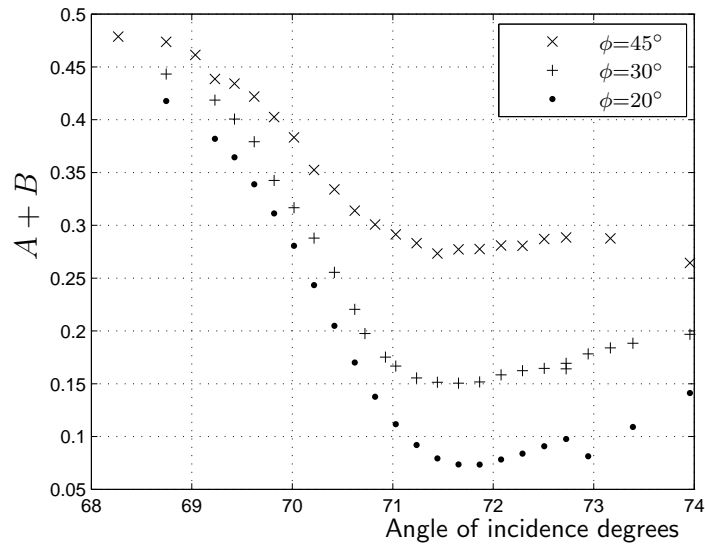


Figure 5.11: Maximum transmission $A + B$ vs angle of incidence.

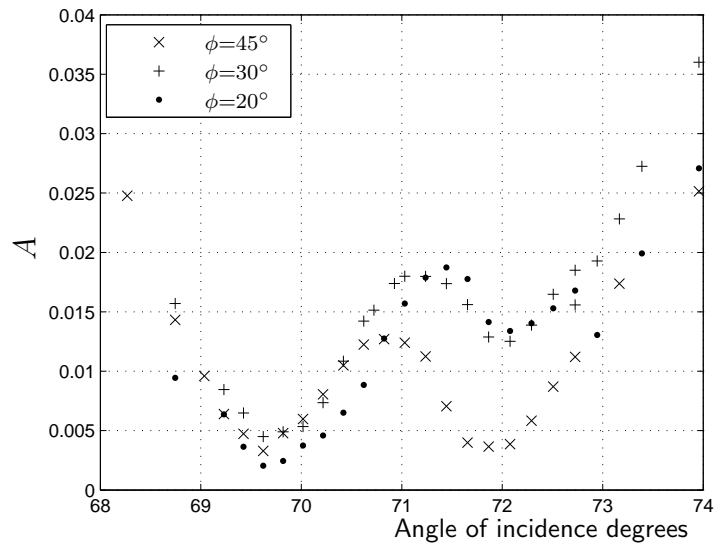


Figure 5.12: Minimum transmission A vs angle of incidence.

used to find the maximum and minimum transmission. The power of the beam incident on the prism and the loss of the analyser were not measured. The transmission for this sample, if the analyser was lossless, can be calculated from my results. The reflectance for p-polarised light is known from the results presented earlier in this section. This can be compared with the intensity recorded for the analyser scans when the analyser was set to transmit p-polarised light. The input power times the loss of the analyser can then be calculated. This was done using the results for 68.75° angle of incidence. Unlike the reflectivity measurements, these results and all the polarisation measurements are not corrected for the effect of the Fresnel reflection at the air–prism and prism–slide interfaces.

The maximum and minimum transmission for this system with a lossless analyser are shown in figures 5.11 and 5.12. Note that as for the theoretical results in chapter 3 (figures 3.8 and 3.9), the main effect of moving ϕ closer to 0° (p-polarised) to increase the sensitivity is to reduce the maximum transmission. As above, the range of 70.6° to 72° angle of incidence is equivalent to a refractive index change of 0.01 RIU as used for the theoretical calculations.

5.3 Expected sensor performance

The signal to noise ratios for refractive index measurements in the shot noise and camera saturation limit conditions $S/N_{shot}(n)|_{max}$ and $S/N_{sat}(n)|_{max}$ were calculated. These were calculated in the same way as for the theoretical treatment of chapter 3.3 (see equations 3.31, 3.36 and 3.37), using the sensitivity and transmission calculated from the polarisation measurements of the slide. The result for the signal to noise ratio of intensity measurements made with the camera measured in section 5.1, $C_{SNR} = 500$, is used when calculating the SNR for the camera saturation case. For the shot noise limit case, I_E , the input intensity measured as number of photons in the measurement time is needed (see equation 3.31). This was calculated for one channel assuming that the input power for the area of the beam that covers the camera’s sensor (0.6 mW) was spread equally over the 128×48 channels. The total energy in the measurement time (0.001 seconds) can then be calculated and a factor of 0.5 is included to account for a detector with

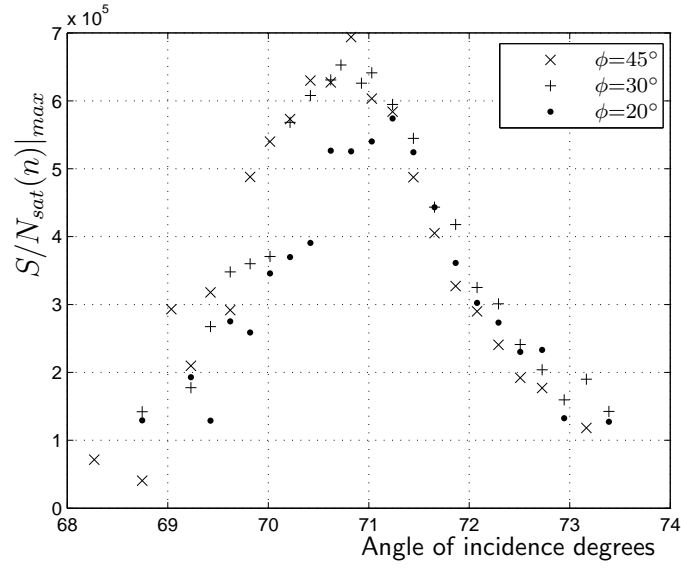


Figure 5.13: The signal to noise ratios for refractive index measurements in the shot noise limit $S/N_{sat}(n)|_{max}$ vs angle of incidence.

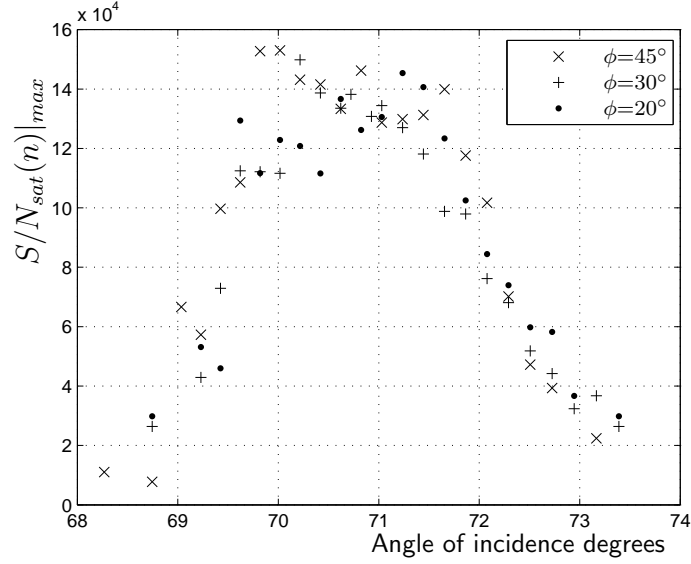


Figure 5.14: The signal to noise ratios for refractive index measurements in the camera saturation limit $S/N_{sat}(n)|_{max}$ vs angle of incidence.

a realistic quantum efficiency. The number of photons with that energy can then be calculated from the energy of each 680 nm photon (1.82 eV) and the charge on an electron to convert from electron volts (eV) to joules.

$$I_E = \frac{0.0006}{128 \times 48} \times 0.001 \times 0.5 \times \frac{1}{1.82 \times e} = 1.68 \times 10^8. \quad (5.1)$$

This gives $\sqrt{I_E} = 1.3 \times 10^4$ as used for the theoretical calculations of chapter 3.3.

The signal to noise ratios $S/N_{shot}(n)|_{max}$ and $S/N_{sat}(n)|_{max}$ are plotted in figures 5.13 and 5.14 respectively. Note that the SNR for the shot noise limit is much higher than that for the camera saturation limit so this instrument is being limited by the performance of the camera. For the camera saturation limit, the SNR is similar for all three settings of ϕ , so as for the theoretical results, it is expected that changing the analyser setting (ϕ) will not change the accuracy of refractive index measurements made with the imaging instrument. Over the range of 70.6° to 72° angle of incidence, (equivalent to a refractive index change of 0.01 RIU as above) $S/N_{sat}(n)|_{max}$ has a typical value of 1.3×10^5 . This is the maximum SNR for a single 1 ms exposure. When making measurements with the imaging instrument, as described in chapter 4.2.1, a sequence of 280 intensity measurements is made over a 1 second scan of the input polarisation ψ . When finding ψ_m for each channel, some of the intensity measurements are not used as the intensity is outside the linear range. For other intensity measurements, where the intensity and thus the intensity change per degree of ψ is small ¹, the signal to noise ratio for n will be much lower than its maximum ($S/N_{sat}(n)|_{max}$). For the purpose of estimating the accuracy of the imaging instrument, it is assumed that the accuracy will be the same as if one tenth as many measurements had been made all with the maximum signal to noise ratio $S/N_{sat}(n)|_{max}$. This is a fairly arbitrary value based on the fraction of the points in a typical scan that was presented in figure 4.4 that lie between $I = 75$ and $I = 150$ which are assumed to dominate the fitted ψ_m . For different scan ranges and different settings of the analyser, the fraction of the total number of measurements that would be appropriate to use would be different. This calculation is therefore intended to provide an order of magnitude estimate of the ex-

¹As the intensity vs ψ has a parabolic form near the minimum.

pected accuracy rather than a precise result. For this case, the SNR for the measurement of n will be increased by a factor of $\sqrt{28}$ over that for a single intensity measurement. So the noise in the refractive index measurements made with the imaging instrument will be approximately

$$\frac{1}{1.3 \times 10^5} \times \frac{1}{\sqrt{28}} = 1.5 \times 10^{-6} \text{RIU}. \quad (5.2)$$

In the next chapter, measurements made with the polarisation imaging instrument will be presented and the noise compared with this result.

6 Imaging measurements

This chapter presents measurements made with the polarisation imaging instrument described in the previous three chapters. In section 6.1 the response of the sensor to salt solutions with different refractive indices is presented. From these measurements, the sensitivity and noise for different settings of the output polariser, ϕ , are calculated and compared with the expected results of chapter 5. Measurements of a spatially varying refractive index change were also made using SPR slides partially coated with a fluoropolymer and are presented in section 6.2.

To determine the performance of the SPR polarisation imaging system, sample solutions of known refractive index were needed. For the results presented in this chapter, solutions were prepared by mixing salt (sodium chloride Ajax Finechem 99.9% pure) with distilled water, the salt and the mixed solution being weighed with a precision balance to calculate the concentration. The refractive index of these solutions was found by linear fitting to data from the CRC handbook [79]. Figures 6.1 and 6.2 show the data used to calculate the refractive indices of the solutions used for the refractive index measurements of section 6.1 and the measurements of the patterned slide presented in section 6.2, respectively. The gradient of the linear fits, $(dn/d(\%w/w)) = 0.001756$ for figure 6.1 and $(dn/d(\%w/w)) = 0.001827$ for figure 6.2, are used to calculate the difference in refractive index between the salt solutions and pure water (Δn). Note that this data is for $\lambda = 589$ nm and a temperature of 20° C. For my measurements, only the difference in refractive index for the solutions used is needed and the wavelength dependence of this is ignored. Solutions were stirred until all visible salt crystals had dissolved and left in covered containers on the optical table for at least 24 hours to ensure that the salt was completely dissolved and the solution

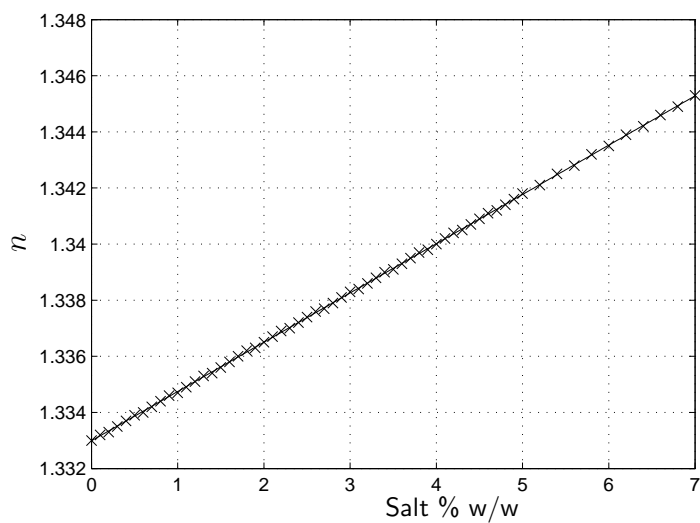


Figure 6.1: Refractive index of salt (NaCl) solutions vs concentration with least mean squares linear fit. This is the data from the CRC handbook [79] used for the refractive index measurements (section 6.1).

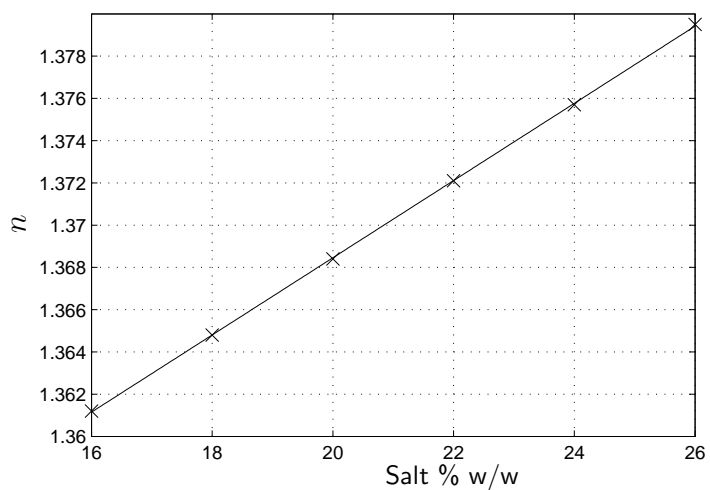


Figure 6.2: Refractive index of salt (NaCl) solutions vs concentration with least mean squares linear fit. This is the data from the CRC handbook [79] used for the measurements of the patterned slide (section 6.2).

was at ambient temperature.

6.1 Refractive index measurements

Refractive index measurements were made using the SPR polarisation imaging system. The gold coated microscope slide used was from the same batch as that measured in chapter 5.2. The six sample solutions shown in table 6.1 were prepared and the refractive index difference between them and pure water (Δn) calculated, as described above. The prism was rotated to an

Solution	NaCl % w/w	Δn
(1)	1.00	0.00176
(2)	2.00	0.0035
(3)	3.02	0.00524
(4)	4.04	0.00706
(5)	5.01	0.00876
(6)	6.03	0.0106

Table 6.1: The six salt solutions used.

external angle of incidence of -0.25° . The internal angle of incidence was calculated by applying Snell's law to the air-prism and prism-slide interfaces and was 71° . The temperature of the flow cell was stabilised at 18° C. This temperature was selected as being close to ambient, due to the limited performance of the temperature controller. The aperture in the imaging optics was set to a 1.5 mm diameter to increase the depth of field. This was done as it was difficult to accurately focus the system when using a sample with no obvious features. With this aperture setting, the resolution¹ and depth of field were $R = 1.22\lambda f/a = 110 \mu\text{m}$ and $\text{dof} = Rf/a = 48 \text{ mm}$.

Measurements made with the output polariser set to $\phi = 45^\circ$ will be presented in detail first and then those for $\phi = 30^\circ$ and $\phi = 20^\circ$ will be summarised and compared.

¹Rayleigh criterion.

6.1.1 Results for $\phi = 45^\circ$

Measurements made with the output polariser set to $\phi = 45^\circ$ will be presented first. For these measurements, the input polariser was set to centre the polarisation scan on $\psi = 10^\circ$. The input polarisation scan was approximately $\pm 30^\circ$. This scan range was chosen so that, for the refractive indices of all the solutions used and for all channels², intensity measurements were made for $\sim 10^\circ$ either side of ψ_m . This was done as it was found that the quadratic fit to find the input polarisation for minimum transmission, ψ_m , gave poor results if measurements on both sides of the minimum were not included. With the flow cell filled with distilled water, polarisation imaging measurements were started.

Measurements were made over an 80 minute period with the apparatus first being allowed to stabilise. The six solutions were then added to the flow cell, alternating with water. As described in chapter 4.2, to make each polarisation imaging measurement, the current through the modulator is changed to scan the input polarisation ψ . As the input polarisation is scanned, intensity measurements are made with the camera and the voltage across the modulator's current measuring resistor is recorded with the DAQ. The value of the resistor voltage at which the intensity is a minimum (V_m) is then found by a quadratic fit for each channel (group of 5×5 pixels). Figure 6.3 shows the raw V_m result for a single channel from the centre of the image. In the first 5 minutes of the measurement, V_m can be seen to change as the modulator and the current measuring resistor warm up. Between 30 and 70 minutes the flow cell is filled with each of the six salt solutions in turn, alternating with water. At the end of the experiment, a calibration measurement, as described in chapter 4.2.2, is made by rotating the input polariser by 10° in 1° steps. The average V_m change, for the 128×48 channels, as the polariser moved 10° was calculated and used to convert the V_m results to the input polarisation azimuthal angle for minimum transmission ψ_m . A total of 2000 ψ_m images were made over the 78.8 minute total time giving a 2.36 second average measurement time.

The input polarisation for minimum transmission, ψ_m , for a single 5×5 pixel channel from the centre of the image is shown in figure 6.4. The first

²There was variation in the results for different channels due to irregularity of the sensor surface as will be shown in figure 6.5.

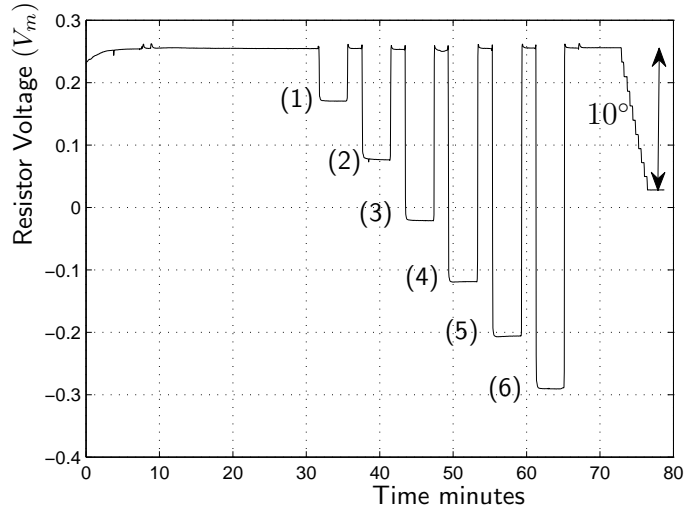


Figure 6.3: The fitted modulator current measuring resistor voltage for minimum transmission (V_m) for a channel from the centre of the image. The arrow marks the 10° input polariser change for calibration. The points where the different salt solutions were added are labelled.

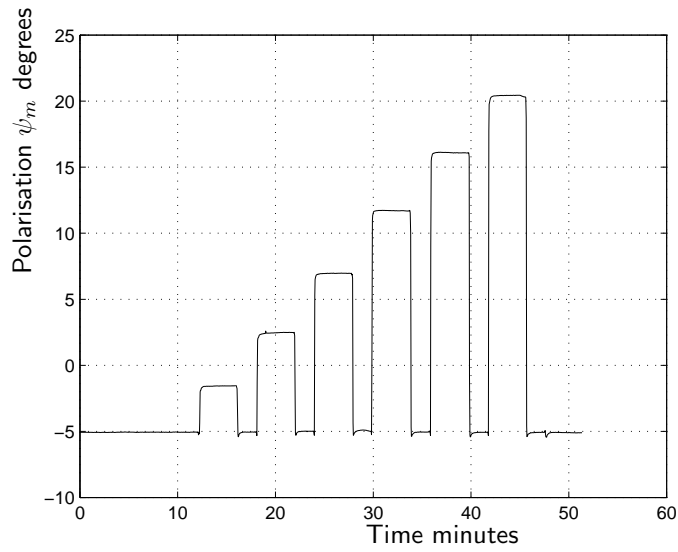


Figure 6.4: Input polarisation for minimum transmission (ψ_m) for a channel from the centre of the image.

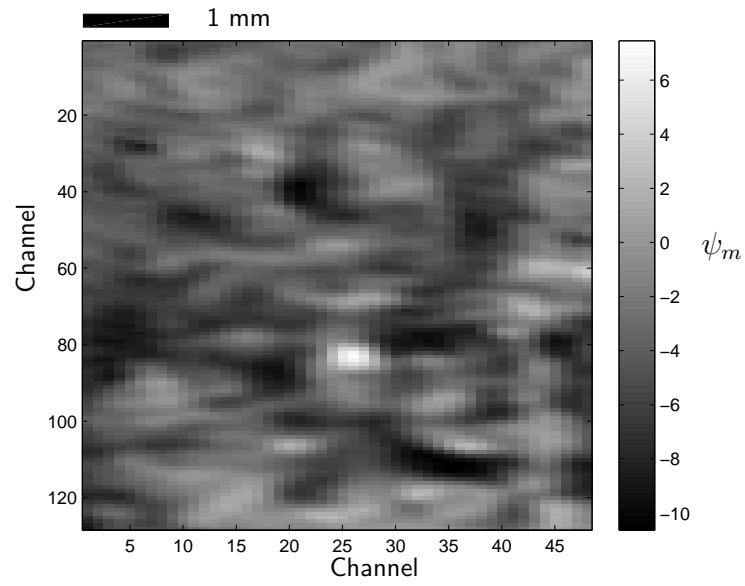


Figure 6.5: An image of the input polarisation for minimum transmission (ψ_m) with distilled water in the flow cell, $\phi = 45^\circ$.

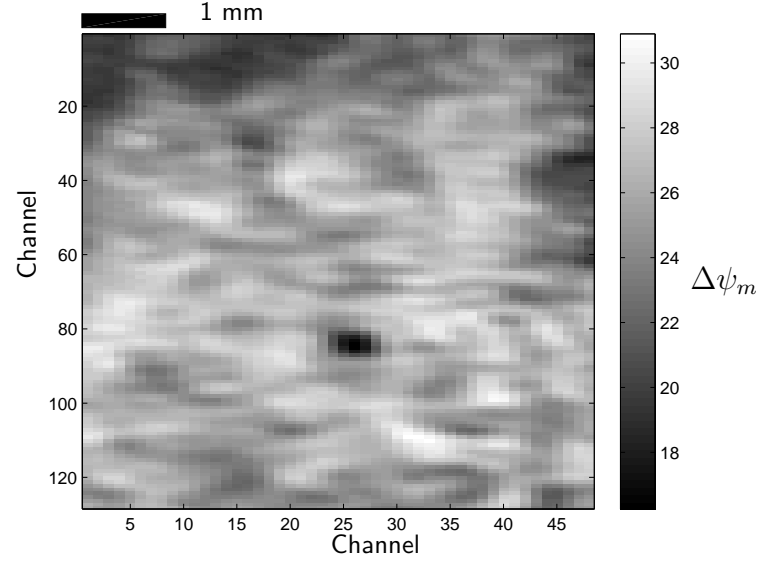


Figure 6.6: An image of the difference in the input polarisation ($\Delta\psi_m$) between solution (6) and water, $\phi = 45^\circ$.

20 minutes while the experiment was stabilising, and the calibration, are not shown. For the first 10 minutes shown, the flow cell is filled with water and ψ_m is constant as the refractive index is not changing. After 10 minutes the six salt solutions are added, alternating with water. In the graph this can be seen as steps in ψ_m as the refractive index changes. Distilled water is added between the salt solutions and it can be seen that ψ_m returns to its original value. The return of ψ_m to its original value confirms that the flow cell has been completely flushed of the salt solution. The size of the ψ_m steps increase, as the solutions were added in order of increasing refractive index. As the solutions are changed, spikes in ψ_m are seen due to temperature changes. This happens as the new solution is at ambient temperature and it takes the temperature controller some time to return the flow cell to its stabilised temperature.

Similar results to those shown in figure 6.4 are obtained for the other channels of the 128×48 channel image. Figure 6.5 shows a typical ψ_m image made with distilled water in the flow cell. The variation in ψ_m is believed to be due to variations in the gold coated surface.

The sensitivity of the instrument was calculated from the difference in ψ_m for distilled water and solution (6). The average ψ_m over two 1 minute periods (water and solution (6)) were used to calculate the sensitivity for each channel. The mean ψ_m change was $\Delta\psi_m = 25.3^\circ \pm 2.3^\circ$. The error here and throughout these results is used to show the variation (1 standard deviation) between different channels. From this and the refractive index difference between solution (6) and water, $\Delta n = 0.0106$, the mean sensitivity was calculated to be $d\psi_m/dn = 2390 \pm 220^\circ \text{RIU}^{-1}$.

It is clear from this that the sensitivity varies considerably for different channels across the gold surface. An image of the difference in the input polarisation for minimum intensity between solution (6) and water, $\Delta\psi_m$, is shown in figure 6.6. This image can be compared with figure 6.5, an image of ψ_m with distilled water in the flow cell.

The noise in the ψ_m results were calculated from the standard deviation of the results over 1 minute intervals. This was done for the first 10 minutes as shown in figure 6.4 and the mean for each channel found. The mean of these polarisation noise results for all channels was then $\sigma_{\psi_m} = 0.0046^\circ \pm 0.0021^\circ$. From the the sensitivity of ψ_m to refractive index changes, the noise in ψ_m can

be converted to the noise in the measured refractive index. The refractive index noise is thus $1.94 \pm 1.1 \times 10^{-6}$ RIU. The error shown in this result ($\pm 1.1 \times 10^{-6}$ RIU) is the variation between channels as for all measurements presented in this chapter. If instead the variation in the noise over the 10 minute interval is used, the error is $\pm 0.15 \times 10^{-6}$ RIU showing that the noise for each channel is almost constant. The noise is similar when the different solutions are in the flow cell.

As well as the noise in the refractive index measurement, the long term drift was analysed. The drift was calculated by finding the difference in the average of ψ_m for two 1 minute intervals and then using the sensitivity to convert it to refractive index. The drift for the first 10 minutes of the data shown in figure 6.4 was $8.7 \pm 2.6 \times 10^{-6}$ RIU. The drift over the whole 50 minutes of the experiment was $11 \pm 18 \times 10^{-6}$ RIU.

Averaging over several channels should reduce the noise in the refractive index due to the camera's intensity noise. To test this, ψ_m for 6×2 groups of channels were averaged. This gave a 21×24 channel image with each channel being an approximately square area on the gold surface. The refractive index noise was then $1.27 \pm 0.58 \times 10^{-6}$ RIU. This is a decrease, but it is not as large as the factor of $\sqrt{12}$ expected if the noise was uncorrelated. The average ψ_m for an 18×6 group of channels from the centre of the image was subtracted from the other 6×2 channel groups in an attempt to reduce the effect of any noise that was correlated across the whole image. This had little effect, resulting in a noise of $1.14 \pm 0.52 \times 10^{-6}$ RIU. Averaging over a 60×20 group of channels from the centre of the image reduced the noise to 0.83×10^{-6} RIU.

6.1.2 Results for all analyser settings

Refractive index measurements were also made for other settings of the analyser, ϕ . These results will now be summarised, with the results for $\phi = 45^\circ$ shown above, repeated for comparison. The ψ_m from 1 channel in the centre of the image for $\phi = 30^\circ$ is shown in figure 6.7 and for $\phi = 20^\circ$ in figure 6.8 whereas those for $\phi = 45^\circ$ were shown in figure 6.4. For $\phi = 30^\circ$, the input polarisation (ψ) scan was centred on $\psi = 10^\circ$ as above. The input polarisation scan was increased to its maximum of approximately $\pm 40^\circ$ due to the

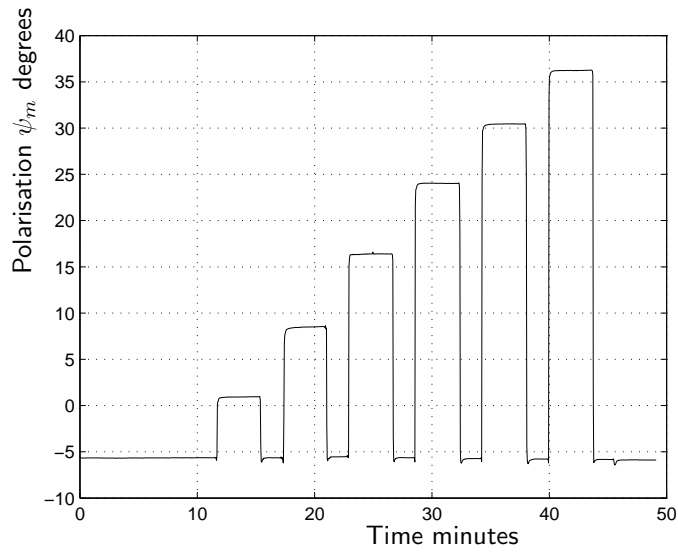


Figure 6.7: Input polarisation for minimum transmission (ψ_m) for a channel from the centre of the image with the analyser set at 30° . The six salt solutions were added in order of increasing index, alternating with water.

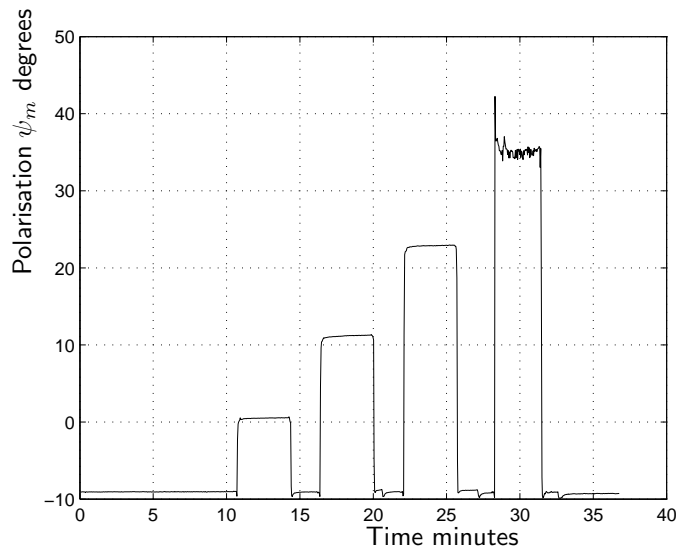


Figure 6.8: Input polarisation for minimum transmission (ψ_m) for a channel from the centre of the image with the analyser set at 20° . Salt solutions (1) to (4) were added alternating with water.

higher sensitivity for $\phi = 30^\circ$. For $\phi = 20^\circ$ the input polarisation (ψ) scan was also approximately $\pm 40^\circ$ but centred on $\psi = 2^\circ$. The centre position had to be moved due to the high sensitivity with $\phi = 20^\circ$. In addition, because of variations in the gold surface, some channels were at the edge of the scan with distilled water in the flow cell and a $\psi = 10^\circ$ centred scan. Solutions (5) and (6) were not used for $\phi = 20^\circ$ as the high sensitivity meant that these were not within the scan range. For solution (4) with $\phi = 20^\circ$, ψ_m was at the edge of the input polarisation (ψ) scan for many channels and gave poor results as shown by the increased noise in figure 6.8. Data for solution (4) were therefore not used for analysis of the sensor performance with $\phi = 20^\circ$.

The sensitivity was calculated in the same way as for $\phi = 45^\circ$. For $\phi = 30^\circ$ the mean input polarisation difference, $\Delta\psi_m$, for distilled water and solution (6) was $41.5^\circ \pm 4.3^\circ$. For $\phi = 20^\circ$ the difference between distilled water and solution (3) was used and was $30.9^\circ \pm 2.5^\circ$. It was found that some channels, where ψ_m was near the edge of the input polarisation (ψ) scan, gave poor or no results. For $\phi = 30^\circ$, channels where the polarisation difference (water to solution (6) as above) was greater than 55° were excluded from the analysis. A total of 61 out of the $128 \times 48 = 6144$ channels were excluded. For $\phi = 20^\circ$, a cut-off of 36° difference (water to solution (3)) was used, excluding 785 out of 6144 channels. A high sensitivity was used to exclude data as it was found that when a channel's ψ_m neared the edge of the ψ scan, the fitted value of ψ_m became too large. The calculated sensitivities are shown in the following table.

Analyser	$\phi = 45^\circ$	$\phi = 30^\circ$	$\phi = 20^\circ$
Sensitivity $d\psi_m/dn$ °RIU ⁻¹	2390 ± 220	3910 ± 410	5890 ± 470

Table 6.2: Sensitivity of ψ_m to refractive index changes.

The sensor response for all three analyser settings is shown in figure 6.9. The difference between ψ_m for each of the solutions and water, $\Delta\psi_m$, is calculated for all channels and then averaged. In the graph, $\Delta\psi_m$ is plotted against the refractive index difference between the solutions and water.

As expected from the measurements of a gold coated slide from the same batch presented in chapter 5.2.1 and from the theoretical calculations of chapter 3.2, as the transmission axis of the analyser is moved closer to p-polarised

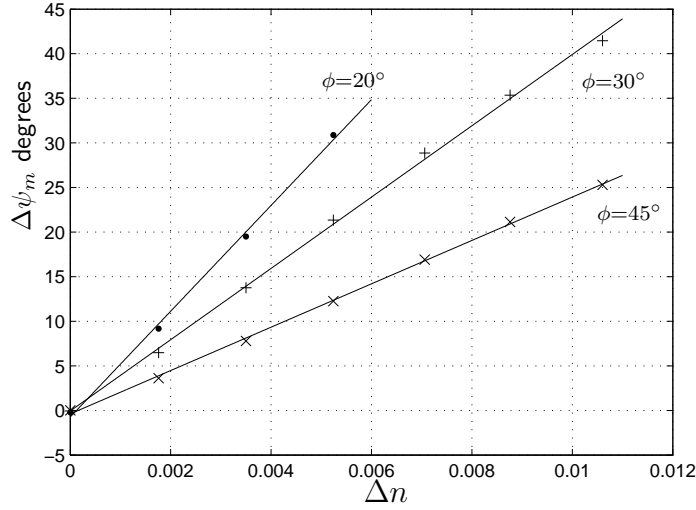


Figure 6.9: The mean change in the input polarisation for minimum transmission ($\Delta\psi_m$) for different solutions with refractive indexes $n = 1.33 + \Delta n$ for three settings of the analyser (ϕ).

($\phi = 0^\circ$) the sensitivity increases. However, the sensitivities obtained are significantly less than those measured in chapter 5.2.1 for a gold slide from the same batch. As shown in figure 5.10, the mean sensitivities over a 0.01 RIU range (1.4° angle of incidence range) were approximately $3000^\circ\text{RIU}^{-1}$ for $\phi = 45^\circ$ and $4500^\circ\text{RIU}^{-1}$ for $\phi = 30^\circ$. This will be discussed further at the end of this chapter.

The noise was calculated for $\phi = 30^\circ$ and $\phi = 20^\circ$ as described above for $\phi = 45^\circ$ and are shown in the table below. The noise for $\phi = 45^\circ$ is repeated for comparison. It is clear that as ϕ is moved closer to zero to

Analyser	$\phi = 45^\circ$	$\phi = 30^\circ$	$\phi = 20^\circ$
Noise in ψ_m	$0.0046^\circ \pm 0.0021^\circ$	$0.0085^\circ \pm 0.0034^\circ$	$0.012^\circ \pm 0.007^\circ$
Noise in n , RIU	$1.94 \pm 1.1 \times 10^{-6}$	$2.1 \pm 0.68 \times 10^{-6}$	$2.1 \pm 1.2 \times 10^{-6}$

Table 6.3: Noise in the polarisation and refractive index.

increase the sensitivity, the noise in the polarisation measurement increases such that there is no gain in the accuracy of the refractive index measurement.

This is in agreement with the theoretical modelling of chapter 3.3.2 and the calculations using the measured properties of a gold slide from chapter 5.3. The noise in the refractive index are close to the expected value calculated in chapter 5.3 (1.5×10^{-6} RIU) .

6.2 Patterned Slides

Measurements were made using gold coated slides patterned with a fluoropolymer to demonstrate that a spatially varying refractive index change can be imaged.

To pattern the slide, FluoroPel 802A solution from Cytonix³ was used. This is a 2% solution of a fluoro-acrylate polymer in a perfluoro-alkane solvent. The solvent was allowed to evaporate until the volume of the solution had reduced to 1/5 of the original volume before it was applied to the surface. This was done to increase the viscosity of the solution. Drops of the resulting solution were placed on the gold surface of the microscope slides with a syringe. The slides were then dried in an oven at 80°C for 15 minutes and allowed to cool. This left a film with refractive index $n \sim 1.37$ on circular areas of the slide surface. The film was thicker at the edges than the centre and if it was not dried in the oven, the refractive index at the edges was significantly (> 0.01) greater than at the centre, probably due to the solvent not completely evaporating. However, as will be shown in my results, the baking significantly damaged the gold surface. The refractive index of the areas of the gold surface covered by the fluoropolymer will stay constant. So if different salt solutions are flowed over the slide, the refractive index and thus the measured ψ_m of only the uncoated areas will change.

A 22.0% w/w salt solution with an approximately 1.37 refractive index was prepared by dissolving 66.03 g NaCl in distilled water to give a total of 300.01 g of solution. A second 21.7% w/w NaCl solution was prepared by adding 146.72 g of the first solution to 2.21 g of distilled water. Using the data from the CRC handbook [79], shown in figure 6.2, the refractive index of these two solutions was calculated to differ by 0.0006 RIU.

The aperture in the imaging optics was set to 3.5 mm diameter for the

³www.cytonix.com

measurements with patterned slides. With this aperture setting, the resolution and depth of field were $R = 47 \mu\text{m}$ and $\text{dof} = 8.9 \text{ mm}$, respectively. So the resolution of the imaging optics is almost the same as the size of the 5×5 pixel channels used.

An image of a patterned slide is shown in figure 6.10. This image is a single intensity measurement made with the polarisation imaging apparatus and the input polarisation set to p-polarised. The flow cell is filled with air and the angle of incidence is adjusted to the SPR reflectivity minimum for the parts of the slide coated with the fluoropolymer or approximately 77° angle of incidence. The light reflected from the area of the gold surface in contact with air does not couple to a surface plasmon and the reflectivity is high. The exposure time was therefore reduced to 0.1 ms to avoid saturating the camera. In the image, the circular areas coated in the fluoropolymer can clearly be seen as dark, low reflectivity areas. For this image, the pixels were not averaged to 5×5 pixel channels. The variation in intensity of the uncoated area is due to the non-uniformity of both the gold surface and the input beam.

6.2.1 Results for patterned sample 1

The temperature of the flow cell was stabilised at 19°C . Measurements were made for all three analyser settings, $\phi = 45^\circ, 30^\circ, 20^\circ$. For these measurements, the input polariser was set to centre the polarisation scan on $\psi = 10^\circ$. An input polarisation (ψ) scan of approximately $\pm 20^\circ$, $\pm 30^\circ$ and $\pm 40^\circ$ was used for the $\phi = 45^\circ, 30^\circ, 20^\circ$ measurements, respectively.

Polarisation imaging measurements were then made. During these measurements, the 21.7% and 22.0% NaCl solutions were exchanged in the flow cell. Figure 6.11 shows a typical image made with $\phi = 45^\circ$ and the 21.7% NaCl solution in the flow cell. It can be seen in the image that the uncoated areas of the gold surface are less uniform. This is believed to be due to damage to the sample from the baking process.

The response of two typical 5×5 pixel channels from areas of the slide coated and uncoated with the fluoropolymer is shown in figure 6.12. For this particular measurement, the analyser was set to $\phi = 45^\circ$ and initially the 21.7% NaCl solution is in the flow cell. The channel from the coated area

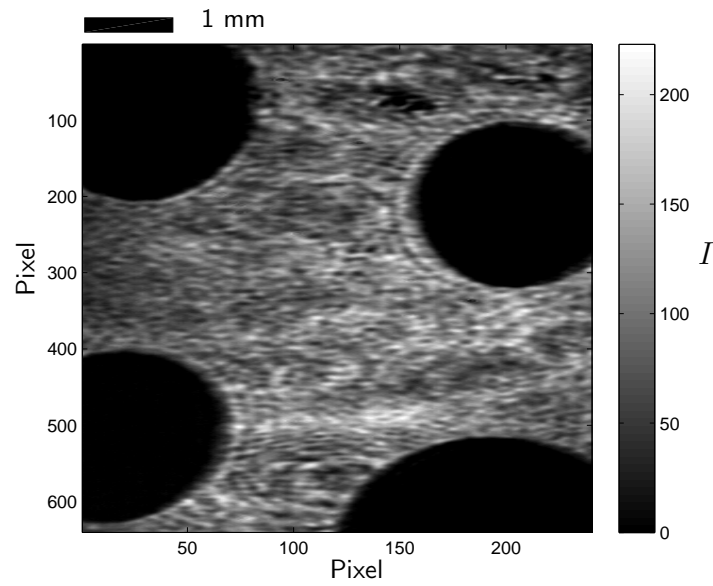


Figure 6.10: Reflected intensity, I , for a microscope slide coated with drops of fluoropolymer with p-polarised input light and the flow cell filled with air.

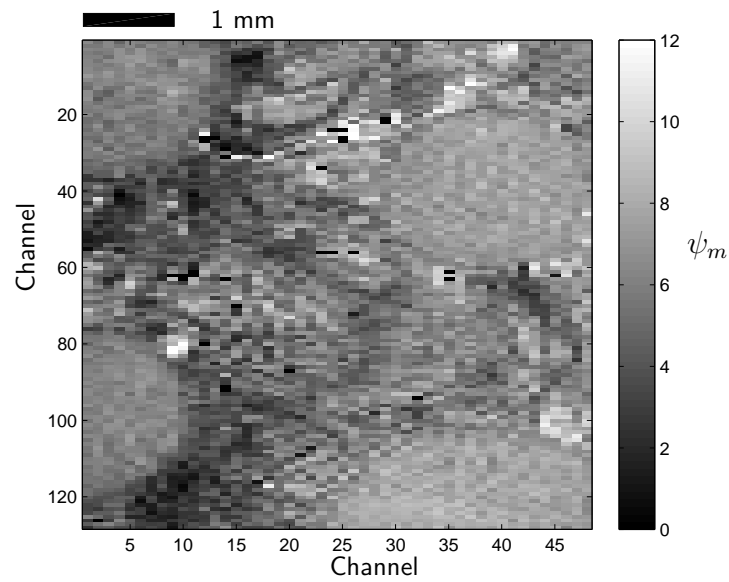


Figure 6.11: Input polarisation for minimum transmission, ψ_m , image of the same partially coated slide as the above figure. Analyser setting $\phi = 45^\circ$ and the 21.7% NaCl solution in the flow cell.

shows almost no change when the solutions are changed apart from the spikes due to temperature changes. This is because the refractive index for that channel stays constant at the index of the polymer ($n \sim 1.37$) independent of what is in the flow cell. For the uncoated channel, ψ_m changes when a solution with a different refractive index is added to the flow cell in the same way as for the refractive index measurements presented earlier in this chapter. The difference ($\Delta\psi_m$) between two polarisation images made with the two different salt solutions is shown in figure 6.13. For the coated areas $\Delta\psi_m \approx 0^\circ$, while for the uncoated areas the change in ψ_m due to the refractive index change can be seen. Two rectangular areas are marked on the image and these areas were used for the sensitivity and noise calculations that follow. The larger rectangle is the uncoated area and the other one, the coated area. Similar results were obtained for the other two analyser settings of $\phi = 30^\circ$ and $\phi = 20^\circ$.

The sensitivity $d\psi_m/dn$ was calculated for the uncoated rectangular area marked on figure 6.13 from the change in ψ_m for the known refractive index change of 0.0006 RIU, $\Delta\psi_m$. The noise in the measured ψ_m was calculated for the uncoated and coated areas marked on the figure from the mean, for the first 5 minutes, of the standard deviation for one minute periods. The noise in the refractive index measurement was then calculated from the sensitivity and the noise in the polarisation measurement. This was done for all three analyser settings $\phi = 45^\circ, 30^\circ, 20^\circ$. A summary is shown in the table below where (U) means uncoated and (C) coated. As previously, uncertainties shown are one standard deviation variation between channels.

Analyser	$\phi = 45^\circ$	$\phi = 30^\circ$	$\phi = 20^\circ$
$\Delta\psi_m$	$2.39^\circ \pm 0.18^\circ$	$3.72^\circ \pm 0.25^\circ$	$5.72^\circ \pm 0.41^\circ$
$d\psi_m/dn$ °RIU ⁻¹	3990 ± 290	6200 ± 410	9540 ± 680
Noise, ψ_m (U)	$0.0051^\circ \pm 0.0024^\circ$	$0.0072^\circ \pm 0.0035^\circ$	$0.0135^\circ \pm 0.0064^\circ$
Noise, n (U)	$1.29 \pm 0.68 \times 10^{-6}$	$1.18 \pm 0.62 \times 10^{-6}$	$1.46 \pm 0.77 \times 10^{-6}$
Noise, ψ_m (C)	$0.0038^\circ \pm 0.0010^\circ$	$0.0050^\circ \pm 0.0014^\circ$	$0.0094^\circ \pm 0.0027^\circ$
Noise, n (C)	$0.95 \pm 0.26 \times 10^{-6}$	$0.80 \pm 0.22 \times 10^{-6}$	$0.98 \pm 0.28 \times 10^{-6}$

Table 6.4: Sensitivity and noise for the patterned slide.

The sensitivity ($d\psi_m/dn$) was found to be higher for these imaging mea-

surements than for the measurements made with the six salt solutions. Part of this is due to the fact that a small refractive index change is being measured at the angle of incidence for peak sensitivity rather than measuring the average sensitivity for a larger (0.0106 RIU as before) range. Most of the sensitivity difference is probably due to differences between the gold surfaces for the two sets of measurements. The sensitivities obtained are quite close to those obtained for the thin film modelling of chapter 3.2 which were 3670, 6570, 10850 $^{\circ}\text{RIU}^{-1}$ for analyser settings of 45° , 30° , 20° respectively (see figure 3.6 at $\Delta n = 0.0055$ or peak sensitivity for the analyser at 45°). The sensitivities are higher than would be expected from the measurements made on a gold slide from the same batch presented in figure 5.10. From thin film modelling, it is expected that the sensitivity should not change significantly between measurements with the refractive index $n \sim 1.33$ and $n \sim 1.37$ as long as the angle of incidence is adjusted accordingly. The noise in the refractive index measurement is lower than for the six salt solutions due to the increased sensitivity while there is little change in the noise in the polarisation measurement. The setting of the analyser has little effect on the accuracy with which refractive index changes can be determined and the noise is similar to the expected value of 1.5×10^{-6} RIU.

Second partially coated slide

Measurements were also made for a second partially coated slide. Different salt solutions to those used for the first partially coated slide were prepared but the concentrations and refractive index difference were approximately the same ($\Delta n = 0.0006$ RIU). This allows the repeatability of the instrument to be checked and ensures that the high sensitivity for the partially coated slide was not due to a mistake in preparing the salt solutions⁴. Only the results with the analyser set at $\phi = 45^{\circ}$ are shown here. Figure 6.14 shows the difference of two polarisation (ψ_m) images with the two solutions. The sensitivity and noise were calculated in the same way as for the previous sample. The polarisation change for the rectangular uncoated area shown in the figure was $\Delta\psi_m = 2.14^{\circ} \pm 0.35^{\circ}$ and the sensitivity thus $d\psi_m/dn = 3560 \pm 580$ $^{\circ}\text{RIU}^{-1}$. The noise in the refractive index measurement was

⁴If the salt had been weighed incorrectly or spilt the refractive index difference between the two solutions would be different and the calculated sensitivity would be wrong.

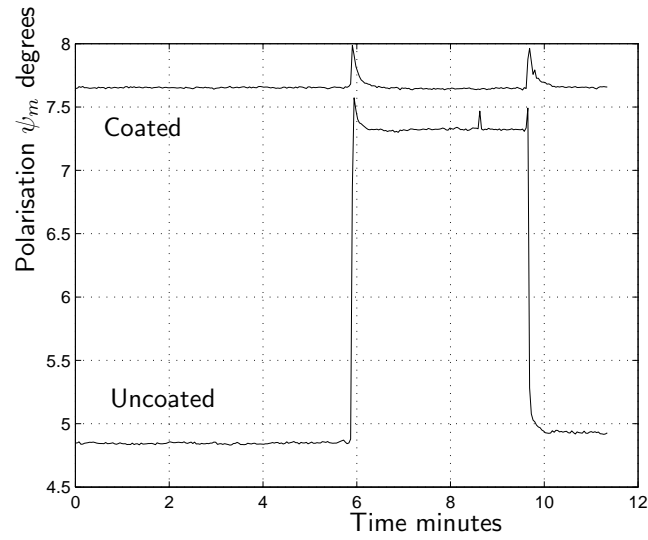


Figure 6.12: Input polarisation for minimum transmission, ψ_m , for two channels from an area coated and uncoated with the fluorepolymer. Analyser setting $\phi = 45^\circ$ and the 21.7% NaCl solution in the flow cell initially.

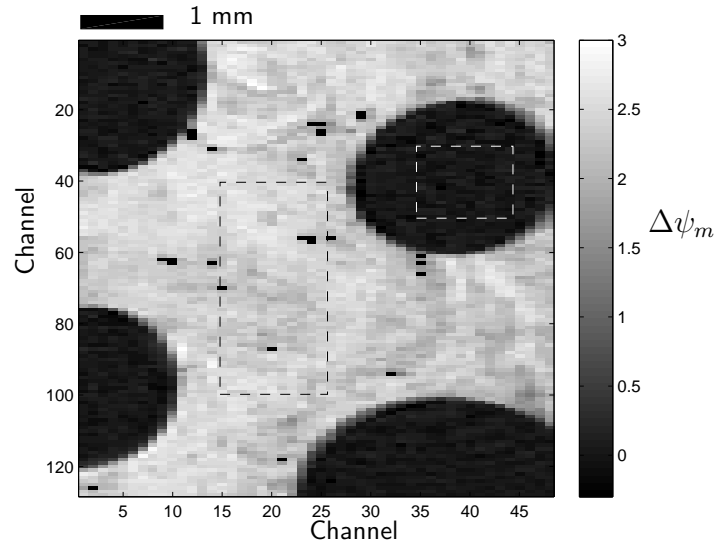


Figure 6.13: Input polarisation for minimum transmission difference, $\Delta\psi_m$, for two images made with two salt solutions (21.7% and 22.0% NaCl) refractive index difference 0.0006 RIU. Analyser setting $\phi = 45^\circ$. The dashed line rectangular areas are used for the noise calculations.

$1.5 \pm 1.2 \times 10^{-6}$ RIU for the uncoated area and $0.71 \pm 0.20 \times 10^{-6}$ RIU for the coated area.

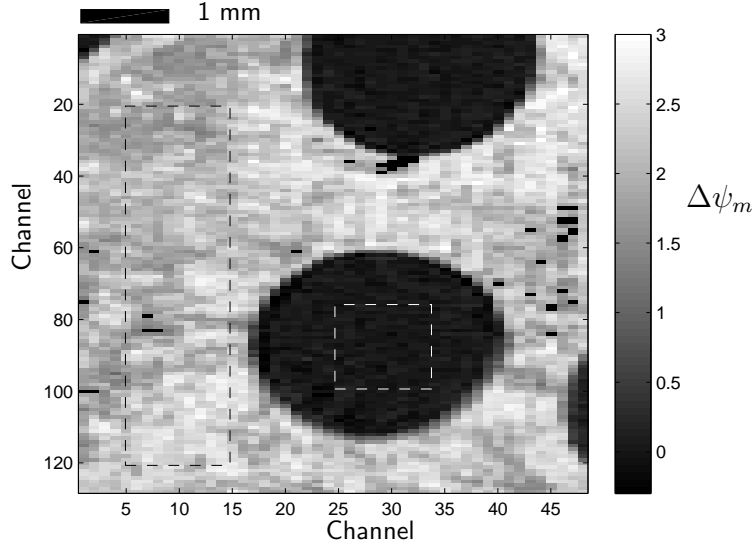


Figure 6.14: Imaging result for the second gold coated slide partially coated with the polymer. The image shows the input polarisation for minimum transmission difference, $\Delta\psi_m$, for images made with two salt solutions (21.7% and 22.0% NaCl) refractive index difference 0.0006 RIU. Analyser setting $\phi = 45^\circ$. The dashed line rectangular areas are used for the noise calculations.

6.3 Discussion and future work

Considerable variation in the sensitivity has been observed, both between different points on each gold slide and between the different gold slides used. This is believed to be due to variations in the properties of the gold surfaces but the exact cause is not clear. All of the gold coated microscope slides used for this chapter were coated at the same time in the vacuum coater. The slides to be coated were mounted around the top of the vacuum chamber. The distance from the gold source to the different slides was approximately the same. However the gold source, a small amount of gold wire melted in a tungsten boat, will emit most intensely upwards [80] so the thickness deposited will not be the same for all slides. It was difficult to adequately

clean the microscope slides and the deposited gold layer is sensitive to any contamination. Areas of the slides where the surface was visibly different, perhaps due to contamination and resulting roughness of the gold layer, were seen on many of the slides. The slides used for the experiments were selected as appearing mostly uniform but may have had some roughness. Surface roughness of the gold layer will couple the plasmon to light [9]. The increase in the loss due to the emitted light is expected to make the SPR dip wider in a similar way to increasing the intrinsic loss of the gold (see figure 5.8). A wider SPR dip will mean a smaller sensitivity. The baking may have altered the properties of the gold surfaces partially coated in the fluoropolymer. The exposed areas of the gold surfaces were noticeably more irregular than the areas covered in the polymer (see figure 6.11) and may have been contaminated. It is also known that if gold films deposited on glass with a chromium adhesion layer are heated the chromium may diffuse through grain boundaries to the surface and then oxidise [73].

The noise for the 5×5 pixel channels was close to the expected value of 1.5×10^{-6} RIU calculated from the properties of the gold surface and camera in chapter 5. It was found that little reduction in the noise could be obtained by averaging groups of channels. The cause of this noise limit is not clear. In the SPR literature, noise limits of the order of a few 10^{-7} RIU are often attributed to vibration or pressure fluctuations (for example see Hooper *et al.* [50]). Noise due to pressure changes would be expected to be well correlated across the surface, but this was not observed. The optical table was mounted on compressed air vibration isolators but no change in the noise was observed with these on. Some early measurements were made with the SPR prism replaced by a reflection from a gold coated prism with the light reflected from an air-gold interface (incident from the air rather than glass side, so no SPR). It was found that the noise in the polarisation measurement could easily be reduced to 0.001° by averaging groups of channels. So the observed noise limit is not believed to be due to limitations of the instrument but rather due to fluctuations at the SPR surface.

It was intended to experiment with commercial gold SPR surfaces to see if using surfaces with more consistent properties would reduce the variation in the sensitivity. A set of SPR surfaces was acquired but were not very uniform. The surfaces showed an irregular pattern of spots where the angle

of incidence for the resonance differed by $\sim 1^\circ$ making them unsuitable for my instrument. It would be desirable to investigate whether the use of more uniform gold surfaces gives more consistent results for the sensitivity of ψ_m to refractive index changes. The noise limit could also be investigated to see if it is affected by the surface properties.

Using a higher performance camera could allow the accuracy or number of channels to be increased. The Micron MT9V403 sensor used in the camera is considered obsolete by its manufacturer and has a resolution of 640×480 pixels at 200 frames per second (fps). A newer sensor, the MT9M413, is available with a resolution of 1280×1024 pixels at 500 fps. This sensor is used in the high accuracy angle scanned SPR imaging instrument demonstrated by VanWiggeren *et al.*[18].

The polarisation imaging sensor presented has a significantly improved accuracy than typical intensity imaging SPR systems that typically have a noise of $\sim 10^{-5}$ RIU [60]. The noise of $\sim 2 \times 10^{-6}$ RIU obtained is close to the polarisation contrast results of Homola *et al.* [61, 62] for 64 independent channels, but an image of 128×48 independent channels is obtained for my instrument. The noise obtained is however higher than the 2.6×10^{-8} RIU for 110 channels shown by VanWiggeren *et al.*[18] for their angle scanned SPR imaging instrument. The polarisation imaging instrument demonstrated here therefore has a good accuracy over a large number of channels using a simple optical system.

7 Differential SPR theory

When using a SPR sensor to detect binding reactions, drifts due to changes in the bulk refractive index or temperature can cause problems. A solution is to compare two sensors, only one of which is sensitised to the analyte of interest. As was described in chapter 2.3.2, instruments for measuring two areas of a SPR surface have been developed for this purpose. This chapter presents an instrument that measures the difference in refractive index between two SPR surfaces. This sensor uses a novel optical configuration where a beam is reflected from two areas of a SPR surface and the transmission is proportional to the square of the difference of the reflection coefficients for the two areas.

7.1 Concept

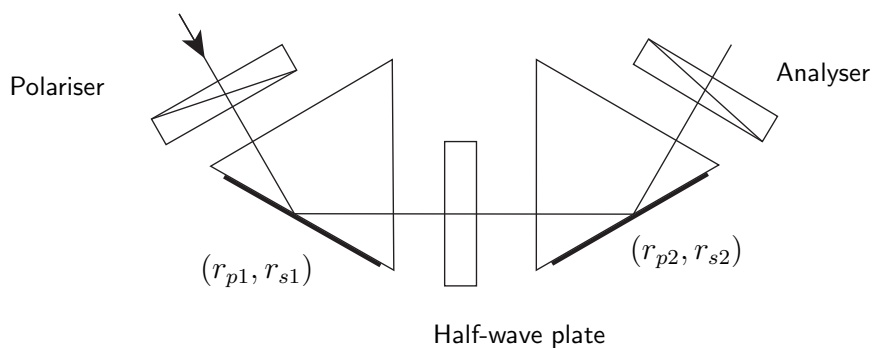


Figure 7.1: A two prism SPR system.

Figure 7.1 shows the concept of a differential surface plasmon resonance sensor. A beam of polarised light is reflected from a SPR surface, with

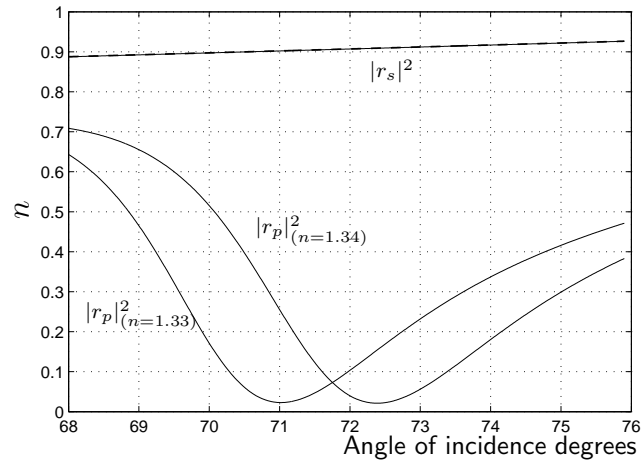


Figure 7.2: Reflectance vs angle of incidence for two refractive indices ($n = 1.33$ and $n = 1.34$). System glass $n = 1.51$ with 3 nm chromium and 45 nm of gold. Results for both s and p-polarised light are shown, with there being almost no difference between the two refractive indices for s-polarised light.

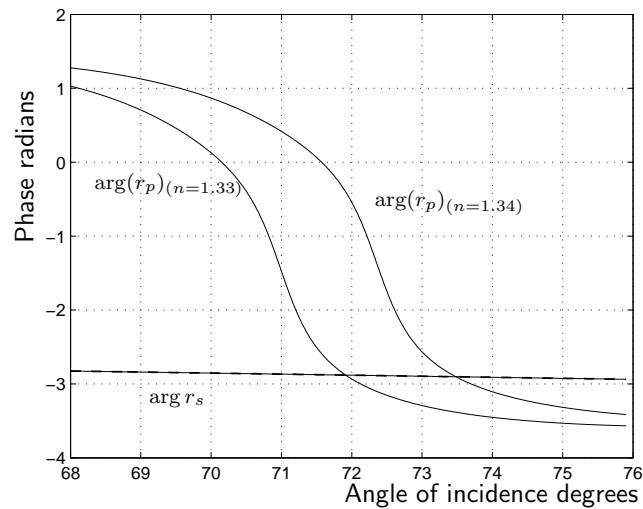


Figure 7.3: Phase change on reflection vs angle of incidence for two refractive indices ($n = 1.33$ and $n = 1.34$). The SPR system is the same as for the reflectance results above.

reflection coefficients r_{p1} and r_{s1} . A half-wave plate at 45° is then used to exchange the p and s-polarised light and the beam is reflected off a second SPR surface with reflection coefficients r_{p2} and r_{s2} . It will be shown that the amount of light transmitted through a polarisation analyser placed after the second SPR surface is sensitive to the difference in the reflection coefficients of the two surfaces.

When analysing this system, it is useful to use the Jones matrix method where the polarisation state of the light is represented by a two element vector $E = \begin{bmatrix} E_p \\ E_s \end{bmatrix}$ where E_p and E_s are the complex amplitude of the electric field of the p-polarised and s-polarised components of the light respectively. The effect of optical elements on the polarisation is then represented by 2×2 matrices.

The first SPR sensor surface has complex reflection coefficients r_{p1} and r_{s1} . If light polarised at 45° and normalised such that its intensity is $I = |E_p|^2 + |E_s|^2 = 1$, is reflected from the surface, its polarisation will change to

$$\begin{bmatrix} r_{p1} & 0 \\ 0 & r_{s1} \end{bmatrix} \frac{1}{\sqrt{2}} \begin{bmatrix} 1 \\ 1 \end{bmatrix} = \frac{1}{\sqrt{2}} \begin{bmatrix} r_{p1} \\ r_{s1} \end{bmatrix}. \quad (7.1)$$

A half-wave plate at 45° is then used to exchange the p-and s-polarised light

$$\begin{bmatrix} 0 & 1 \\ 1 & 0 \end{bmatrix} \frac{1}{\sqrt{2}} \begin{bmatrix} r_{p1} \\ r_{s1} \end{bmatrix} = \frac{1}{\sqrt{2}} \begin{bmatrix} r_{s1} \\ r_{p1} \end{bmatrix}. \quad (7.2)$$

The light is then reflected from a second SPR sensor surface with complex reflection coefficients r_{p2} and r_{s2}

$$\begin{bmatrix} r_{p2} & 0 \\ 0 & r_{s2} \end{bmatrix} \frac{1}{\sqrt{2}} \begin{bmatrix} r_{s1} \\ r_{p1} \end{bmatrix} = \frac{1}{\sqrt{2}} \begin{bmatrix} r_{p2}r_{s1} \\ r_{p1}r_{s2} \end{bmatrix}. \quad (7.3)$$

If the two surface are the same $r_{p1} = r_{p2} = r_p$ and $r_{s1} = r_{s2} = r_s$ therefore

$$\frac{r_p r_s}{\sqrt{2}} \begin{bmatrix} 1 \\ 1 \end{bmatrix}, \quad (7.4)$$

that is, the light is linearly polarised at 45° and attenuated by a factor of

$|r_p r_s|$. If the light is then incident on a polarisation analyser set with its transmission axis at -45° , the transmission will be zero.

If the reflection coefficients of the two surfaces are not identical, the transmission, T , will not be zero but can be calculated from

$$\begin{bmatrix} E_p \\ E_s \end{bmatrix} = \frac{1}{2} \begin{bmatrix} 1 & -1 \\ -1 & 1 \end{bmatrix} \frac{1}{\sqrt{2}} \begin{bmatrix} r_{p2} r_{s1} \\ r_{p1} r_{s2} \end{bmatrix} = \frac{1}{2\sqrt{2}} \begin{bmatrix} r_{p2} r_{s1} - r_{p1} r_{s2} \\ r_{p1} r_{s2} - r_{p2} r_{s1} \end{bmatrix}. \quad (7.5)$$

where $\frac{1}{\sqrt{2}} \begin{bmatrix} 1 & -1 \\ -1 & 1 \end{bmatrix}$ is the matrix for a polariser with its transmission axis at -45° from p-polarised. The input light intensity was normalised, so the transmission is

$$T = |E_p|^2 + |E_s|^2, \quad (7.6)$$

$$= \frac{1}{8} |r_{p2} r_{s1} - r_{p1} r_{s2}|^2 + \frac{1}{8} |r_{p1} r_{s2} - r_{p2} r_{s1}|^2, \quad (7.7)$$

$$= \frac{1}{4} |r_{p2} r_{s1} - r_{p1} r_{s2}|^2. \quad (7.8)$$

The s-polarised light does not couple to the plasmon and so the change in the reflection coefficient with refractive index is much smaller than for p-polarised light (see figures 7.2 and 7.3). So we can use the approximation $r_{s1} \approx r_{s2} \approx r_s$

$$T \approx \frac{1}{4} |r_s (r_{p2} - r_{p1})|^2, \quad (7.9)$$

so the transmission is proportional to the square of the difference between the p reflection coefficients for the two SPR surfaces.

Theoretical modelling of the differential SPR instrument was done using equation 7.8. The reflection coefficients were calculated using the scattering matrix method as described in appendix A. For the first results presented, the SPR system is the same as that for the simulations of chapter 3.2, 3 nm of chromium and 45 nm of gold on BK7 glass ($n = 1.51$). The reflectance and phase change for this system are plotted in figures 7.2 and 7.3. The wavelength is $\lambda = 680$ nm for all results presented in this chapter. Note that r_s is almost independent of the refractive index of the sensed medium and changes slowly with angle of incidence compared to r_p . The refractive index at the first SPR surface is defined to be n_1 and at the second surface $n_2 = n_1 + \Delta n$. The transmission as a function of the refractive index difference between

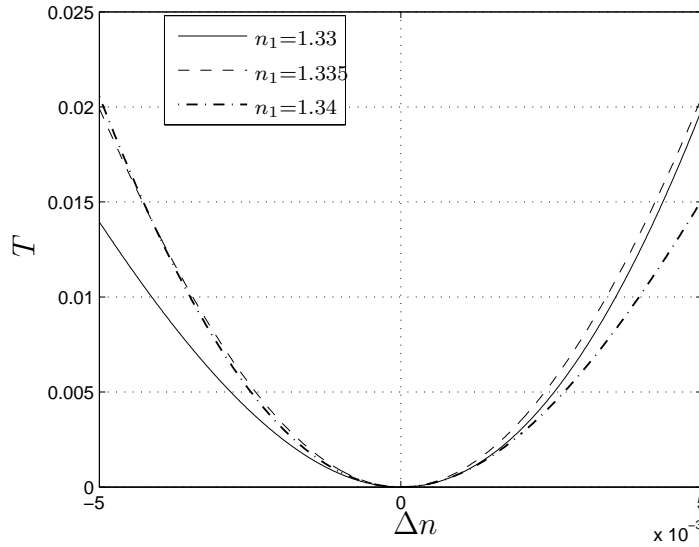


Figure 7.4: Transmission, T , for the differential SPR instrument vs the refractive index difference between the two SPR surfaces, Δn . Angle of incidence $\theta = 71^\circ$ for both reflections.

the two surfaces, $\Delta n = n_2 - n_1$, is shown in figure 7.4 for different common refractive indices, n_1 . An angle of incidence of 71° , which is approximately the value to give minimum reflectivity (the centre of the SPR dip) for $n = 1.33$, is used. The transmission is zero when $\Delta n = 0$ as expected from equation 7.8 and increases as $|\Delta n|$ increases. If the angle of incidence or n_1 were changed to move away from the surface plasmon resonance, the transmission at $\Delta n = 0$ would still be zero but the transmission would change more slowly as $|\Delta n|$ increased as the reflection coefficients change less rapidly away from the resonance. As shown in the figure, changes in Δn could be detected from changes in the transmission. However the response is non-linear (approximately quadratic) and depends on the common index n_1 for $\Delta n \neq 0$.

A more practical implementation of the differential SPR instrument is shown in figure 7.5. A mirror is used to fold the optical path so that two areas of the same SPR surface can be used for the two reflections. The half-wave plate is replaced by two passes through a quarter-wave plate and the transmission is the same as for the previous system, as given by equa-

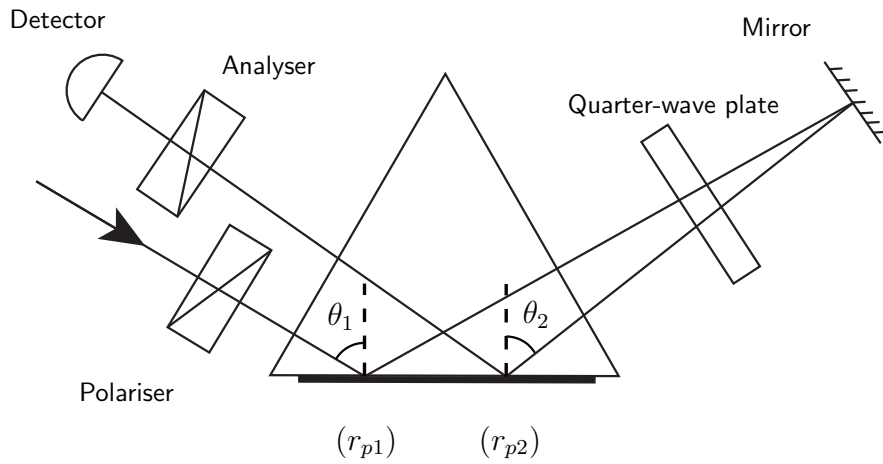


Figure 7.5: A more practical configuration for the differential SPR instrument. A movable mirror can be used to change θ_2 .

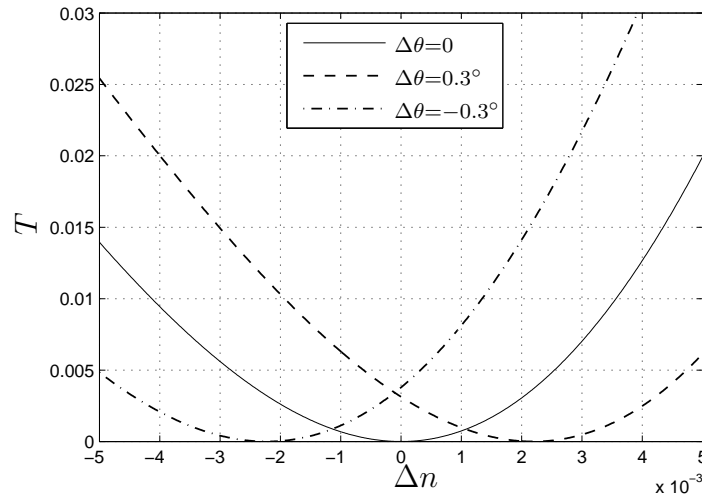


Figure 7.6: Transmission vs refractive index difference for different angle of incidence differences. The SPR system is the same as that used previously with $n_1 = 1.33$.

tion 7.8. A tilting mirror can be used to alter the angle of incidence for the second reflection (θ_2). As shown in figures 7.2 and 7.3, changing the angle of incidence has a very similar effect to changing the refractive index. The angle of incidence difference is defined as $\Delta\theta = \theta_2 - \theta_1$. Figure 7.6 shows the transmission vs Δn for different values of $\Delta\theta$. Note that changing the angle of incidence of the second reflection shifts the Δn value of the intensity minimum. While it cannot be seen in the figure, using $\Delta\theta \neq 0$ makes the minimum intensity non zero as reflection coefficients for the two reflections cannot be made exactly equal.

To give a more linear measurement of Δn , the angle of incidence difference ($\Delta\theta$) can be modulated by oscillating the mirror. We can measure the difference in transmission between $\theta_2 = \theta_1 + \Delta\theta + 0.1^\circ$ and $\theta_2 = \theta_1 + \Delta\theta - 0.1^\circ$ defining the signal as

$$S = T(\Delta\theta + 0.1^\circ) - T(\Delta\theta - 0.1^\circ). \quad (7.10)$$

This is equivalent to using a $\pm 0.1^\circ$ square wave modulation of θ_2 and measuring the amplitude of the AC signal at the modulation frequency in the detected intensity. The choice of $\pm 0.1^\circ$ amplitude is arbitrary, but is of the same order of magnitude as the modulation that will be used for my experimental work. Square wave modulation, rather than the sinusoidal modulation that will be used for my experimental work, is used as it makes the signal easier to calculate. The signal vs the refractive index difference was calculated for the same SPR system as above and is shown in figure 7.7. Near $\Delta n = 0$ the signal (S) is proportional to Δn . As $|\Delta n|$ increases, however, the response becomes non-linear and depends on the common index, n_1 . For detecting small refractive index difference changes, measuring the amplitude of the signal may be adequate.

A more linear measurement of the refractive index difference (Δn) with less sensitivity to the common index (n_1) can be obtained by measuring the angle of incidence difference where the signal is zero. Figure 7.8 shows the angle of incidence difference for zero signal, $\Delta\theta_m = \Delta\theta(S = 0)$, vs refractive index difference, for different common indices. The angle of incidence difference for zero signal was found numerically for each Δn value by calculating the signal (S) for a range of $\Delta\theta$ values and finding the minimum. As can be seen in the figure, the $\Delta\theta_m$ result is very close to linear and almost indepen-

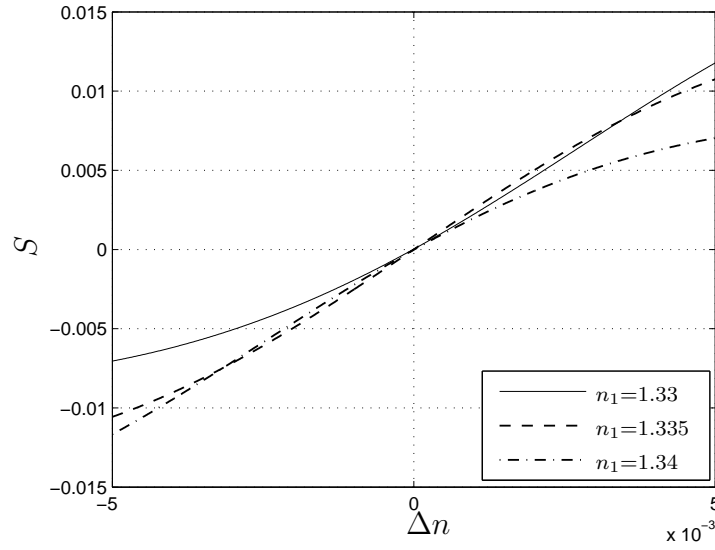


Figure 7.7: Signal (S) vs refractive index difference (Δn) for different common indices (n_1). Angle of incidence $\theta_1 = 71^\circ$ and $\Delta\theta = 0$.

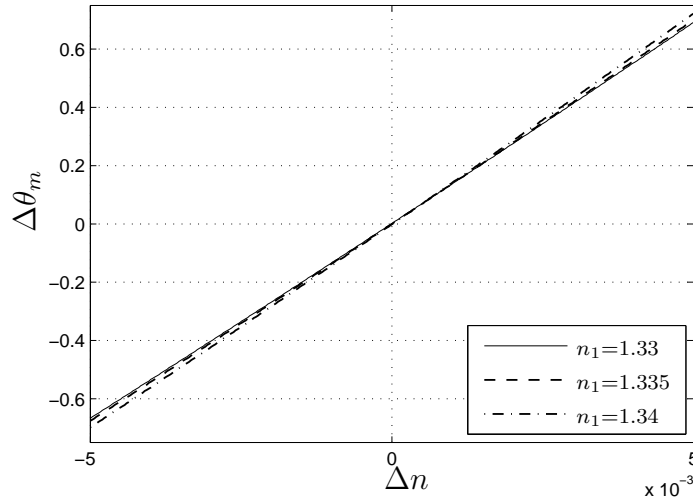


Figure 7.8: Angle of incidence difference for zero signal ($\Delta\theta_m$) vs refractive index difference (Δn) for different common indices (n_1). System 3 nm of chromium and 45 nm of gold on glass ($n = 1.51$) as above, $\theta_1 = 71^\circ$.

dent of the common index. This technique of measuring $\Delta\theta_m$ to detect the refractive index difference was therefore used for my experimental work.

7.2 Different SPR systems

The use of different SPR systems may change the measurement, and theoretical results for three SPR systems are compared in this section. The first system is that used for all the theoretical results presented so far with 3 nm chromium and 45 nm gold ($N = 0.161 + 3.64i$) on glass ($n = 1.51$) at 71° angle of incidence with $\lambda = 680$ nm. The second system is the same as before except with 55 nm rather than 45 nm of gold. The variation in the thickness has a significant effect on the shape and steepness of the phase change at the resonance, as was shown in figure 2.9. The third system is chosen to be similar to the SPR system found to be a better fit for the experimentally determined reflectance vs angle of incidence measurements of a gold coated slide in chapter 5.2. This system has 6 nm of chromium and 45 nm of gold with the refractive index of the gold changed to $N = 0.24 + 3.85i$. The different refractive index of the gold has the effect of making the dip in the reflectance due to the surface plasmon resonance wider and moving it to a smaller angle of incidence, as was shown in figure 5.8. For the results for the third system, the angle of incidence was changed to 70° or approximately the reflectance minimum for that system with $n = 1.33$.

The results for measuring the amplitude of the signal (S) are shown in figure 7.9. They have a similar form for all systems, with the main difference being a variation in the sensitivity $dS/d(\Delta n)$. The lower sensitivity of the signal to the refractive index difference for the third system is expected as for this system the resonance dip is wider so r_p changes less rapidly with angle of incidence or refractive index. From equation 7.9, the transmission is approximately proportional to the square of the difference of the p reflection coefficients for the two reflections. So if the resonance dip is wider the transmission and thus the signal should change more slowly as a function of refractive index difference.

The results for measuring the angle of incidence difference for zero signal for the three SPR systems are shown in figure 7.10. These are very similar

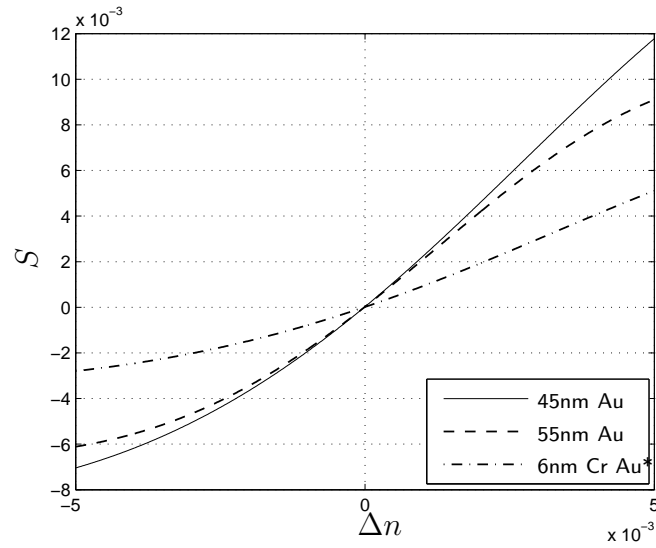


Figure 7.9: Signal vs refractive index difference for three SPR systems, $n_1 = 1.33$. The first system (45 nm Au) is the same as previously 3 nm chromium and 45 nm gold with the angle of incidence 71° the second system (55 nm) is the same except that the gold thickness is 55 nm. The third system (6 nm Cr Au*) is 6 nm of chromium and 45 nm gold with the index of gold changed to $N = 0.24 + 3.85i$ and the angle of incidence 70° .

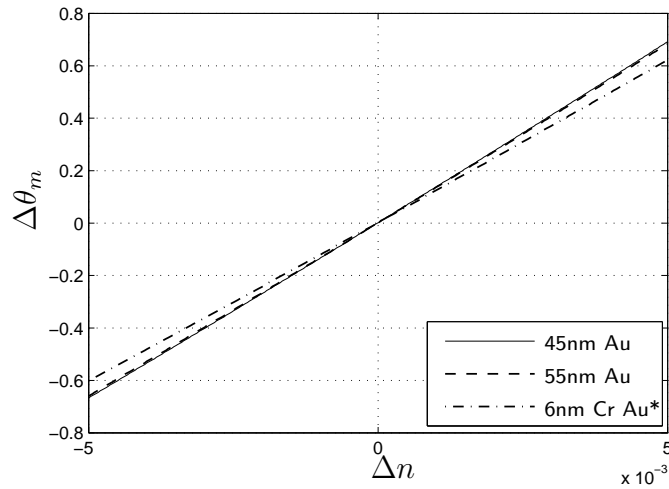


Figure 7.10: Angle of incidence difference for zero signal vs refractive index difference for the same three SPR systems as the above figure.

and linear for all three systems. The only obvious difference is that the sensitivity $d(\Delta\theta)/d(\Delta n)$ is slightly lower for the third SPR system. The wider resonance will reduce the rate at which the signal changes with angle of incidence difference changes ($dS/d(\Delta\theta)$) (just as it reduces ($dS/\Delta n$) as shown in figure 7.9) and this may affect the accuracy of the $\Delta\theta_m$ measurement.

From these results, it appears that measuring the angle of incidence difference for zero signal should work similarly for all three SPR systems presented. It is expected that this technique should work in general for any system where there is a SPR resonance and thus a p reflection coefficient that changes rapidly and in a similar way as the angle of incidence or refractive index changes.

7.3 Differences between the two SPR surfaces

All of the previous simulations of this chapter have assumed the SPR surfaces at the location of the first and second reflections are identical, except for the refractive index of the sensed medium. The measurements made with the polarisation imaging instrument presented in chapter 6 show significant variation in the input polarisation for minimum transmission, ψ_m , and its sensitivity to refractive index changes, $d\psi_m/dn$. It is believed that these variations are the result of variations in the properties of the gold surface, in particular the thickness and optical constants of the layers or roughness. It is therefore necessary to consider the effect that differences between the properties of the two SPR surfaces will have on the differential measurement.

Modelling was done for a system where the SPR surface for the first reflection was the same as that used for most of the results presented earlier, 3 nm of chromium and 45 nm of gold on glass $n = 1.51$ and the second SPR surface differed only in that the gold layer was 47 nm thick. Note that this thickness difference is much smaller than that shown for both surfaces above (55 nm) that had almost no effect on the measurement. Results for the angle of incidence difference for minimum signal ($\Delta\theta_m$) for this system were calculated as for the results presented previously and are shown in figure 7.11. The response to changes in Δn is very similar to the results presented for a system with two identical SPR surfaces presented in figure 7.8. However the

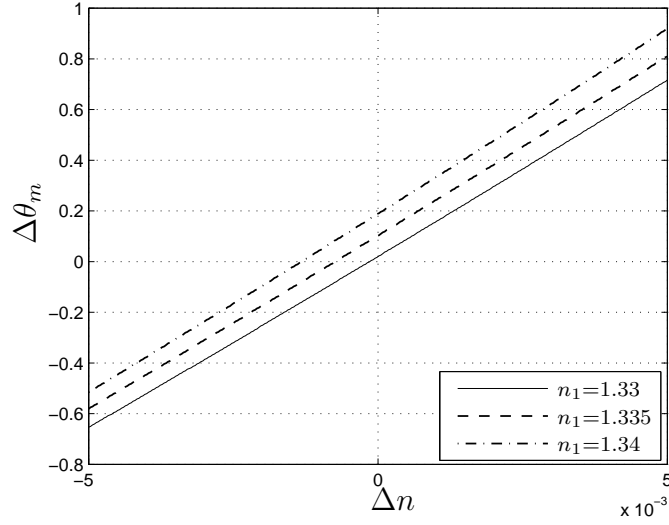


Figure 7.11: Angle of incidence difference for zero signal vs refractive index difference for different common refractive indices. Results are for the system with 45 nm gold on the first SPR surface and 47 nm on the second one described in the text.

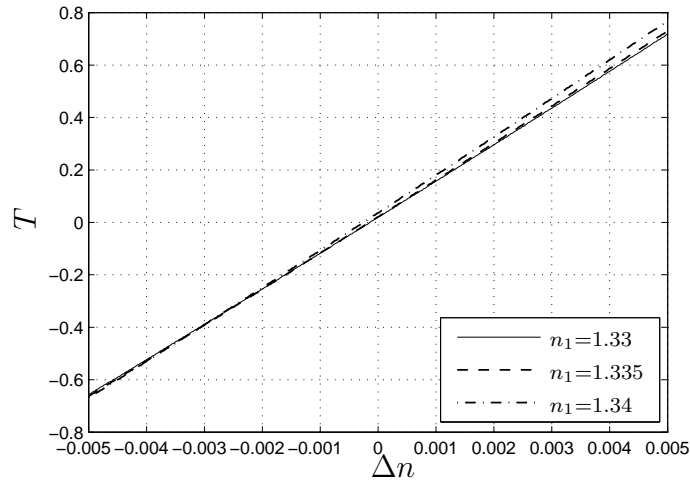


Figure 7.12: Angle of incidence difference for zero signal vs refractive index difference for different common refractive indices. Results are for the same SPR system as the figure above with the analyser moved to $\phi = -50.5^\circ$ to compensate for the difference between the two surfaces.

difference between the two SPR surfaces has a large effect on the instrument's response to changes in the common index, n_1 . For the results presented earlier for identical SPR surfaces, changes in n_1 had a negligible effect on $\Delta\theta_m$ for $\Delta n = 0$ and only a small effect when $\Delta n \neq 0$. With the thickness difference between the two SPR surfaces, changes in n_1 add an offset to the $\Delta\theta_m$ vs Δn result, that is, the instrument is now sensitive to changes in the common refractive index as well as the difference in the refractive indices. The sensitivity to the common index is a problem as the purpose of this instrument is to allow small changes in the refractive index difference to be detected in the presence of variations in the common index so as to distinguish a binding reaction occurring at one sensor surface from a change in the bulk index of the solution.

The sensitivity to common index changes when the two SPR surfaces are different is because as the common index changes, the reflection coefficient of one surface will change faster than the other. The angle of incidence difference for zero signal, $\Delta\theta_m$, will be approximately the point of minimum transmission where the difference between the reflection coefficients is a minimum (see equation 7.8). So if the common index changes, to maintain minimum transmission the angle of incidence difference must be changed such that the difference between the reflection coefficients for the two surfaces is again a minimum.

This effect can be compensated for, and the insensitivity to common refractive index changes restored, by changing the setting of the polariser or analyser. To explain why this works it is necessary to examine the transmission of the instrument when the analyser is set to an azimuthal angle other than -45° as previously assumed. The light incident on the analyser has the state

$$\frac{1}{\sqrt{2}} \begin{bmatrix} r_{p2}r_{s1} \\ r_{p1}r_{s2} \end{bmatrix}, \quad (7.11)$$

as shown in equation 7.3 above. A polariser with its transmission axis at an angle ϕ is represented by the matrix for a polariser at $\phi = 0$ and two rotation matrices

$$\begin{bmatrix} \cos \phi & -\sin \phi \\ \sin \phi & \cos \phi \end{bmatrix} \begin{bmatrix} 1 & 0 \\ 0 & 0 \end{bmatrix} \begin{bmatrix} \cos \phi & \sin \phi \\ -\sin \phi & \cos \phi \end{bmatrix}. \quad (7.12)$$

For the purpose of calculating the transmission, the second rotation matrix

can be neglected. This will give a state with the right intensity but p-polarised rather than linearly polarised at ϕ

$$\begin{bmatrix} 1 & 0 \\ 0 & 0 \end{bmatrix} \begin{bmatrix} \cos \phi & \sin \phi \\ -\sin \phi & \cos \phi \end{bmatrix} \frac{1}{\sqrt{2}} \begin{bmatrix} r_{p2}r_{s1} \\ r_{p1}r_{s2} \end{bmatrix} = \frac{1}{\sqrt{2}} \begin{bmatrix} \cos \phi r_{p2}r_{s1} + \sin \phi r_{p1}r_{s2} \\ 0 \end{bmatrix}. \quad (7.13)$$

So, as the initial state of the light was normalised such that its intensity was 1 (see equation 7.1) the transmission of the optical system is

$$T = |E_p|^2 + |E_s|^2, \quad (7.14)$$

$$= \frac{1}{2} |\cos \phi r_{p2}r_{s1} + \sin \phi r_{p1}r_{s2}|^2. \quad (7.15)$$

The approximation that the reflection coefficients for s-polarised light are the same can be used again

$$T \approx \frac{1}{2} |r_{s1}(\cos \phi r_{p2} + \sin \phi r_{p1})|^2. \quad (7.16)$$

With $\phi = -45^\circ$, $\cos \phi = 1/\sqrt{2}$, $\sin \phi = -1/\sqrt{2}$ we get the same result as before, that the transmission is proportional to the square of the difference of the p reflection coefficients. If the p reflection coefficient for one of the surfaces changes more quickly as the index changes, ϕ can be adjusted such that the transmission will not change as n_1 changes. The difference in the rate at which the reflection coefficients for the two surfaces change will depend on the refractive index and angle of incidence, so this compensation will only be effective over a limited range. An equivalent compensation can be achieved by changing the polariser setting rather than the analyser and this will be used experimentally.

Adjusting the analyser azimuthal angle to compensate for differences in the response of the two SPR surfaces is shown in figure 7.12. This is the same system as figure 7.11 except that the analyser setting has been changed to $\phi = -50.5^\circ$. By comparing the figures it can be seen that the sensitivity to changes in the common refractive index has been greatly reduced. The value of $\phi = -50.5^\circ$ was obtained by plotting the angle of incidence difference for zero signal, $\Delta\theta_m$, against the common index, n_1 , for different values of ϕ to find the best compensation over the range $1.33 \leq n_1 \leq 1.335$. Examples of these plots are shown in figure 7.13.

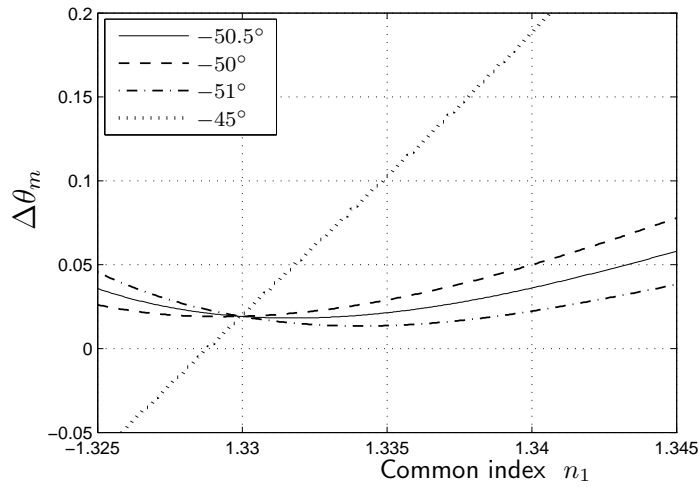


Figure 7.13: Angle of incidence difference for zero signal vs the common index for different settings of the analyser. Results are for the system where the two SPR surfaces have 45 and 47 nm of gold described in the text.

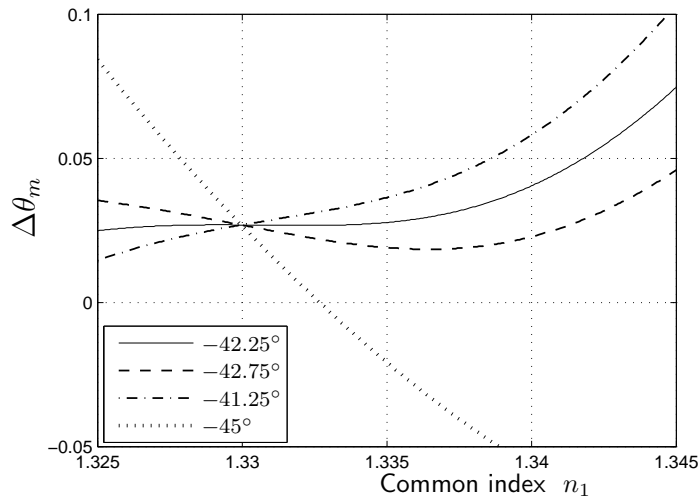


Figure 7.14: Angle of incidence difference for zero signal vs the common index for different settings of the analyser. Results are for the system where the refractive index of the gold for the second SPR surface has been changed.

Adjusting the analyser to compensate for differences between the two SPR surfaces was also investigated for a system where the difference was in the optical properties, rather than the thickness of the gold layer. The first SPR surface is the same as before, 3 nm of chromium and 45 nm of gold ($N = 0.16 + 3.64i$). For the second surface, the loss ($\Im(\epsilon)$) of the gold was increased by 50 % giving a refractive index of $N = 0.24 + 3.65i$. This was chosen as increasing the loss increases the width of the SPR resonance dip making the p reflection coefficient change less rapidly with refractive index. This, or loss caused by roughness of the gold, is considered to be a likely explanation for the variation in the sensitivity $d\psi_m/dn$ across the gold surfaces for the polarisation imaging results presented in chapter 6. $\Delta\theta_m$ vs the common index n_1 is plotted for this system in figure 7.14. As for the previous system, adjusting the analyser setting can significantly reduce the sensitivity of the instrument to common index changes over a limited common index range.

7.4 Noise

An estimate can be made of the accuracy of the differential SPR instrument to see if high accuracy measurements are possible. As described above, the angle of incidence difference where the signal is zero, $\Delta\theta_m$, is found. The signal is defined as

$$S = T(\Delta\theta + 0.1^\circ) - T(\Delta\theta - 0.1^\circ), \quad (7.17)$$

or the difference in transmission between $\Delta\theta + 0.1^\circ$ and $\Delta\theta - 0.1^\circ$. The signal can be generated by oscillating the mirror by $\pm 0.05^\circ$, detecting the transmitted light and measuring the amplitude of the AC component of the detected intensity at the modulation frequency. Square wave modulation is used here for simplicity but sinusoidal modulation will be used experimentally. As the signal is zero at $\Delta\theta_m$ and varies linearly close to $\Delta\theta_m$ a simple feedback loop controlling the mirror should be able to maintain $\Delta\theta = \Delta\theta_m$.

The accuracy with which $\Delta\theta_m$ can be maintained may be determined by the noise in the signal. At $\Delta\theta_m$, where the signal is zero, the noise in the signal will be equal to the noise in the measured transmission at $\Delta\theta_m + 0.1^\circ$

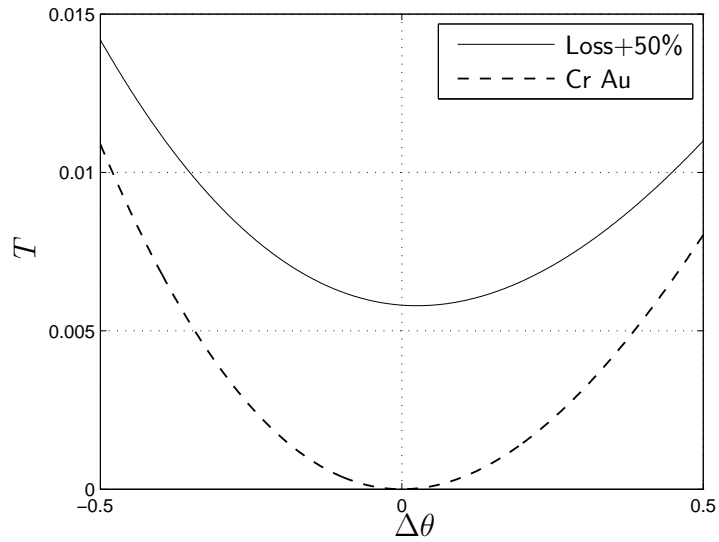


Figure 7.15: Transmission vs angle of incidence difference. The system where the loss of the second gold surface is increased and the system where both surfaces are identical 3 nm chromium and 45 nm gold are shown.

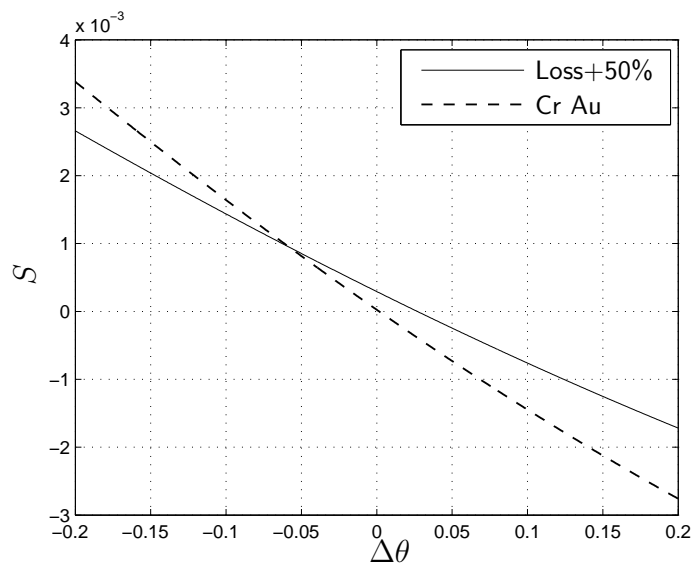


Figure 7.16: Signal vs angle of index difference for the same two differential SPR systems as above.

or $\Delta\theta_m - 0.1^\circ$

$$N_S(S = 0) = N_{T(\Delta\theta_m + 0.1^\circ)}. \quad (7.18)$$

I assume that the measurement is limited by the shot noise (photon statistics) of the detected light. As for this instrument only a single detector is needed and so a photodiode can be used, it is not necessary to consider the effect on the noise of detector saturation, as was necessary for the imaging instrument (see chapter 3.3). The transmission is $T = I_D/I_E$ where I_D is the number of photons detected in the measurement time and I_E is the number of photons emitted by the source in the measurement time. The shot noise in the transmission measurement is then

$$N_{shot} = \sqrt{I_D}/I_E = \sqrt{I_E T}/I_E = \sqrt{T/I_E}. \quad (7.19)$$

So the noise in the signal due to the shot noise will be

$$N_S(S = 0) = \sqrt{\frac{T(\Delta\theta_m + 0.1^\circ)}{I_E}}. \quad (7.20)$$

The number of photons emitted in the measurement time is calculated for an input power of 0.001 W, a measurement time of 1 second and light at $\lambda = 680$ nm where the energy in one photon is 1.82 eV. A factor of 0.5 is included to account for a detector with a realistic quantum efficiency.

$$I_E = \frac{0.001 \times 1 \times 0.5}{1.82 \times e} = 1.72 \times 10^{15}. \quad (7.21)$$

Note e here is the charge on an electron $1.6 \times 10^{-19}C$ to convert from eV to joules.

The transmission vs $\Delta\theta$ is plotted in figure 7.15 for the system with both SPR surfaces 3 nm chromium and 45 nm of gold used in the theoretical results above. The transmission for the system where the optical properties of the gold for the second SPR surface were altered by increasing the loss, as used for figure 7.14, are also shown. For the results where the two SPR surfaces differ, the analyser is set to $\phi = 42.25^\circ$ to compensate for the difference as described in section 7.3. For the system with two identical SPR surfaces the transmission drops to zero when $\Delta\theta = 0$ as expected from equation 7.8. However for the system where the two surfaces differ, the transmission does

not drop to zero.

The noise of the $\Delta\theta_m$ result will be

$$N_{\Delta\theta_m} = N_S(S=0) \times \frac{dS}{d(\Delta\theta)}(\Delta\theta_m), \quad (7.22)$$

where $dS/d(\Delta\theta)$ can be found from the plot of S vs $\Delta\theta$ in figure 7.16.

The noise in $\Delta\theta_m$ in the shot noise limit for the system with identical SPR surfaces is 7.33×10^{-12} degrees. Or converting to the noise in the refractive index 1.0×10^{-9} RIU.

For the system where the loss is increased for the second surface the noise is 2.04×10^{-11} degrees or 2.9×10^{-9} RIU. The noise is higher for the second system due to the increased transmission (see figure 7.15) and the decreased $dS/d(\Delta\theta)$ (see figure 7.16).

The accuracy with which the refractive index difference can be detected in the shot noise limit is very high and it is expected that other noise sources will dominate. These results do suggest that high accuracy measurements may be possible with this system.

8 Differential SPR apparatus

This chapter describes the experimental apparatus used for my differential SPR instrument. Figure 8.1 shows the equipment used and the arrangement on the optical table. A beam from a super luminescent diode (SLD) is passed through a polariser to set the initial polarisation. The beam is then reflected from a SPR system, a prism with a gold coated microscope slide index matched to it. A mirror is used to steer the beam so that it is again reflected from the SPR surface, this time at a point on the surface ~ 10 mm below the first reflection. The mirror is mounted on a piezo bender actuator to allow it to be tilted to control the angle of incidence of the second reflection

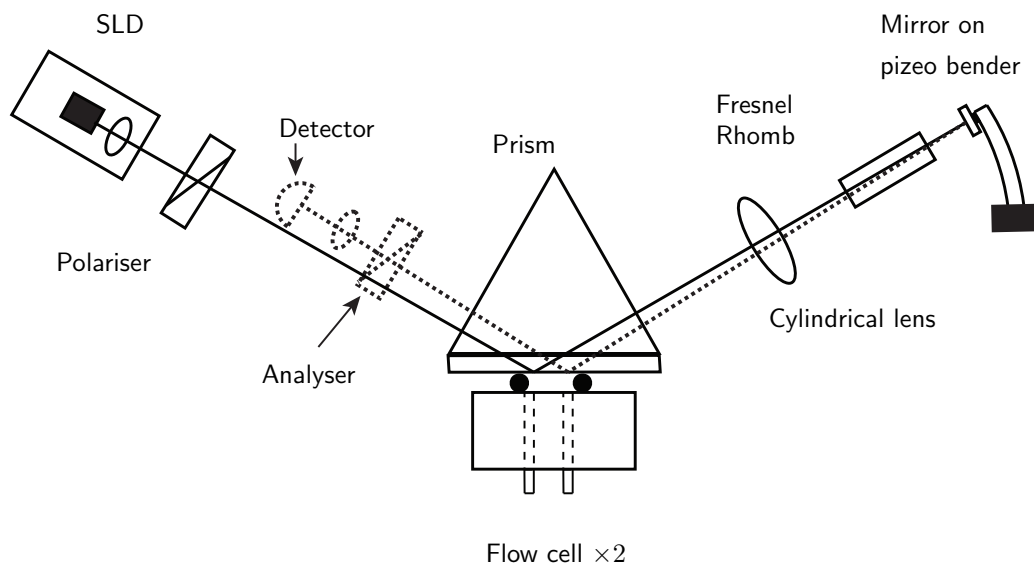


Figure 8.1: The experimental apparatus for the differential SPR measurements. The parts shown as dotted lines are below the rest of the apparatus.

from the SPR surface. A cylindrical lens between the mirror and the prism is used to stop the beam moving across the SPR surface when the angle of incidence is changed. A Fresnel rhomb quarter-wave plate is placed next to the mirror with both beams passing through it. After the second reflection from the SPR surface the beam is incident on a polarisation analyser. The light transmitted through the analyser is then focused onto a photodiode. An aluminium block with two flow cells is clamped to the SPR surface. The top flow cell covers the area of the SPR surface where the first reflection occurs and the bottom flow cell covers the area where the second reflection occurs. The angle of incidence at the second reflection is modulated sinusoidally using the piezo bender. The AC component of the intensity at the modulation frequency is detected using a phase sensitive detector. A simple feedback loop controlling the piezo bender is used to adjust the angle of incidence of the second reflection such that the output of the phase sensitive detector is zero.

8.1 Apparatus details

8.1.1 Light source and polariser

The light source was the same QSDM680-9 super luminescent diode (SLD) used for the imaging SPR instrument, centre wavelength 677 nm, spectral width 7.5 nm FWHM. The diode mount's aspheric collimation lens was adjusted to focus the beam to a waist near the mirror. The same Glan-Thompson polariser mounted in a Newport SR50 rotation stage as used for the imaging instrument was also used. An aperture between the polariser and the SLD limited the beam diameter to 3 mm. The intensity of the beam after the polariser was ~ 1.5 mW.

8.1.2 Prism and flow cell

The prism and flow cell arrangement was the same as that for the imaging instrument (see chapter 4.1.3) except that an aluminium block with grooves for two 10 mm diameter O-rings rather than one 20 mm diameter one was used. Figure 8.2 shows the arrangement of the SPR system and the flow cell.

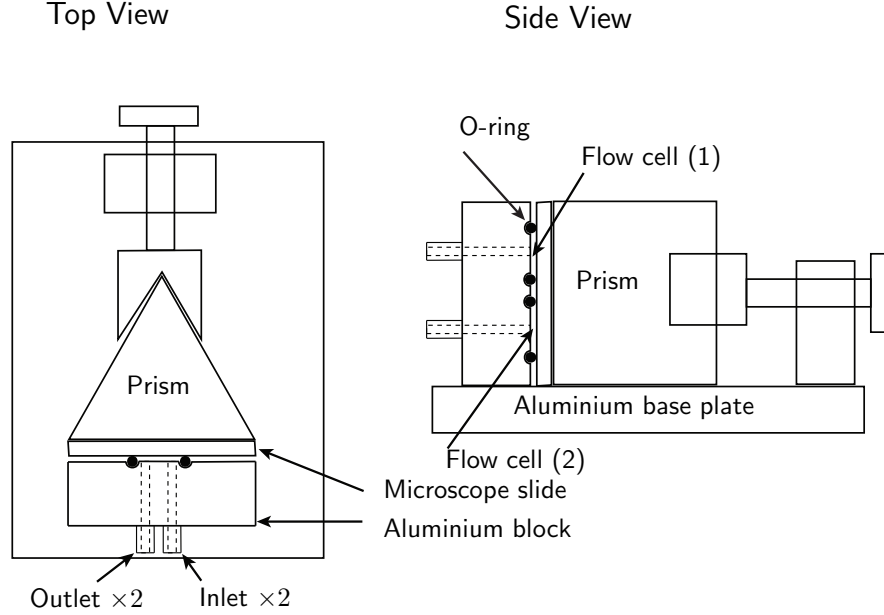


Figure 8.2: The arrangement of the prism and flow cells.

The same high index (SF2 glass $n = 1.64$) prism was used with a gold coated microscope slide ($n = 1.50$) index matched to it with oil (Cargile $n = 1.51$). The slide was cleaned and coated with a 3 nm adhesion layer of chromium and ~ 42 nm of gold by thermal evaporation as for the imaging measurements. The spaces between the block and the gold coated slide within each O-ring formed the top and bottom flow cells, each less than 0.1 ml in volume. Two holes drilled through the block into each flow cell, with plastic pipe fittings on the outside, formed the inlet and outlet. Each flow cell inlet was connected through a 4–1 selector valve to four plastic 60 ml syringes that could contain distilled water or salt solutions with different refractive indices. The same syringes and Tygon tubing as for the imaging measurements were used. A tube from the outlet of each flow cell led to a waste bucket. When changing the solution in a flow cell, at least 5 ml of the new solution was flowed through the cell to ensure the previous solution was completely replaced.

A Peltier thermoelectric cooler (TEC) driven by a PID controller was again used to allow the temperature of the flow cell to be controlled. For the imaging measurements, the prism and flow cell were mounted on a rotation stage to allow the angle of incidence to be controlled. This rotation stage was

not available for the differential SPR measurements so the prism mount was clamped directly to the optical table. The mount was adjusted to minimise the reflectivity for p-polarised light with the flow cells filled with water. From the results obtained for a similar gold slide in chapter 5.2 this is expected to be an angle of incidence at the gold surface of approximately 72° . The actual angle of incidence was not measured.

8.1.3 Angle of incidence control

The angle of incidence of the second reflection from the SPR surface was controlled using a movable mirror. The mirror was a 5 mm piece of microscope cover slip with the same gold coating as the SPR surface. The mirror was glued to the end of a noliac¹ CMBP03 piezo bender actuator. The other end of the actuator was clamped to a mirror mount on top of a Newport SR50 rotation stage. The actuator consists of a thin rectangle formed from two layers of piezoelectric material, with electrodes, sandwiched together. When a voltage is applied, one layer expands while the other layer contracts, causing the actuator to bend. The actuator is 21 mm long and for its maximum ± 100 volt range, if one end is fixed, the other end moves by $\pm 85\mu\text{m}$. If the actuator is assumed to always have a constant curvature along its length, this corresponds to a change of $\pm 0.46^\circ$ in the angle of the mirror. For all my differential results the ± 30 V amplifier that was used to drive the imaging instrument's modulator was used to drive the piezo. The angular range of the mirror was thus $\pm 0.14^\circ$ or $\pm 0.28^\circ$ change in the reflected beam. The mirror was placed 30 cm from the prism and a 7.5 cm focal length cylindrical lens was placed halfway between them to reduce the movement of the beam across the SPR surface as the angle of the mirror changes.

8.1.4 Fresnel Rhomb

A Thorlabs Fresnel rhomb quarter-wave plate was used for the differential instrument. As shown in figure 8.3, this is a glass block where the beam is totally internally reflected twice. The block is shaped such that the phase difference between the reflection coefficients is $\pi/4$ for each reflection adding

¹ www.noliac.com

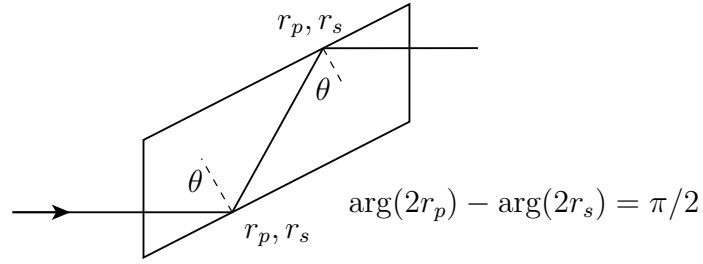


Figure 8.3: Fresnel rhomb quarter-wave plate.

up to a total $\lambda/4$ retardance. This was used rather than a quartz wave-plate as it is almost achromatic, the only change in the retardance with wavelength is that caused by the dispersion of the glass. This allows the SLD to be used as the light source avoiding any interference fringes. The Fresnel rhomb was mounted in a manual rotation stage and was set at 45° to p-polarised.

8.1.5 Analyser and detector

The polarisation analyser was a Lambda Research Optics broadband near infra-red polarising beam-splitter cube. It was clamped in a v-mount so that its transmission axis was -45° from p-polarised. The light transmitted through the analyser was then focused onto a photodiode with a $f = 70$ mm lens. An aperture between the lens and the photodiode blocked light reflected at the prism-slide interface.

8.2 Electronics

This section describes the electronics used for the differential SPR instrument. The electronics were constructed on copper coated board and, with the exception of the piezo driver, run off a ± 7 V supply.

8.2.1 Photodiode

A Vishay BPW34 PIN photodiode was used as the detector. This was directly connected to a front-end amplifier constructed using a National LF356

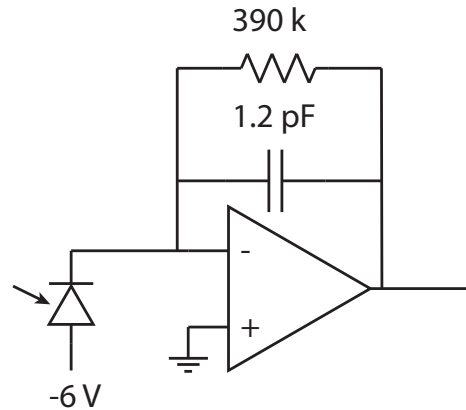


Figure 8.4: Photodiode front-end amplifier.

operational amplifier. A detailed explanation of this circuit's design and noise performance is given in Hobbs [81].

8.2.2 Phase sensitive detector

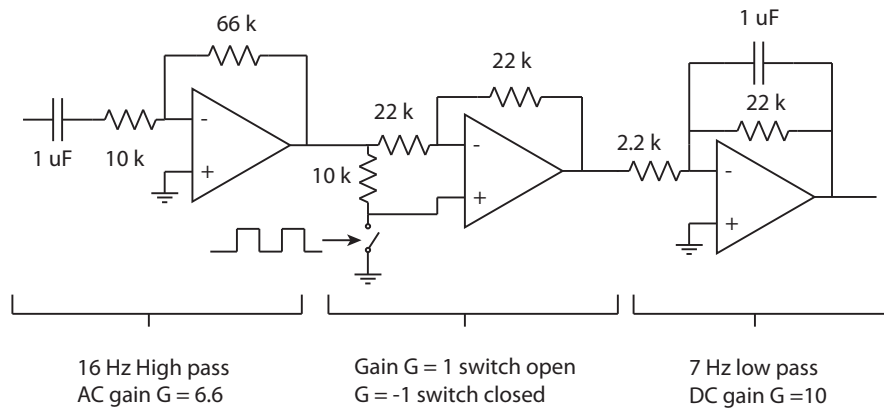


Figure 8.5: Phase sensitive detector circuit.

To measure the amplitude of the signal at the modulation frequency, a simple phase sensitive detector was constructed. The signal from the photodiode front-end was first amplified and the DC component removed. The phase sensitive detector was an amplifier with its gain switched between 1 and -1 by a CMOS switch. The switch was controlled by a square wave at

the modulation frequency from an op-amp used as a comparator with one input AC coupled to the piezo's drive signal and the other input grounded. This operation is equivalent to multiplying the signal from the photodiode by a square wave. So the DC component of the output is proportional to the amplitude of the signal at the modulation frequency² times the cosine of the phase difference between the signal and the square wave. The signal was then amplified and low pass filtered. A National L347 quad op-amp and a CD4066 CMOS switch were used for this circuit.

8.2.3 Piezo driver and PI controller

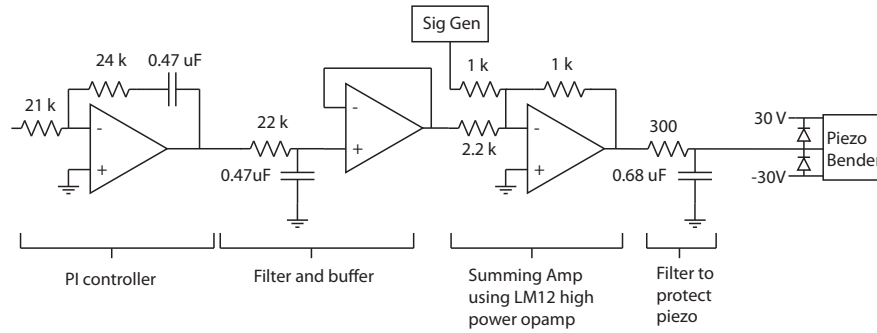


Figure 8.6: Piezo driver and PI controller circuit.

A simple proportional–integral (PI)³ controller was used to maintain the mean angle of incidence at the point where the amplitude of the signal at the modulation frequency and thus the output of the phase sensitive detector was zero. The circuit for the single op-amp PI controller, an op amp integrator with an extra resistor to give the proportional component is shown above. A low pass filter at the output of the controller was used to protect the piezo from any large, rapid voltage changes caused by any malfunction of the controller. Large voltage steps applied to the piezo bender cause high accelerations and vibration that may damage it. The piezo was driven by the output of a summing amplifier using a National LM12 high power op-amp running off a ± 30 V supply. As well as the signal from the PI controller the

²Plus terms due to the even harmonics.

³This is the same as a PID controller with zero derivative component.

other input to the summing amplifier was a ~ 400 Hz sine wave from a signal generator to produce the angle of incidence modulation. This is the same amplifier that was used to drive the modulator's coil for the polarisation imaging experiments. A 780 Hz low pass filter between the amplifier and the piezo was again used to provide protection against sudden voltage changes. The signal used to generate the square wave for the phase sensitive detector was taken after the filter so that the filter's phase shift does not affect the experiment. A TL084 quad op-amp was used for the PI controller and buffer. For all the experimental results that will be presented, the amplitude of the piezo modulation was 18 V peak to peak or approximately a $\pm 0.08^\circ$ variation in the angle of incidence.

8.3 Position sensitive detector

The system described above accurately maintains the angle of incidence at the second SPR surface at the point where the signal at the modulation frequency is zero. To make differential SPR measurements as described in the previous chapter, changes in the angle of incidence must be monitored. It is not sufficient to simply monitor the piezo's drive voltage as there is substantial hysteresis in the relationship between the angle of the mirror and the applied voltage. Strain gauges were glued to the piezo in a bridge configuration to monitor its bending but this showed similar hysteresis to the drive voltage. The change in the angle of a beam reflected from the mirror on the piezo bender was therefore measured directly with a position sensitive detector (PSD).

Figure 8.7 shows the components used to detect changes in the angle of the mirror. These can be added to figure 8.1 to give the complete experimental apparatus. A beam from the SLD was reflected off the mirror and then incident on the PSD. As the angle of the mirror changes, the beam will move across the PSD and the position change can be detected. The beam used is the light that is reflected from the front face of the prism and a fixed mirror is used to steer it to the mirror mounted on the piezo. The position sensitive detector was a Hamamatsu S3931. This is a photodiode with a 6×1 mm active area. The anode has a resistive layer and two connections, one at each end of the active area. The photo-current splits between the two connections.

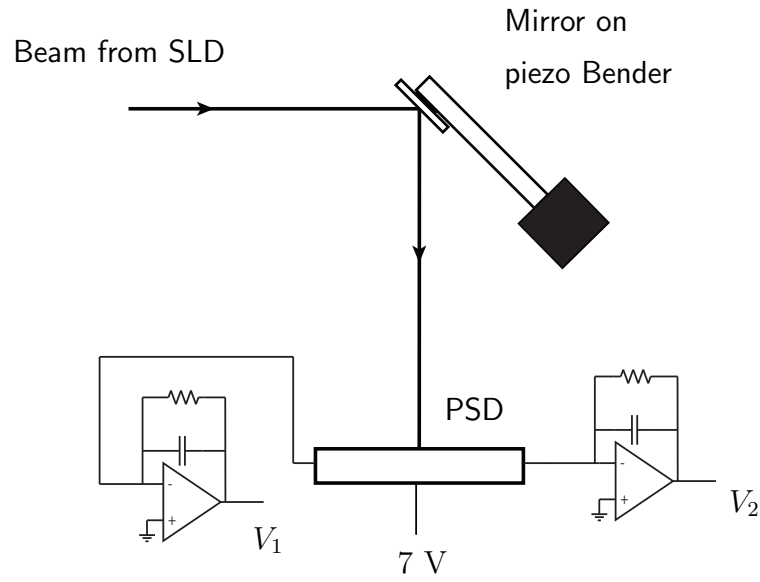


Figure 8.7: Apparatus used to detect changes in the angle of the mirror.

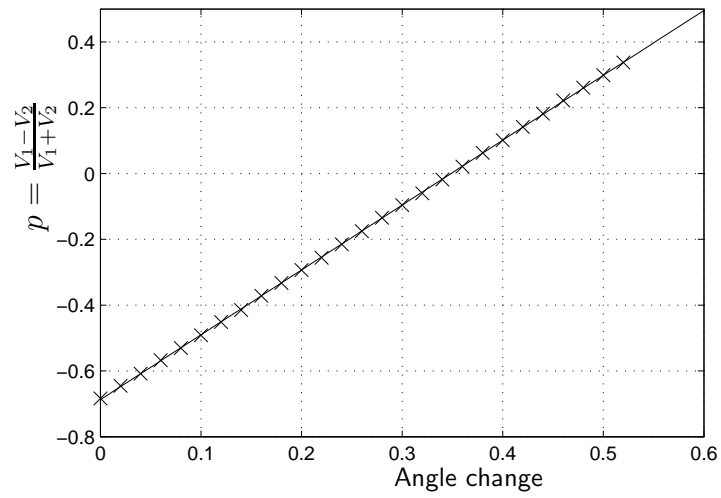


Figure 8.8: Position on the PSD , p , vs change in the angle of the reflected beam.

The position of the light spot on the detector (p) can be found from the two photo-currents i_1 and i_2 by

$$p = \frac{i_1 - i_2}{i_1 + i_2}, \quad (8.1)$$

where $p = 0$ is the centre of the detector and $p = 1, -1$ are full scale. The cathode is common and is used to reverse bias the diode. Two photodiode front-end amplifiers, as used for the other photodiode (section 8.2.1), were used to convert the photo-currents to voltages V_1 and V_2 . These used LF356 op-amps, 100 k Ω resistors and 0.68 μ F capacitors. The large capacitor is used to limit the bandwidth to 2.3 Hz (3dB) to remove the signal due to the angle of incidence modulation. When making differential SPR measurements, 10000 measurements of both output voltages were made over a one second period, using the 12 bit analogue-to-digital converter of a Measurement Computing PC1001 data acquisition card mounted in a PC, and then averaged. The position (p) was then calculated and recorded. The PSD was mounted 0.36 meters from the piezo.

To allow the measured position to be converted to the angle of incidence, a calibration measurement was made. With the PI controller removed but the modulation on, the rotation stage that the piezo was mounted on was moved in 0.01 $^\circ$ increments. This stepped the angle of the reflected beam by 0.02 $^\circ$ increments. The position was measured as the rotation stage was stepped and the result is shown in figure 8.8 with a linear least mean squares fit. The data, which covers a range larger than the piezo can move, is highly linear and the fitted gradient of p vs angle is 1.97 per degree. So the position can be directly converted to the angle of incidence at the prism. The angle at the prism is converted to angle of incidence at the second SPR surface using Snell's law at the air-prism and prism-slide interfaces, assuming the angle of incidence is close to 72 $^\circ$. The noise in the position, measured as the mean standard deviation for 5 one minute intervals, was $N_p = 2.2 \times 10^{-4}$ or approximately 0.7 μ m. This is equivalent to a noise in the angle of incidence at the second SPR surface of $N_\theta = 1.2 \times 10^{-4}$ $^\circ$.

9 Differential SPR measurements

This chapter presents measurements made with the differential SPR instrument described in the previous two chapters.

9.1 Response to small index changes

To measure the response of the differential instrument to refractive index changes, solutions of known index were needed. Three solutions were prepared by mixing distilled water with salt (NaCl). The solutions were stirred until all visible salt crystals had dissolved and then left for at least a day in covered containers to ensure that the salt had completely dissolved and the solutions were at ambient temperature. The difference in refractive index between the solutions and pure water ($n = 1.33$) was calculated from linear fitting to data from the CRC handbook [79] as for the solutions used for the imaging measurements (see figure 6.1). The refractive indices of the solutions used are given in the table below.

Solution	NaCl % w/w	$n - 1.33$
(0)	0	0
(1)	0.25	0.00044
(2)	0.50	0.00088
(3)	0.76	0.00133

Table 9.1: Solutions used to characterise the differential instrument.

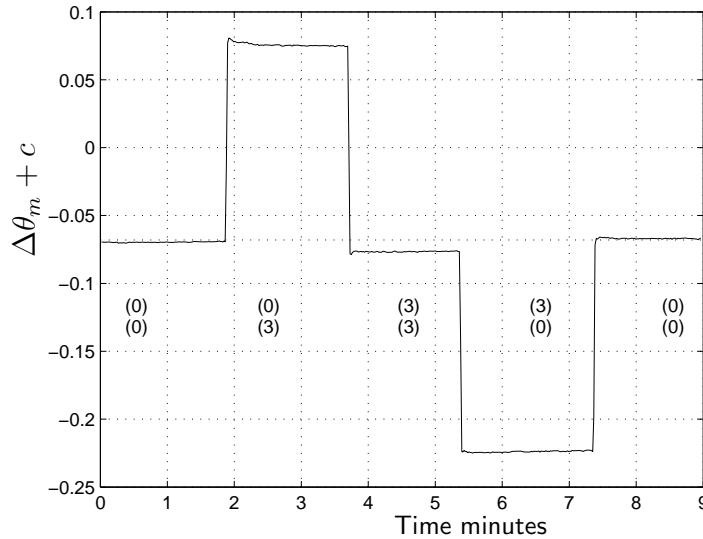


Figure 9.1: Angle of incidence difference for zero signal as distilled water and solution (3) were exchanged in the flow cells. An extra grid line is shown to emphasise the sensitivity to the common refractive index.

An initial measurement of the sensor response was made with the polariser transmission axis at 45° to p-polarised and is shown in figure 9.1. It was difficult to accurately determine when the angle of incidence difference, $\Delta\theta$, was zero. Throughout this chapter, therefore, the angle of incidence for zero signal, $\Delta\theta_m$, is given plus an unknown offset, c . The offset is determined by the position of the PSD, with $\Delta\theta_m + c = 0$ when the beam is centred on the PSD. Only distilled water and solution (3) were used for this measurement. For this measurement both of the flow cells were filled with water at the start of the measurement, as labelled $\begin{smallmatrix} (0) \\ (0) \end{smallmatrix}$ in the figure. Solution (3) was then injected into the bottom flow cell, the one covering the area of the SPR surface where the second reflection occurs, as labelled $\begin{smallmatrix} (0) \\ (3) \end{smallmatrix}$ in the figure. The top flow cell, the one covering the area of the SPR surface where the first reflection occurs, was then filled with solution (3) as labelled $\begin{smallmatrix} (3) \\ (3) \end{smallmatrix}$. The bottom flow cell was then filled with distilled water, $\begin{smallmatrix} (3) \\ (0) \end{smallmatrix}$, and then the top flow cell as well, $\begin{smallmatrix} (0) \\ (0) \end{smallmatrix}$. As shown in the figure, changes in the refractive index difference between the two surfaces are detected as changes in the angle of incidence for zero signal. The sensor response to a change in the common index can

also be seen in the figure as the difference in the angle of incidence for $\begin{pmatrix} 0 \\ 0 \end{pmatrix}$ and $\begin{pmatrix} 3 \\ 3 \end{pmatrix}$. The sensitivity of the instrument to changes in the refractive index difference is approximately 20 times larger than the sensitivity to changes in the common index. As described in chapter 7.3, sensitivity of the instrument to the common index can be caused by differences in the properties of the SPR surfaces where the two reflections occur and can be compensated for by adjusting the setting of the analyser or polariser. The solutions were exchanged between $\begin{pmatrix} 0 \\ 0 \end{pmatrix}$ and $\begin{pmatrix} 3 \\ 3 \end{pmatrix}$ as the polariser was adjusted and a setting of 45.9° from p-polarised was found to minimise the sensitivity to the common index.

9.2 Sensor response when compensated

With the polariser set to 45.9° , a series of experiments was made using the three salt solutions to characterise the sensor's response. For the first set of measurements, shown in figure 9.2, the flow cells were initially filled with water left over from previous measurements, as labelled $\begin{pmatrix} 0 \\ 0 \end{pmatrix}$. Water and the three solutions were then injected in order of increasing refractive index with each solution being added to the bottom flow cell first, then the top flow cell. At the end of the experiment the flow cells were filled in turn with water. A second set of measurements was made with the solutions now being added to the top flow cell first and then to the bottom flow cell. The second set of measurements are shown in figure 9.3.

As can be seen from the figures, the sensor output changes in response to refractive index differences and is almost independent of the common index. The spikes seen are caused by temperature differences as the solutions were added. The flow cell was stabilised at 19.5°C and the solutions were at the ambient temperature of 21°C .

The sensitivity of the sensor was calculated from the difference in the angle of incidence for zero signal between the mean for a half minute (19 to 19.5 minutes in the graphs) period with solution (3) in one flow cell and water in the other and the mean for a one minute period (23 to 24 minutes) with water in both flow cells. The change in angle of incidence was 0.145° for the first set of measurements and 0.149° for the second. From the difference

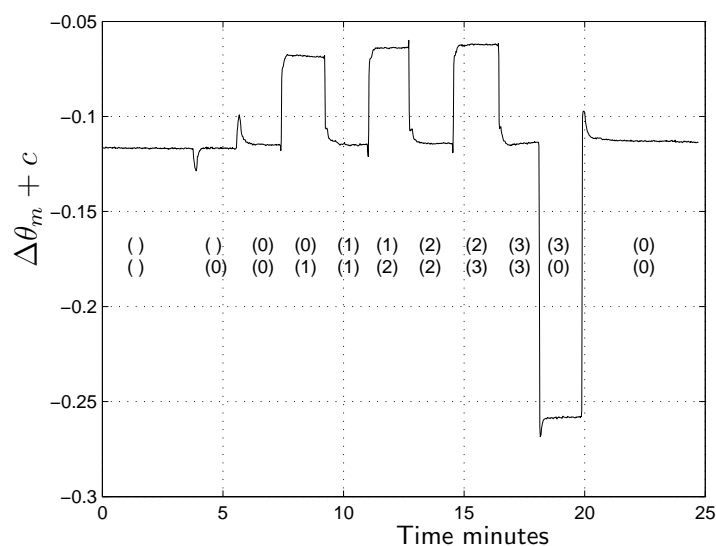


Figure 9.2: Angle of incidence difference for zero signal as distilled water and the three salt solutions were exchanged in the flow cells in order of increasing refractive index then water again and bottom flow cell first.

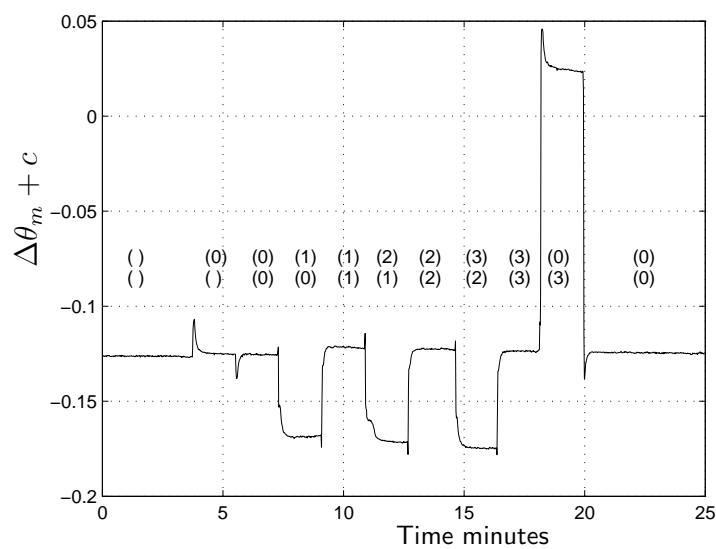


Figure 9.3: Angle of incidence difference for zero signal as distilled water and the three salt solutions were exchanged in the flow cells in order of increasing refractive index then water again and top flow cell first.

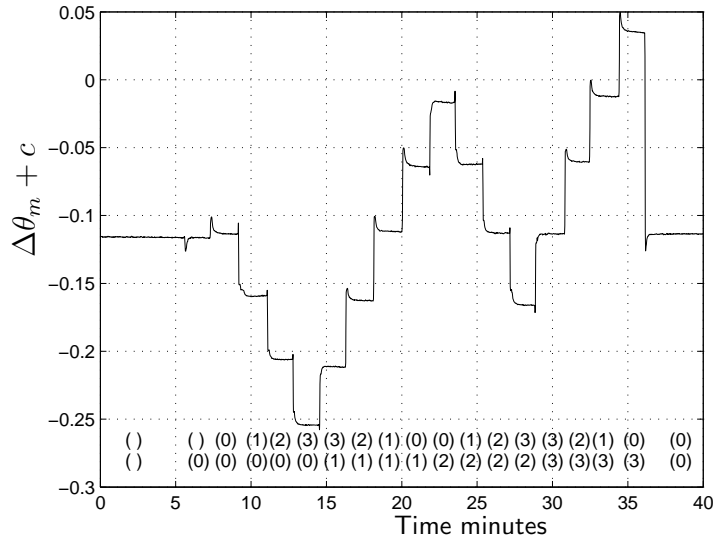


Figure 9.4: Angle of incidence difference for zero signal for all 16 combinations of the three salt solutions and distilled water.

between the refractive index of water and solution (3), 0.00133 RIU , this is a sensitivity, $d\Delta\theta_m/d\Delta n$, of 109 and $112 \text{ }^\circ\text{RIU}^{-1}$.

The noise was calculated as the standard deviation for a one minute period for each of the first three minutes of both sets of measurements. The mean noise was $1.86 \times 10^{-4} \text{ }^\circ$ for the first set of measurements and $2.05 \times 10^{-4} \text{ }^\circ$ for the second. From the calculated sensitivities, the noise in the refractive index difference was $1.7 \times 10^{-6} \text{ RIU}$ and $1.8 \times 10^{-6} \text{ RIU}$ respectively.

A measurement of the instrument's response to all 16 combinations of the three solutions and water was also made and is shown in figure 9.4. Again the angle of incidence difference for zero signal clearly depends on the refractive index difference of the solutions in the two flow cells.

A detailed view of the response of the instrument when both flow cells are filled with the same solution, for all three sets of measurements is shown in figure 9.5. The differences between $\Delta\theta_m$ for the different solutions are small and do not seem to be consistent. The one consistent result is that an increase in $\Delta\theta_m$ is observed when water is added to the top flow cell when it already contains water from the previous experiment. This may mean that

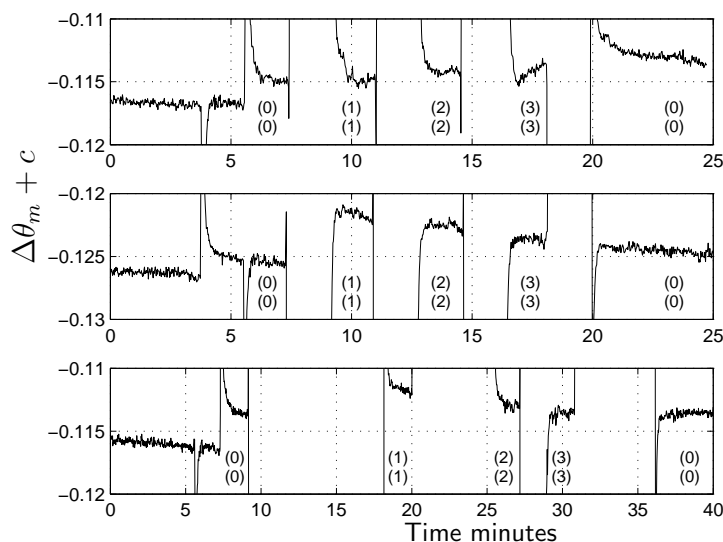


Figure 9.5: Angle of incidence difference for zero signal results for the three experiments above when both flow cells contain the same solution. The results are, from the top, those shown in figures 9.2, 9.3 and 9.4 respectively.

when a new solution was added it was not completely replacing the previous one or that there were drifts due to other effects e.g. bubbles in the flow cell. If the results for $\begin{smallmatrix} (0) \\ (0) \end{smallmatrix}$ and $\begin{smallmatrix} (3) \\ (3) \end{smallmatrix}$ are compared, the sensitivity to the common index is found to be at least one hundred times smaller than the sensitivity to the index difference. The second set of measurements shown (those from figure 9.3) are offset slightly from the others. These measurements were made two hours after the other measurements and the instrument has drifted slightly.

An analysis of the sensor response for the measurement of all 16 combinations of solutions that were presented in figure 9.4 was performed. For each of the 16 combinations of solutions, the mean $\Delta\theta_m + c$ value for the half minute before the next solution was added was calculated. The mean $\Delta\theta_m + c$ for both flow cells filled with water, $\begin{smallmatrix} (0) \\ (0) \end{smallmatrix}$, was then subtracted from the mean for each of the other combinations to find the change in the angle of index difference for zero signal. In figure 9.6 these results are plotted against the refractive index of the solution in the bottom flow cell ($n_2 = n_1 + \Delta n$) for each of the values of the refractive index of the solution in the top flow cell,

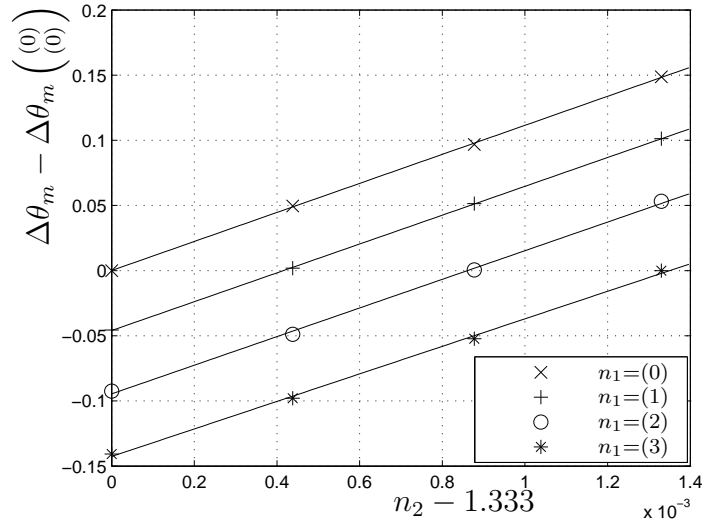


Figure 9.6: The change in the angle of incidence difference for zero signal vs the refractive index in the bottom flow cell (n_2) for different refractive indices in the top flow cell (n_1).

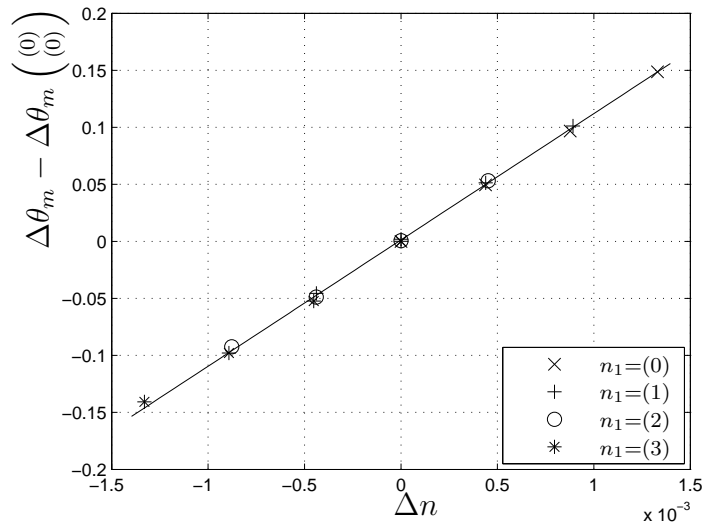


Figure 9.7: The change in the angle of incidence difference for zero signal vs the refractive index difference, $\Delta n = n_2 - n_1$. Results for different refractive indices in the top flow cell (n_1) are labelled to show the insensitivity to the common index.

n_1 . Each refractive index is shown as the difference between the refractive index of that solution and water. A linear fit to the data for each value of n_1 is used to calculate the sensitivity, shown in the table below.

Top flow cell	$n_1 - 1.33$	Sensitivity $d\Delta\theta_m/dn_2$
(0)	0	111.4 °RIU ⁻¹
(1)	0.00044	110.6 °RIU ⁻¹
(2)	0.00088	109.8 °RIU ⁻¹
(3)	0.00133	105.6 °RIU ⁻¹

Table 9.2: Sensitivity for different solutions in the top flow cell.

The sensitivities are very similar except for solution (3) in the top flow cell where the fitted sensitivity is significantly lower. It is noted that this lower sensitivity is dependent on one result, that for $\binom{3}{0}$ which gives the lowest $\Delta\theta_m$ observed. The change in $d\Delta\theta_m$ from $\binom{0}{0}$ to $\binom{3}{0}$ was smaller than that found for the measurements presented in figure 9.2. The larger value was 0.145° which gives better agreement with the other sensitivities. If this result is treated as an outlier and excluded from the fit the sensitivity changes to 109.9 °RIU⁻¹, similar to the others. This $\binom{3}{0}$ value is suspected to be an outlier as it disagrees with both the previous $\binom{3}{0}$ value (see figure 9.2) and the trend of the other results for this experiment. Inconsistent results have been observed when the solution was added to the flow cell too quickly or less than 5 ml of the salt solution was used. This result could also indicate that at $\binom{3}{0}$ the instrument has reached the edge of its linear range. It would be desirable to repeat these measurements to see if the $\binom{3}{0}$ result is consistent.

The refractive index difference between the solutions in the two flow cells ($\Delta n = n_2 - n_1$) can be calculated. The sensor response vs the refractive index difference is plotted for all 16 results in figure 9.7. A linear fit to all the results except for $\binom{3}{0}$ is shown to illustrate the sensitivity and linearity of the result. The gradient of the line, the sensitivity, is 110.8 °RIU⁻¹. From the figure it can be seen that the angle of index difference for zero signal, $\Delta\theta_m$, is linearly dependent on the refractive index difference, Δn , and almost independent of the common index, n_1 .

9.3 Results for a larger refractive index range

Measurements were also made with solutions covering a wider refractive index range. The salt concentration and the difference in the refractive index between the solution and water are shown in the table below.

Solution	NaCl % w/w	$n - 1.33$
(0)	0	0
(1)	1.00	0.00176
(5)	5.01	0.00876
(6)	6.03	0.0106

Table 9.3: The three higher index solutions used.

Note that solution (1) is not the same as for the previous measurements and that solutions (5) and (6) are numbered in proportion to their refractive indices. The polariser was again set to 45.9° .

Measurements were then made exchanging these solutions in the flow

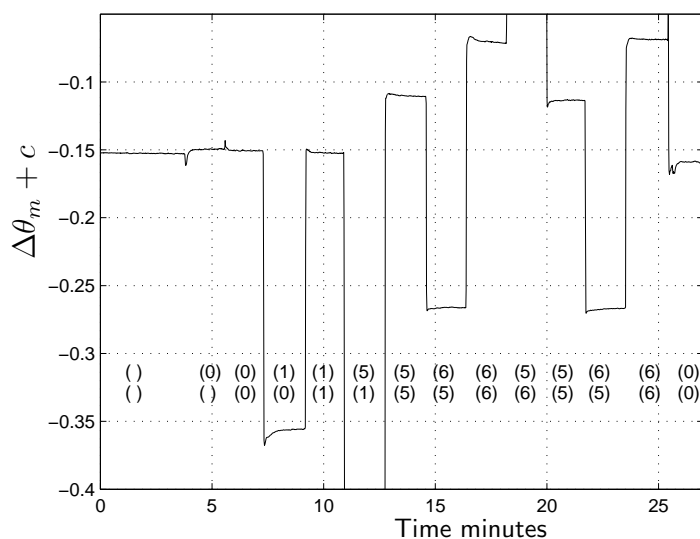


Figure 9.8: Angle of incidence difference for zero signal for water and the three high index solutions. Note again that solution (1) is not the same as for the earlier measurements.

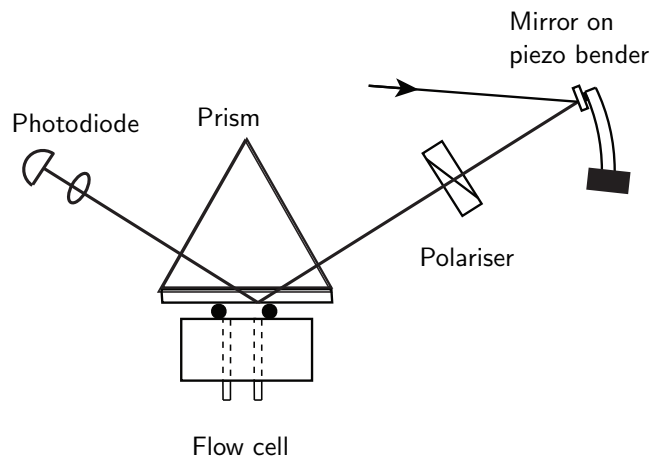


Figure 9.9: The effective configuration for the single channel measurements.

cells and are shown in figure 9.8. The graph is labelled with the contents of both the flow cells in the same way as for the previous measurements. The available $\Delta\theta$ scan range provided by the piezo bender actuator was much too small to cover the full range of $\Delta\theta_m$ for the range of refractive indices used. The scale of the graph was therefore set so that data where the actuator was at one of its limits are not shown. From the figure it can be seen that the sensor responds to the refractive index difference for the $\begin{smallmatrix} (1) \\ (0) \end{smallmatrix}$ and $\begin{smallmatrix} (6) \\ (5) \end{smallmatrix}$ results as expected, $\begin{smallmatrix} (5) \\ (6) \end{smallmatrix}$ is off-scale. The sensitivity of the instrument to changes in the common index clearly increases as the common refractive index increases. This is shown in the figure as the significant difference in $\Delta\theta_m$ between $\begin{smallmatrix} (0) \\ (0) \end{smallmatrix}$ and $\begin{smallmatrix} (5) \\ (5) \end{smallmatrix}$ or $\begin{smallmatrix} (6) \\ (6) \end{smallmatrix}$. The fact that the sensitivity to n_1 changes as the index increases is consistent with the theoretical modelling, for example figure 7.14.

9.4 Temperature changes

As well as the measurements of the response of the differential SPR instrument to refractive index changes presented above, the temperature sensitivity of the instrument was investigated. In figure 9.10, $\Delta\theta_m$ is shown with the temperature initially 20.7°C and then increased by 4.5°C. The setting of the temperature controller was changed 2 minutes into the experiment and the temperature takes several minutes to stabilise. Both of the flow cells were

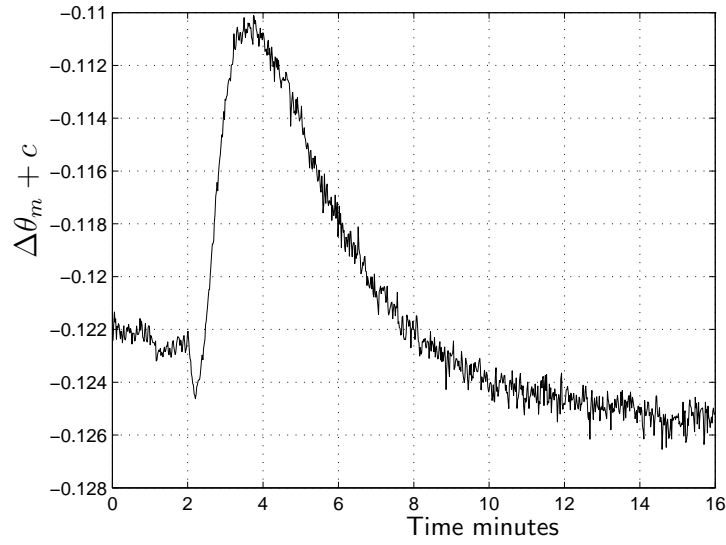


Figure 9.10: Angle of incidence difference for zero signal as the temperature is changed by 4.5°C starting at 2 minutes.

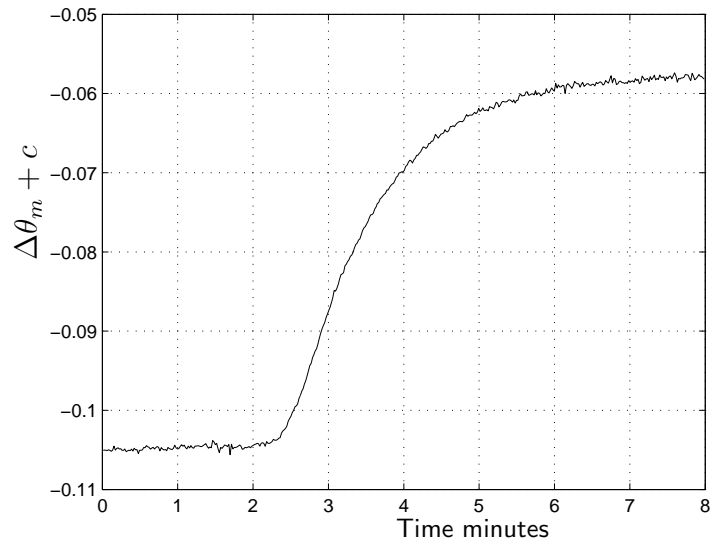


Figure 9.11: Angle of incidence difference for zero signal for the single channel configuration as the temperature is changed by -4°C starting at 2 minutes.

filled with water for all of this measurement.

For comparison, a single channel SPR measurement of a temperature change was made. The apparatus was converted to the single channel angle modulated SPR instrument equivalent to figure 9.9. To convert the apparatus, the analyser was removed and a polariser set to transmit p-polarised light was placed in the beam just before it is reflected at the second SPR surface. The light incident on the second SPR surface is now p-polarised regardless of the properties of the first SPR surface and the Fresnel rhomb. The angle of incidence at the second surface will still be modulated and so an AC signal in the intensity will be observed. This signal will be zero near the angle of incidence of the reflectance minimum of the SPR dip. Changes in the refractive index in the bottom flow cell, where the second SPR surface is, will change the angle of incidence at which the SPR dip occurs and can be detected from the change in the angle of incidence for zero signal. Changes in the refractive index in the top flow cell may change the transmission but will not change the angle of incidence for zero signal as the polarisation of the light incident at the surface in the bottom flow cell is now fixed at p-polarised. From a measurement of the response of the single channel instrument to exchanging water and the 1% salt solution in the bottom flow cell, the sensitivity was found to be $149\text{ }^{\circ}\text{RIU}^{-1}$. It is not clear why the sensitivity was significantly higher than for the differential instrument. The dependence of angle of incidence for zero signal on the temperature, for this single channel measurement is shown in figure 9.11. The temperature is initially 20.9°C and is then decreased by 4°C .

In figure 9.11 it can be seen that for the single channel configuration, the temperature change causes a significant change in the measured angle of incidence for zero signal. This is because the refractive indices of water and gold are temperature dependent. For the differential configuration however, as shown in figure 9.10, the measured angle of incidence changes by a much smaller amount during the temperature change, probably due to a difference in the rate of heating for the two flow cells. The angle of incidence $\Delta\theta_m$ then returns to very close to its original value after the temperature change is complete and the temperature of the flow cells is uniform again. This is because the reflection coefficients of the two SPR surfaces have a similar temperature dependence. The difference in temperature response of the

two configurations is much too large to be accounted for by the sensitivity difference between them.

9.5 Discussion and future work

The differential SPR instrument can effectively measure changes in the refractive index difference over the range $\Delta n = \pm 0.0013$ RIU. Insensitivity to the common index was achieved by adjusting the polariser as expected from the theoretical modelling of chapter 7.3. The noise in the refractive index difference is approximately 1.8×10^{-6} RIU. This is much larger than the shot noise limit found in the theoretical results. The noise is suspected to be due to fluctuations occurring at the SPR surfaces. Earlier versions of the experiment measuring the amplitude of the signal rather than the angle gave a similar noise in the refractive index so the PSD and feedback loop are not believed to be limiting the performance. The observed noise in the angle is also about twice the noise from the PSD measured in chapter 8.3. It is noted that the noise limit for the differential instrument is larger than that found for averaging large areas with the imaging instrument perhaps because there are now two reflections from SPR surfaces rather than one.

Future work

The measurements presented in this chapter may be viewed as a trial run for more detailed measurements to better characterise the sensors response. This is the most obvious work to do next. In particular a detailed calibration procedure measuring the sensitivity to the common index over a range of different indices and settings of the polariser.

The variation across the SPR surfaces could be characterised and this would enable a theoretical prediction of the sensitivity to the common index.

A number of improvements to the instrument were considered and could be implemented

- Some commercial SPR surfaces have been obtained and these could be investigated to see if they are more uniform.

- The noise in the refractive index as described above is about twice the limit due to the noise of the position sensitive detector. If significant accuracy improvements are to be obtained, more accuracy in monitoring the angle would be needed. The performance of the PSD used is limited by its resistive anode but a different PSD such as a split detector could be used.
- The limited range of the instrument, as shown in the results presented in figure 9.8, is due to the limited angle scan range of the piezo when driven by ± 30 V. Driving the piezo with a higher voltage or using a different piezo could allow a larger refractive index range to be investigated. The piezo used was selected for low cost and suitability for attaching strain gauges rather than range, and a piezo with at least five times greater range for ± 30 V has been ordered.

10 Conclusion

A polarisation imaging SPR instrument has been constructed. It was demonstrated that this instrument can detect refractive index changes over a 0.01 RIU range. For a 128×48 channel image the noise in the refractive index measurement was approximately 2×10^{-6} RIU, close to that expected from a theoretical analysis and the properties of the SPR surface and camera used. As expected from theoretical modelling, the noise showed little change as the setting of the polarisation analyser was altered in order to increase the sensitivity of the input polarisation for minimum transmission to refractive index changes. Significant variation in the sensitivity was observed and this is believed to be due to variations in the properties of the gold SPR surfaces. This instrument has a high accuracy compared to typical intensity imaging instruments [60] for a large number of channels with a simple optical system. The accuracy is much lower than the 2.6×10^{-8} RIU for 110 channels of the angle imaging instrument presented by VanWiggeren *et al.*[18]. Averaging groups of channels and using some channels as references did not produce significant accuracy improvements. The cause of this noise limit is not clear. A similar polarisation imaging technique has been demonstrated by Johnston *et al.* [66]. This instrument needs a custom CMOS chip as the sensor as compared to the standard CMOS camera used for my instrument. The noise performance of this sensor is not described.

A novel technique for differential SPR measurements was developed. Theoretical analysis of this technique suggested that it should allow the refractive index difference, between two areas of a SPR surface, to be measured with high accuracy and linearity. The effect on this instrument of differences between the properties of the two areas of the SPR surface was examined. As differences between the two areas of the SPR surface were found to make

the instrument sensitive to the common index, as well as the difference, a technique to compensate by rotating one of the polarisers was developed. An experimental implementation of the differential instrument was constructed. It was demonstrated that this instrument can detect refractive index difference changes over a ± 0.0013 RIU range, with a noise of approximately 2×10^{-6} RIU. When the input polariser was adjusted to compensate for the difference between the properties of the two areas of the SPR surface the sensitivity to the common index, over a 0.0013 RIU range, was almost eliminated. Existing dual channel instruments as described in chapter 2.3.2 measure the refractive index at two points on a SPR surface while this instrument makes a single measurement of the difference between the two areas. The original aim of this system was to achieve lower noise as noise common to both areas of the surface would be cancelled, however it appears from my imaging measurements that uncorrelated noise sources dominate. The noise obtained, 2×10^{-6} RIU is significantly higher than for the dual channel instrument of Hooper *et al.* [70] obtaining a noise of $\sim 1 \times 10^{-7}$.

Possible improvements and future work for the two SPR instruments demonstrated in this thesis have already been described in the two results chapters (see chapters 6 and 9). In particular, more work needs to be done to characterise the differential instrument. Both instruments had a noise limit of the order of 10^{-6} RIU. Attempts to reduce the noise below this level were unsuccessful. Before the two instruments presented in this thesis are improved it would be useful to examine this limit. A simple high accuracy single channel instrument could be constructed using either angle or polarisation modulation. Experiments could then be done to establish the noise due to the SPR surface rather than the instrument. More uniform gold surfaces could be used to see if this affects the noise.

A Scattering matrix method

The theoretical modelling of the instruments presented in this thesis require the reflection coefficients of SPR surfaces to be calculated. This was done using the Fresnel equations and the scattering matrix thin film modelling technique. As these methods are vital to the the theoretical results they are described below and the Matlab code implementation is given.

The Fresnel equations for the reflection and transmission amplitude coefficients of an interface between two materials for p and s polarised light are:

$$r_s = \frac{N_1 \cos \theta_1 - N_2 \cos \theta_2}{N_1 \cos \theta_1 + N_2 \cos \theta_2}, \quad (\text{A.1})$$

$$r_p = \frac{N_1 \cos \theta_2 - N_2 \cos \theta_1}{N_1 \cos \theta_2 + N_2 \cos \theta_1}, \quad (\text{A.2})$$

$$t_s = \frac{2N_1 \cos \theta_1}{N_1 \cos \theta_1 + N_2 \cos \theta_2}, \quad (\text{A.3})$$

$$t_p = \frac{2N_1 \cos \theta_1}{N_1 \cos \theta_2 + N_2 \cos \theta_1}, \quad (\text{A.4})$$

where N_1 and N_2 are the complex refractive indices of the material on the incidence (1) and transmission (2) sides of the interface and $\theta_{1,2}$ are the angles of incidence and transmission.

Consider a thin film system with an ambient and a substrate separated by m thin homogeneous films, as shown in figure A.1. The reflection and transmission of each interface are described by the Fresnel equations. The reflection and transmission properties of the whole system can be analysed with the scattering matrix method described by Azzam and Bashara [19].

Assume plane waves and let the electric field of the forward travelling $(+z)$ and backward travelling $(-z)$ waves be $E^+(z)$ and $E^-(z)$, respectively.

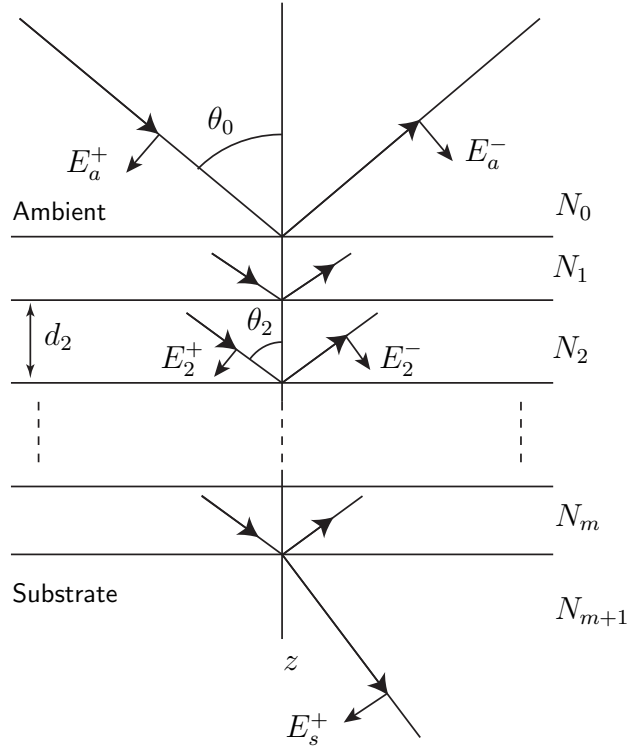


Figure A.1: A thin film system

The electric fields for two planes, parallel to the boundary of the substrate, at arbitrary positions z' and z'' can be related by a 2×2 transform matrix S .

$$\begin{bmatrix} E^+(z') \\ E^-(z') \end{bmatrix} = \begin{bmatrix} S_{11} & S_{12} \\ S_{21} & S_{22} \end{bmatrix} \begin{bmatrix} E^+(z'') \\ E^-(z'') \end{bmatrix}, \quad (\text{A.5})$$

$$E(z') = SE(z''). \quad (\text{A.6})$$

For two planes an infinitesimal distance δ above and below the interface between the j th and $j+1$ th materials, the interface matrix $I_{j(j-1)}$ is defined by

$$E(z_j - \delta) = I_{j(j-1)} E(z_j + \delta). \quad (\text{A.7})$$

If there are two planes, the first just past the $j-1$ to j interface and the second just before the j to $j+1$ interface, the propagation matrix L_j is

defined by

$$E(z_j + \delta) = L_j E(z_j + \delta). \quad (\text{A.8})$$

The relation between the fields in the ambient just before the first interface E_a and the field in the substrate just after the last interface E_s can be found in terms of the interface and propagation matrices by repeated use of equation A.6

$$E_a = S E_s, \quad (\text{A.9})$$

$$= I_{01} L_1 I_{12} \dots L_m I_{m(m+1)} E_s. \quad (\text{A.10})$$

where S is the scattering matrix for the thin film system. In full the relation between the fields is

$$\begin{bmatrix} E_a^+ \\ E_a^- \end{bmatrix} = \begin{bmatrix} S_{11} & S_{12} \\ S_{21} & S_{22} \end{bmatrix} \begin{bmatrix} E_s^+ \\ 0 \end{bmatrix}, \quad (\text{A.11})$$

where E_a^+ is the incident wave, the reflected (so backward travelling) wave is E_a^- , the transmitted wave is E_s^+ and there is no wave incident from the substrate side so $E_s^- = 0$. The reflection and transmission coefficients can then be found from the relations between the incident, reflected and transmitted waves

$$r = \frac{E_a^-}{E_a^+} = \frac{S_{21}}{S_{11}}, \quad (\text{A.12})$$

$$t = \frac{E_s^+}{E_a^+} = \frac{1}{S_{11}}. \quad (\text{A.13})$$

So if the scattering matrix can be found, the reflection and transmission coefficients of the thin film system can be calculated.

To find the interface matrices, consider the relation between the fields on either side of the interface of two materials a and b

$$\begin{bmatrix} E_a^+ \\ E_a^- \end{bmatrix} = \begin{bmatrix} I_{11} & I_{12} \\ I_{21} & I_{22} \end{bmatrix} \begin{bmatrix} E_b^+ \\ E_b^- \end{bmatrix}. \quad (\text{A.14})$$

If there is a plane wave incident from a to b on the interface, then the Fresnel reflection and transmission coefficients give the following relations between

the fields

$$E_b^+ = t_{ab}E_a^+, \quad (\text{A.15})$$

$$E_a^- = r_{ab}E_a^+, \quad (\text{A.16})$$

and $E_b^- = 0$ as there is no wave incident from that side. Using the relations from A.14

$$E_a^+ = I_{11}E_b^+, \quad (\text{A.17})$$

$$E_a^- = I_{21}E_b^+, \quad (\text{A.18})$$

the components of the first column of the interface matrix can be found in terms of the reflection and transmission coefficients

$$I_{11} = 1/t_{ab}, \quad (\text{A.19})$$

$$I_{21} = r_{ab}/t_{ab}. \quad (\text{A.20})$$

If there is now a plane wave incident from b to a

$$E_b^+ = r_{ba}E_b^-, \quad (\text{A.21})$$

$$E_a^- = t_{ba}E_b^-, \quad (\text{A.22})$$

with $E_a^+ = 0$ as no wave incident from that side. Applying A.14

$$0 = I_{11}E_b^+ I_{12}E_b^-, \quad (\text{A.23})$$

$$E_a^- = I_{21}E_b^+ I_{22}E_b^-. \quad (\text{A.24})$$

If the results for I_{11} and I_{21} in terms of the transmission and reflection coefficients found above are substituted into equations A.23 and A.24 then

$$E_b^+ = -I_{12}t_{ab}E_b^-, \quad (\text{A.25})$$

$$E_a^- = \left[\frac{r_{ab}r_{ba}}{t_{ab}} + I_{22} \right] E_b^-. \quad (\text{A.26})$$

The other two components of the interface matrix are then

$$I_{12} = -r_{ba}t_{ab}, \quad (\text{A.27})$$

$$I_{22} = (t_{ab}t_{ba} - r_{ab}r_{ba})/t_{ab}. \quad (\text{A.28})$$

Using the relation between the Fresnel coefficients for opposite sides of the same interface $r_{ba} = r_{ab}$ and $t_{ba} = (1 - r_{ab}^2)/t_{ab}$, the interface matrix is then

$$I_{ab} = \frac{1}{t_{ab}} \begin{bmatrix} 1 & r_{ab} \\ r_{ab} & 1 \end{bmatrix}. \quad (\text{A.29})$$

The reflection and transmission coefficients are different for p and s polarised light, so the interface and scattering matrices will also be different.

The reflection and transmission coefficients will depend on the angle of incidence in each material which can be found by applying Snell's law to each interface

$$N_0 \sin \theta_0 = N_1 \sin \theta_1 = \dots = N_m \sin \theta_m. \quad (\text{A.30})$$

In the case of total internal reflection, the angle of transmission will be complex.

To find the propagation matrix, consider the electric field E_0 and E_d at two planes a distance d apart in a single material. There is no interface and so no reflection, only a phase shift β given by

$$\beta = \frac{2\pi d N}{\lambda} \cos \theta. \quad (\text{A.31})$$

So the relation between the fields is

$$\begin{bmatrix} E_0^+ \\ E_0^- \end{bmatrix} = \begin{bmatrix} e^{i\beta} & 0 \\ 0 & e^{-i\beta} \end{bmatrix} \begin{bmatrix} E_d^+ \\ E_d^- \end{bmatrix} \quad (\text{A.32})$$

and so the layer matrix is,

$$L = \begin{bmatrix} e^{i\beta} & 0 \\ 0 & e^{-i\beta} \end{bmatrix}. \quad (\text{A.33})$$

The scattering matrix method was implemented in the Matlab code given below. This code takes vectors N and T which are the refractive index and thickness of the materials, the wavelength λ and angle of incidence (called θ_0 in the Matlab code). The function returns a vector $RCs = [r_p \ r_s \ t_p \ t_s]$.

```

function [RCs] = thinfilmsT(N,T,lambda,theta0)

% find the angle of incidence in the materials (Snell)
theta = asin(N(1).*sin(theta0)./N);

Ipa = zeros(2,2,length(N)-1); Isa = zeros(2,2,length(N)-1);

for c = 1:length(N)-1
    rpa = ( N(c+1).*cos(theta(c)) - N(c).*cos(theta(c+1)) ) ./
        ( N(c+1).*cos(theta(c)) + N(c).*cos(theta(c+1)) );
    rsa = ( N(c).*cos(theta(c)) - N(c+1).*cos(theta(c+1)) ) ./
        ( N(c).*cos(theta(c)) + N(c+1).*cos(theta(c+1)) );
    tpa = ( 2*N(c).*cos(theta(c)) ) ./ ( N(c+1).*cos(theta(c))
        + N(c).*cos(theta(c+1)) );
    tsa = ( 2*N(c).*cos(theta(c)) ) ./ ( N(c).*cos(theta(c))
        + N(c+1).*cos(theta(c+1)) );
    Ipa(:,:,c) = [1 rpa;rpa 1]./tpa; % Interface matrix for p
    Isa(:,:,c) = [1 rsa;rsa 1]./tsa; % Interface matrix for s
end

Sp = Ipa(:,:,1); Ss = Isa(:,:,1);

for c = 1:length(N)-2
    k = 2*pi./lambda.*(N(c+1).^2 - (N(1)*sin(theta0)).^2).^5 ;
    L = [exp(-i*k*T(c)) 0 ; 0 exp(i*k*T(c))]; % Layer matrix
    Sp = Sp*L*Ipa(:,:,c+1) ; % Scattering matrix for p
    Ss = Ss*L*Isa(:,:,c+1) ; % Scattering matrix for s
end

RCs = [0 0 0 0];
RCs(1) = Sp(2,1)/Sp(1,1); % rp
RCs(2) = Ss(2,1)/Ss(1,1); % rs
RCs(3) = 1/Sp(1,1); % tp
RCs(4) = 1/Ss(1,1); % ts

```

B Optical properties of materials

Gold

Data for the refractive index of gold was taken from the Handbook of Optical Constants of Solids [72]. The data was given as n and k with $N = n + ik$ and the data used is given in the table below.

λ nm	n	k
619.9	0.217	3.05
652.6	0.166	3.15
688.8	0.160	3.80
729.3	0.164	4.35
774.9	0.174	4.86

Table B.1: Optical constants of gold.

Using cubic spline interpolation, the refractive index of gold at $\lambda = 680$ nm is $N = 0.161 + 3.64i$ to 3 significant figures.

Chromium

Data for the refractive index of chromium is taken from Johnson and Christy [82]. The refractive index is given for the photon energy in eV so this was converted to wavelength using.

$$\lambda = \frac{hc}{E} \quad (\text{B.1})$$

where, $h = 6.626068 \times 10^{-34} \text{ m}^2\text{kg s}^{-1}$, Planck's constant, $c = 299792458 \text{ ms}^{-1}$ the speed of light and E the energy converted to joules using the charge on the electron $e = 1.602176 \times 10^{-19} \text{ C}$.

The data used are given in the table below.

$E \text{ eV}$	$\lambda \text{ nm}$	n	k
1.64	616.8	3.08	3.42
1.76	659.5	3.05	3.39
1.88	704.5	3.09	3.34
2.01	756.0	3.17	3.30

Table B.2: Optical constants of chromium.

Using cubic spline interpolation, the refractive index of chromium at $\lambda = 680 \text{ nm}$ is $N = 3.07 + 3.36i$ to 3 significant figures.

References

- [1] E. Kretschmann and H. Raether, “Radiative decay of non radiative surface plasmons excited by light (surface plasma waves excitation by light and decay into photons applied to non-radiative modes),” *Zeitschrift fuer Naturforschung*, vol. 23, pp. 2135–2136, 1968.
- [2] C. Nylander, B. Liedberg, and T. Lind, “Gas detection by means of surface plasmon resonance,” *Sensors and Actuators*, vol. 3, pp. 79–88, 1982.
- [3] J. Homola, S. S. Yee, and G. Gauglitz, “Surface plasmon resonance sensors: review,” *Sensors and Actuators B*, vol. 54, pp. 3–15, 1999.
- [4] J. Homola, “Present and future of surface plasmon resonance biosensors,” *Analytical and Bioanalytical Chemistry*, vol. 377, pp. 528–539, 2003.
- [5] G. Steiner, “Surface plasmon resonance imaging,” *Analytical and Bioanalytical Chemistry*, vol. 379, pp. 328–331, 2004.
- [6] A. A. Kruchinin and Y. G. Vlasov, “Surface plasmon resonance monitoring by means of polarization state measurement in reflected light as the basis of a dna-probe biosensor,” *Sensors and Actuators B*, vol. 30, pp. 77–80, 1996.
- [7] J. Homola, H. B. Lu, and S. S. Yee, “Dual-channel surface plasmon resonance sensor with spectral discrimination of sensing channels using dielectric overlayer,” *Electronics Letters*, vol. 35, no. 13, pp. 1105–1106, 1999.

- [8] D. J. Griffiths, *Introduction to Electrodynamics third edition*. Prentice-Hall, 1999.
- [9] S. A. Maier, *Plasmonics: Fundamentals and Applications*. Springer, 2007.
- [10] J. M. Pitarke, V. M. Silkin, E. V. Chulkov, and P. M. Echenique, “Theory of surface plasmons and surface-plasmon polaritons,” *Reports on Progress in Physics*, vol. 70, no. 1, pp. 1–87, 2007.
- [11] J. Homola, I. Koudela, and S. S. Yee, “Surface plasmon resonance sensors based on diffraction gratings and prism couplers: sensitivity comparison,” *Sensors and Actuators B*, vol. 54, pp. 16–24, 1999.
- [12] R. W. Wood, “On a remarkable case of uneven distribution of light in a diffraction grating spectrum,” *Philosophical Magazine*, 1902.
- [13] W. L. Barnes, A. Dereux, and T. W. Ebbesen, “Surface plasmon sub-wavelength optics,” *Nature*, vol. 424, pp. 824–830, 2003.
- [14] W. L. Barnes, W. A. Murray, J. Dintinger, E. Devaux, and T. Ebbesen, “Surface plasmon polaritons and their role in the enhanced transmission of light through periodic arrays of subwavelength holes in a metal film,” *Physical Review Letters*, vol. 92, no. 10, p. 107401, 2004.
- [15] T. Nikolajsen, K. Leosson, I. Salakhutdinov, and S. I. Bozhevolnyi, “Polymer-based surface-plasmon-polariton stripe waveguides at telecommunication wavelengths,” *Applied Physics Letters*, vol. 82, no. 5, pp. 668–670, 2003.
- [16] D. K. Gifford and D. G. Hall, “Emission through one of two metal electrodes of an organic light-emitting diode via surface-plasmon cross coupling,” *Applied Physics Letters*, vol. 81, no. 23, pp. 4315–4317, 2002.
- [17] A. Otto, “Excitation of nonradiative surface plasma waves in silver by the method of frustrated total reflection,” *Zeitschrift fur Physik*, vol. 216, pp. 398–410, 1968.
- [18] G. D. VanWiggeren, M. A. Bynum, J. P. Ertel, S. Jefferson, K. M. Robotti, E. P. Thrush, D. M. Baney, and K. P. Killeen, “A novel optical

- method providing for high-sensitivity and high-throughput biomolecular interaction analysis,” *Sensors and Actuators B*, vol. 127, pp. 341–349, 2007.
- [19] R. M. A. Azzam and N. M. Bashara, *Ellipsometry And Polarized Light*. North-Holland Publishing Company, 1977.
- [20] W. P. Chen and J. M. Chen, “Use of surface plasma waves for determination of the thickness and optical constants of thin metallic films,” *Journal of the Optical Society of America*, vol. 71, no. 2, pp. 189–191, 1981.
- [21] I. Pockrand, J. Swalen, J. Gordon-II, and M. Philpott, “Surface plasmon spectroscopy of organic monolayer assemblies,” *Surface Science*, vol. 74, pp. 237–244, 1977.
- [22] J. C. Quail and H. J. Simon, “Second-harmonic generation from silver and aluminum films in total internal reflection,” *Physical Review B*, vol. 31, no. 8, pp. 4900–4905, 1985.
- [23] T. Y. F. Tsang, “Surface-plasmon-enhanced third-harmonic generation in thin silver films,” *Optics Letters*, vol. 21, no. 4, pp. 245–247, 1996.
- [24] C. L. Baird and D. G. Myszka, “Current and emerging commercial optical biosensors,” *Journal of Molecular Recognition*, vol. 14, pp. 261–268, 2001.
- [25] J. Homola, “Surface plasmon resonance sensors for detection of chemical and biological species,” *Chemical Reviews*, no. 108, pp. 462–493, 2008.
- [26] A. Ibrahim, Z. Mohammad, and L. Akhlesh, “Surface plasmon resonance for biosensing: A mini-review,” *Electromagnetics*, vol. 28, no. 3, pp. 214–242, 2008.
- [27] V. Nanduri, A. K. Bhunia, S. I. Tu, G. C. Paoli, and J. D. Brewster, “Spr biosensor for the detection of l. monocytogenes using phage-displayed antibody,” *Biosensors and Bioelectronics*, vol. 23, pp. 248–252, 2007.
- [28] F. C. Dudak and I. H. Boyaci, “Development of an immunosensor based on surface plasmon resonance for enumeration of escherichia coli in water samples,” *Food Research International*, vol. 40, pp. 803–807, 2007.

- [29] N. Bassil, E. Maillart, M. Canva, Y. Levy, M.-C. Millot, S. Pissard, R. Narwa, and M. Goossens, "One hundred spots parallel monitoring of dna interactions by spr imaging of polymer-functionalized surfaces applied to the detection of cystic fibrosis mutations," *Sensors and Actuators B*, vol. 94, pp. 313–323, 2003.
- [30] J. Chung, S. Kim, R. Bernhardt, and J. Pyun, "Application of spr biosensor for medical diagnostics of human hepatitis b virus (hhbv)," *Sensors and Actuators B*, vol. 111–112, pp. 416–422, 2005.
- [31] E. S. Forzani, K. Foley, P. Westerhoff, and N. Tao, "Detection of arsenic in groundwater using a surface plasmon resonance sensor," *Sensors and Actuators B*, vol. 123, pp. 82–88, 2007.
- [32] Rajan, S. Chand, and B. Gupta, "Surface plasmon resonance based fiber-optic sensor for the detection of pesticide," *Sensors and Actuators B*, vol. 123, pp. 661–666, 2007.
- [33] D. R. Shankaran, K. Matsumoto, K. Toko, and N. Miura, "Development and comparison of two immunoassays for the detection of 2,4,6-trinitrotoluene (tnt) based on surface plasmon resonance," *Sensors and Actuators B*, vol. 114, pp. 71–79, 2006.
- [34] B. H. Ong, X. Yuan, S. C. Tjin, J. Zhang, and H. M. Ng, "Optimised film thickness for maximum evanescent field enhancement of a bimetallic film surface plasmon resonance biosensor," *Sensors and Actuators B*, vol. 114, pp. 1028–1034, 2006.
- [35] B. Liedberg, C. Nylander, and I. Lundström, "Surface plasmon resonance for gas detection and biosensing," *Sensors and Actuators*, vol. 4, p. 299, 1983.
- [36] K. Matsubara, S. Kawata, and S. Minami, "Optical chemical sensor based on surface plasmon measurement," *Applied Optics*, vol. 27, no. 6, pp. 1160–1163.
- [37] K. Johansen, R. Stalberg, I. Lundström, and B. Liedberg, "Surface plasmon resonance: instrumental resolution using photo diode arrays," *Measurement Science and Technology*, vol. 11, pp. 1630–1638, 2000.

- [38] T. Chinowsky, J. Quinn, D. Bartholomew, R. Kaiser, and J. Elkind, "Performance of the spreeta 2000 integrated surface 4 plasmon resonance affinity sensor," *Sensors and Actuators B*, vol. 91, no. 1–3, pp. 266–274, 2003.
- [39] C. Chou, H. T. Wu, Y. C. Huang, and Y. L. Chen, "Characteristics of a paired surface plasma waves biosensor," *Optics Express*, vol. 14, no. 10, pp. 4307–4315, 2006.
- [40] L. M. Zhang and D. Uttamchandani, "Optical chemical sensing employing surface plasmon resonance," *Electronics Letters*, vol. 24, no. 23, pp. 1469–1470, 1988.
- [41] F. Caruso, M. J. Jory, G. W. Bradberry, J. R. Sambles, and D. N. Furlong, "Acousto-optic surface-plasmon resonance measurements of thin films on gold," *Journal of Applied Physics*, vol. 83, no. 2, pp. 1023–1028, 1998.
- [42] S. Nelson, K. Johnston, and S. Yee, "High sensitivity surface plasmon resonance sensor based on phase detection," *Sensors and Actuators B*, vol. 35–36, pp. 187–191.
- [43] H. P. Chiang, J. L. Lin, and Z. W. Chen, "High sensitivity surface plasmon resonance sensor based on phase interrogation at optimal incident wavelengths," *Applied Physics Letters*, vol. 88, no. 141105, 2006.
- [44] B. Ran and S. G. Lipson, "Comparison between sensitivities of phase and intensity detection in surface plasmon resonance," *Optics Express*, vol. 14, no. 12, pp. 5641–5650, 2006.
- [45] X. Yina and L. Hesselink, "Goos-hänchen shift surface plasmon resonance sensor," *Applied Physics Letters*, vol. 89, p. 261108, 2006.
- [46] H. M. Cho, W. Chegala, Y. J. Choa, Y. Kimb, and H. Kim, "Enhancement of biomolecular detection sensitivity by surface plasmon resonance ellipsometry," *Proceedings of SPIE*, vol. 6008, no. 1F, 2005.
- [47] H. Arwin, M. Poksinski, and K. Johansen, "Total internal reflection ellipsometry: principles and applications," *Applied Optics*, vol. 43, no. 15, pp. 3028–3036, 2004.

- [48] J. Homola and S. S. Yee, “Novel polarization control scheme for spectral surface plasmon resonance sensors,” *Sensors and Actuators B*, vol. 51, pp. 331–339, 1998.
- [49] Z. Sun, Y. He, and J. Guo, “Surface plasmon resonance sensor based on polarization interferometry and angle modulation,” *Applied Optics*, vol. 45, no. 13, pp. 3071–3076, 2006.
- [50] I. R. Hooper and J. R. Sambles, “Sensing using differential surface plasmon ellipsometry,” *Journal of Applied Physics*, vol. 96, no. 5, pp. 3004–3011, 2004.
- [51] C. E. Stewart, I. R. Hooper, and J. R. Sambles, “Surface plasmon differential ellipsometry of aqueous solutions for bio-chemical sensing,” *Journal of Physics D: Applied Physics*, vol. 41, p. 105408, 2008.
- [52] R. Slavík, J. Homola, and J. Čtyroký, “Single-mode optical fiber surface plasmon resonance sensor,” *Sensors and Actuators B*, vol. 54, pp. 74–79, 1999.
- [53] H. Y. Lin, Y. C. Tsao, W. H. Tsai, Y. W. Yang, T. R. Yan, and B. C. Sheu, “Development and application of side-polished fiber immunosensor based on surface plasmon resonance for the detection of legionella pneumophila with halogens light and 850 nm-led,” *Sensors and Actuators A*, vol. 138, pp. 299–305, 2007.
- [54] J. Čtyroký, J. Homola, E. Brynda, M. Skalsky, P. Nekvindová, J. Špírková, J. Škvor, and J. Šchröfel, “Surface plasmon resonance biosensor based on integrated optical waveguide,” *Sensors and Actuators B*, vol. 76, pp. 8–12, 2001.
- [55] P. Tobiška, O. Hugon, A. Trouillet, and H. Gagnaire, “An integrated optic hydrogen sensor based on spr on palladium,” *Sensors and Actuators B*, vol. 74, pp. 168–172, 2001.
- [56] J. Dostálek and J. Homola, “Surface plasmon resonance sensor based on an array of diffraction gratings for highly parallelized observation of biomolecular interactions,” *Sensors and Actuators B*, vol. 129, pp. 303–310, 2008.

- [57] O. Telezhnikova and J. Homola, "New approach to spectroscopy of surface plasmons," *Optics Letters*, vol. 31, no. 22, pp. 3339–3341, 2006.
- [58] G. J. Wegner, A. W. Wark, H. J. Lee, E. Codner, T. Saeki, S. Fang, and R. M. Corn, "Real-time surface plasmon resonance imaging measurements for the multiplexed determination of protein adsorption/desorption kinetics and surface enzymatic reactions on peptide microarrays," *Analytical Chemistry*, vol. 76, pp. 5677–5684, 2004.
- [59] C. T. Campbell and G. Kim, "Spr microscopy and its applications to high-throughput analyses of biomolecular binding events and their kinetics," *Biomaterials*, vol. 28, pp. 2380–2392, 2007.
- [60] J. S. Shumaker-Parry and C. T. Campbell, "Quantitative methods for spatially resolved adsorption/desorption measurements in real time by surface plasmon resonance microscopy," *Analytical Chemistry*, vol. 76, pp. 907–917, 2004.
- [61] M. Piliarik, H. Vaisocherová, and J. Homola, "A new surface plasmon resonance sensor for high-throughput screening applications," *Biosensors and Bioelectronics*, vol. 20, pp. 2104–2110, 2005.
- [62] M. Piliarik, H. Vaisocherová, and J. Homola, "Towards parallelized surface plasmon resonance sensor platform for sensitive detection of oligonucleotides," *Sensors and Actuators B*, vol. 121, pp. 187–193, 2007.
- [63] A. G. Notcovich, V. Zhuk, and S. G. Lipson, "Surface plasmon resonance phase imaging," *Applied Physics Letters*, vol. 76, pp. 1665–1667, March 2000.
- [64] S. J. Chen, Y.-D. Su, F. M. Hsiu, C. Y. Tsou, and Y. K. Chen, "Surface plasmon resonance phase-shift interferometry: Real-time dna microarray hybridization analysis," *Journal of Biomedical Optics*, vol. 10, no. 3, p. 034005, 2005.
- [65] A. M. C. Lokate, J. B. Beusink, G. J. M. P. Geert A. J. Besselink, and R. B. M. Schasfoort, "Biomolecular interaction monitoring of autoantibodies by scanning surface plasmon resonance microarray imaging," *Journal of the American Chemical Society*, vol. 129, pp. 14013–14018, 2007.

- [66] N. Johnston, C. Stewart, R. Light, B. Hayes-Gill, M. Somekh, S. Morgan, J. Sambles, and M. Pitter, "Quad-phase synchronous light detection with 64 x 64 cmos modulated light camera," *Electronics Letters*, vol. 45, no. 21, pp. 1090–1091, 2009.
- [67] L. A. Lyon, W. D. Holliway, and M. J. Natan, "An improved surface plasmon resonance imaging apparatus," *Review of Scientific Instruments*, vol. 70, no. 4, pp. 2076–2081, 1999.
- [68] E. Fu, S. Ramsey, R. Thariani, and P. Yager, "One-dimensional surface plasmon resonance imaging system using wavelength interrogation," *Review of Scientific Instruments*, vol. 77, no. 076106, pp. 1–3, 2006.
- [69] I. Stemmler, A. Brecht, and G. Gauglitz, "Compact surface plasmon resonance-transducers with spectral readout for biosensing applications," *Sensors and Actuators B*, vol. 54, pp. 98–105, 1999.
- [70] I. Hooper, M. Rooth, and J. Sambles, "Dual-channel differential surface plasmon ellipsometry for bio-chemical sensing," *Biosensors and Bioelectronics*, vol. 25, pp. 411–417, 2009.
- [71] J. Dostálek, H. Vaisocherová, and J. Homola, "Multichannel surface plasmon resonance biosensor with wavelength division multiplexing," *Sensors and Actuators B*, vol. 108, pp. 758–764, 2005.
- [72] E. D. Palik, *Handbook of Optical Constants of Solids*. Academic Press, San Diego, 1998.
- [73] P. S. Kenrick, "Grain boundary diffusion effects of films of gold on chromium," *Nature*, vol. 217, pp. 1248–1251, 1968.
- [74] N. P. Barnes and L. B. Petway, "Variation of the verdet constant with temperature of terbium gallium garnet," *Journal of the Optical Society of America B*, vol. 9, no. 10, pp. 1912–1915, 1992.
- [75] P. Horowitz and W. Hill, *The Art of Electronics*. Cambridge University Press, 1989.
- [76] J. A. Davis and R. M. Bunch, "Temperature dependence of the faraday rotation of hoya fr-5 glass," *Applied Optics*, vol. 23, no. 4, pp. 633–636, 1984.

-
- [77] R. B. Northrop, *Introduction to instrumentation and measurements*, p. 413. CRC Press, 1997.
- [78] D. E. Aspnes, E. Kinsbron, and D. D. Bacon, “Optical properties of Au: Sample effects,” *Physical review B*, vol. 21, no. 8, pp. 3290–3299, 1980.
- [79] D. R. Lide, *CRC Handbook of Chemistry and Physics*, page 8-71. CRC Press/Taylor and Francis, 88th ed., 2008.
- [80] L. Holland, *Vacuum Deposition of Thin Films*, p. 143. Chapman and Hall, 4th ed., 1961.
- [81] P. C. D. Hobbs, *Building Electro-Optical Systems: Making It All Work*. Wiley, 2000.
- [82] P. B. Johnson and R. W. Christy, “Optical constants of transition metals: Ti, V, Cr, Mn, Fe, Co, Ni, and Pd,” *Physical Review B*, vol. 9, no. 12, pp. 5056–5070, 1974.